To the Graduate Council:

I am submitting herewith a thesis written by Daniel A. Bales entitled, "A Study of Decarburization in SAE 1042 Steel: Its Effect on Fatigue Life, Tensile Properties, and Fatigue Fractography." I recommend that it be accepted in partial fulfillment of the requirements for the degree of Master of Science, with a major in Metallurgical Engineering.

W. T. Becker

W. T. Becker, Major Professor

We have read this thesis
and recommend its acceptance:

Ben T. Oliver

A Mathews

Accepted for the Council:

L Evans Roth

Vice Chancellor
Graduate Studies and Research

A STUDY OF DECARBURIZATION IN SAE 1042 STEEL: ITS EFFECT ON FATIGUE LIFE, TENSILE PROPERTIES, AND FATIGUE FRACTOGRAPHY

A Thesis

Presented for the

Master of Science

Degree

The University of Tennessee, Knoxville

Daniel A. Bales

August 1977

ABSTRACT

The R. R. Moore rotating-beam fatigue test was used to determine the effects of increased surface decarburization on the fatigue life of SAE 1042 steel. This test was conducted on three series of test specimens: (1) specimens having no surface decarburization (series D-1), (2) specimens having a 0.038 inch (0.97 mm) decarburized surface layer (series D-8), and (3) specimens having a 0.080 inch (2.03 mm) decarburized surface layer (series D-24). In addition to the fatigue tests, the change in various tensile properties resulting from surface decarburization was investigated for each of the three test series utilizing the standard ASTM tensile test.

Careful study of the fractured fatigue specimens by scanning electron microscopy (SEM) revealed important information as to the nature and morphology of fatigue striations present in medium carbon steels, and established the "quasi-striation" pattern as the primary microscopic identity present in normalized SAE 1042 steel.

Results of the fatigue tests indicated that the initial decarburization depth had the greatest effect on the fraction of life degradation, while the tensile properties tests proved that the tensile properties, ultimate tensile strength (UTS) and yield strength (YS), originally reduced by surface decarburization, could be restored with proper machining practices.

In essence the study showed:

1. A decarburized surface layer severely reduces fatigue life.
2. Fatigue life decreases with an increase in the decarburization depth.
3. Removal of the decarburized surface layer completely restores the initial tensile properties.
4. Macroscopic fracture surface appearance is not affected by the presence of decarburization.
5. Three distinct fracture surface appearances exist in the applied stress range of a fatigue curve: (1) a "jagged" fracture surface at high stresses (above the YS), (2) a "ratcheted" fracture surface at medium stresses (approximately 1/2 of the UTS), and (3) a "smooth" fracture surface at low stresses (approximately 1/2 of the YS).
6. Striations are invariably more prone to form in primary ferrite.
7. Striation density is enhanced by (1) a reduction in the applied stress, and (2) an increase in the depth of surface decarburization.
8. No direct correlation between applied stress and striation spacing can be determined for materials which exhibit primarily "quasi-striation" fatigue patterns.

Particular emphasis was given the implementation of computerized statistical data analysis. The unique combination of the statistical analysis system (SAS) and curve fitting programs, specifically developed for this study is discussed.

TABLE OF CONTENTS

LIST OF TABLES

LIST OF FIGURES

FIGURE | PAGE

FIGURE PAGE

FIGURE PAGE

FIGURE PAGE

FIGURE PAGE

NOMENCLATURE

AA	=	Arithmetical Average
A_3	=	austenite-ferrite allotropic transformation
A.R.	=	as received condition
ASM	=	American Society for Metals
ASTM	=	American Society for Testing and Materials
^oC	=	degrees Centigrade
C.F.	=	cold finished
CLA	=	center line average
cpm	=	cycles per minute
Decarb	=	decarburization
D-1	=	decarburized at 1550^{o}F (843^{o}C) for one hour
D-8	=	decarburized at 1550^{o}F (843^{o}C) for eight hours
D-24	=	decarburized at 1550^{o}F (843^{o}C) for 24 hours
DPH	=	diamond pyramid hardness
ϵ	=	strain (in/in)
^oF	=	degrees Fahrenheit
Fe_3C	=	iron carbide
FeO	=	iron oxide
K	=	stress intensity factor
M	=	mega (10^6)
MN/m^2	=	Mega-Newton per square meter

μ	=	micron (10^{-6} meters) (3.94×10^{-5} inches)
μ-in	=	micro-inches (10^{-6} inches)
mm	=	millimeter
N_f	=	number of cycles to failure
psi	=	pounds per square inch
R_B	=	Rockwell Hardness Number, B-scale
RMS	=	root mean square
rpm	=	revolutions per minute
Sa	=	stress amplitude
Se	=	endurance limit stress
Sm	=	mean stress
Sr	=	stress range
SAE	=	Society of Automotive Engineers
SAS	=	Statistical Analysis System
SEM	=	scanning electron microscopy
S-N	=	stress verses number of cycles to failure
UTS	=	ultimate tensile strength
YP	=	yield point
YS	=	yield strength

CHAPTER 1

INTRODUCTION AND HISTORICAL REVIEW

The effect of decarburization on fatigue life was once a very controversial topic. Following a surge of activity in the 1930's with a general consensus that decarburization was detrimental to fatigue life (14, 32, 33), a renewed interest during the 1940's and 1950's concluded that in some cases decarburization caused little if any decrease in fatigue strength (28, 44, 61). The dispute over the degree of damage caused by decarburization remained, although to a lesser extent, a topic of discussion into the early 1960's (67). While most recent literature now states emphatically that decarburization is detrimental to fatigue life, there exists little quantitative data supporting these statements (5, 42, 64, 68).

As one might expect, the decrease in fatigue life was and remains a primary concern of the automotive industry. What is surprising is the lack of suitable standards by which to control the acceptability of decarburized automotive parts. While ASM, ASTM, and SAE state that decarburization is detrimental to fatigue strength, neither ASM, ASTM, nor SAE have published, in open literature, any statements regarding the acceptability of decarburized automotive parts.

Factors Affecting Fatigue Life

Several factors commonly affect the fatigue behavior of a part. A discussion of the variables affecting the fatigue failure is complex, due to the large number of macroscopic and microscopic parameters.

Macroscopic parameters. Macroscopic parameters include (1) state of stress, (2) surface condition, and (3) residual stress.

Failures are generally caused by repeated loadings below the yield strength (YS). The endurance stress (Se), which is generally defined as the maximum value for which a plain specimen can sustain 10^7 cycles without failure (31, 49, 68), is greatly influenced by the state of stress (uniaxial verses multiaxial), as well as the stress range (Sr) and the stress amplitude (Sa). The rate of loading is also a variable (24, 53). Collection of uniaxial stress data is commonly associated with completely reversed bending, as in a R. R. Moore rotating-beam fatigue test in which the test specimen experiences pure bending. The bending stress in a rotating-beam test alternates continuously between a maximum tension and a maximum compression (both values equal in magnitude to the applied stress); the mean stress (Sm) remains zero at all times. However, for unidirectional bending (plane bending), the mean stress is, generally, greater than zero; and the test specimen experiences a bending stress as well as a shear stress. The endurance limits obtained with unidirectional bending may differ considerably from the endurance limits (using the same material) obtained with rotating-beam tests (27, 31).

Surface roughness can greatly affect the fatigue life of any part. For ground and polished ferrous parts, the endurance stress (Se) may be taken as approximately 50% of the ultimate tensile strength (UTS), while the Se of as-forged parts is approximately 10% of the UTS. Se values for machined finishes such as turning, milling, shaping, and polishing with emery paper range from 25% to 40% of the UTS (34, 49, 68). Horger (41) reported that the endurance limit of "soft steels" does not vary appreciably over a range of "fine to rough" turned surface finishes, but specimens of the same material with a polished surface finish had an increase in endurance limit of 10%; however, he found no variation in the endurance limit of ground, polished, and super-finished "soft steels." Fluck (26) reported that polishing of lathe-turned specimens increased the endurance limit as much as 400% in annealed SAE 1035 steel.

Mechanical and thermal processing of ferrous alloy parts commonly involves a surface treatment to obtain an increased fatigue life or improved wear resistance and frequently requires an additional machining operation for dimensional tolerances and surface finish. Typical examples are leaf springs, automotive axles, and aircraft landing gears. Surface treating operations include cold working, altering the microstructure as in induction hardening, and changing the chemical composition as in carburizing, cyaniding, or nitriding. In all surface treatments and machining operations, residual stresses, those stresses which would exist in an elastic body if all loads were removed, may be generated (3).

Cold working a material as in cold rolling or shot peening involves straining the material beyond the yield point (YP), causing the material to flow plastically. This process increases the material's resistance to further plastic deformation by increasing the yield strength (YS) of the outer surface, but more importantly produces a beneficial residual stress pattern (31, 49). One of the more common surface treatments involving an alteration of the microstructure is induction hardening. Residual stresses in this type of treatment are induced by a phase change resulting from the quenching of a hardenable steel. The volume change associated with the formation of martensite in the surface of the steel gives rise to compressive stresses at the surface and tensile stresses at the interior (3, 6, 27, 49). It is a well-established fact that compressive residual stresses are considered beneficial to fatigue life in bending. While the influence of continued cyclic loading may somewhat reduce these stresses, the addition of a compressive residual stress and an applied tensile stress results in a reduced working stress at the surface, where stresses are usually a maximum (3, 40, 41, 43, 49, 58, 68).

Certain machining processes (grinding in particular) may produce tensile residual stresses in the outer surface. Richards (60) found that while turning, recessing, and polishing with emery paper produced compressive residual stresses, grinding produced high tensile stresses in the surface which extended from 0.002 inches (0.05 mm) to 0.024 inches (0.61 mm) below the surface due to the thermal action of the heat generated. Horger (43) reported that the grinding process produced a deterioration of the mechanical properties in the surface material. Others (2, 39, 68) have reported that grinding produces tensile residual stresses, some so great that micro-cracking of the surface was observed (3, 31). Hendriksen (36), one of the first investigators to estimate the magnitude of residual stresses produced by various machining operations, pointed out that residual stresses increase as the carbon content decreases. In tests conducted on SAE 1020 steel, using a single point tool with a lengthwise planing process, he found that residual stresses almost as great as the UTS (approximately 1.0×10^5 psi) existed in areas of high stress concentration. Lipson, Noll, and Clock (49) suggested that residual stresses less than 2.5×10^4 psi should be neglected, but Spotts (68) postulated that the combination of an applied high tensile stress and a high residual stress resulting from a machining operation such as grinding would give premature failure.

Microscopic parameters. Microscopic parameters which exist are (1) core microstructure, (2) surface microstructure, (3) surface carbides, (4) intergranular oxidation, (5) surface oxidation, and (6) internal oxidation.

Properties of the core material often differ from those exhibited by the surface material. An example is the induction hardening process which was explained earlier. The microstructure, whether of the core or of the surface, may contain ferrite, pearlite, martensite, tempered martensite, or some combination of these. In situations where contrasting core and surface microstructures exist, the presence of high tensile residual stresses at the core/case juncture may lead to premature failure (39, 44).

Surface carbides, intergranular oxidation, surface oxidation, and internal oxidation all may cause adverse service conditions. Grover (31) has stated that one of the most important factors governing the strength of heat treatable steels is the size, shape, and distribution of carbides (Fe_3C). Brittle particles such as carbides in the surface act as sites of stress concentration, causing early crack initiation. Intergranular oxidation, sometimes called grain boundary oxidation, occurs about 1740°F (950°C) when the oxidizing action of the atmosphere develops oxide (FeO) particles along the original austenite grain boundaries (42). Surface oxidation (scale) occurs readily in most oxidizing atmospheres above 900°F (482°C). Both intergranular and surface oxidation provide sites of high stress concentration which eventually lead to premature failure. Internal oxidation results in the formation of voids and oxide particles (inclusions) which can lower the fatigue strength markedly due to the increased crack propagation rates (16, 55, 59, 63, 65).

Prior Work Involving Decarburization

During the 1920's and throughout the 1930's considerable information was published which argued that decarburization was detrimental to fatigue life (4, 14, 28, 29, 32, 33). The data of this time consisted primarily of completely reversed bending tests and the conclusions were based solely on completely reversed bending data and the endurance limit. Statements referring to this work are commonly seen in texts through the 1950's (17, 20, 31, 41, 61). Possibly due to the war effort during the early 1940's, a renewed interest developed in fatigue failure analysis. These data were mainly collected for high carbon steels, but did include non-reversed bending data. These steels were much higher in ultimate tensile strength (UTS) than materials previously tested, and the result was a conflict in the conclusions concerning the effect of surface decarburization; the latter data indicated that decarburization had little, if any, effect on fatigue life degradation, while the earlier data stated that decarburization was detrimental to fatigue life. Implications of the non-reversed bending tests and the higher strength steels remain to be adequately discussed in published literature (17, 31, 35, 44, 61). A categorization of the major researchers, the type of study conducted, and their findings are presented in Table 1.

Hankins and Becker (32, 33) did extensive testing on springs, controlling both the surface finish and the decarburization. They concluded that both the surface finish and the decarburization caused

TABLE 1

FINDINGS OF DECARBURIZATION RELATED FATIGUE TESTS

Reference	Method of Testing	Weight Percent Carbon	Surface Condition	Conclusions
1	A	0.40	1	D
25	A	0.94-1.05	1	NC
28	A	0.36-0.79	2	I & D
32	A & B	0.54-0.55	2	D
33	A & B	0.32-0.60	2	D
44	A	0.40	2	N & D
61	B	0.60	2	I & D
67	A	0.61	1	D

A = Rotating-Beam; Mean Stress Equal to Zero.
B = Unidirectional Bending; Mean Stress Greater than Zero.

1 = Decarburized.
2 = Decarburized and Non-Decarburized.

I = Decarburization Increases Fatigue Life.
N = No Appreciable Change in Decarburized and Non-Decarburized Test Results.
D = Decrease in Fatigue Life Due to Decarburization.
NC = Non-Conclusive.

a decrease in fatigue life; however, decarburization was found to be the more detrimental of the two. Failure was explained by the early formation of a crack in the softer decarburized layer which resulted in a stress concentration at the crack tip. With the aid of stress concentration the crack then propagated into the two-phase material, eventually causing failure.

Burns (18) reported that a high-silicon, low-manganese spring steel is less liable to premature failure than one containing high manganese, due to the mechanical defects on the surface. He found that a high silicon content reduces the tendency to scaling during heat treatment, but at the same time promotes deep surface decarburization, while manganese has the opposite effect with regards to both scaling and decarburization. Andrew and Richardson (4) reported that surface decarburization is dependent on the furnace temperature, the gaseous conditions within the furnace, and the temperature of removal from the furnace. They found that spring steels which have a non-scaled, heavily decarburized surface give more efficient quenching than specimens having a thick tenaceous scale and little or no decarburization.

In 1934 Gill and Goodacre (28) conducted tests on patented steel wire. In commercial drawing practices at that time, all wire manufactured for service in the form of rope had a decarburized surface layer. Fatigue tests run at corresponding stress levels indicated that the number of bends for the decarburized wire was higher than the number of bends for wire drawn free from decarburization. Jackson and Pochapsky (44) postulated that fatigue strength was controlled by the strength of the ferrite in the decarburized layer. They found, as did Gill and Goodacre, that decarburization has a lesser effect on the fraction of life degradation at high stress levels than at stress levels near the endurance limit. Jackson and Pochapsky also found that as the core hardness increased, in general, the fatigue life decreased, although the hardness of the decarburized layer remained essentially unchanged.

In 1957 Robinson (61), a supervisor in metallurgy research at General Motors Corporation, challenged the earlier work of Hankins and Becker (32, 33) by pointing out that no finishing was given the decarburized test specimens, while the non-decarburized specimens were machined and polished after the heat treatment. He suggested that a material which is decarburized might be superior to the non-decarburized material at one stress level and inferior at other stress levels.

Spiegler, Weiss, and Taub (67) did extensive research on both decarburized and non-decarburized steels in 1964 and found that while earlier crack formation occured in the decarburized specimens, the decarburization did not affect the crack propagation rate, suggesting that the depth of decarburization has no effect on fatigue strength. This information conflicted with the earlier statements of Cauzaud (20), who reported that fatigue life decreased as the depth of decarburization increased, but did agree with Boegehold (14), who had reported as early as 1937 that a thin decarburized surface layer was just as damaging to fatigue life as a deep decarburized surface layer. Other investigators (17, 60, 66, 68, 70) have stated that decarburization reduces fatigue life, but have provided no data in support of their statements.

In 1974 Shah (64) pointed out in a report involving aircraft accidents that forged parts such as exhaust rocker arms, main rotor drag brace clevices, and spring legs of main landing gears, where a machining operation should have completely removed any surface decarburization, had failed prematurely due to the presence of 0.010 inches (0.3 mm) to 0.024 inches (0.6 mm) of surface decarburization.

Although more than 25 years have passed since the resurgence of interest in fatigue failures during World War II, data from various researchers is still in apparent disagreement. Some of the disagreement is most likely due to inadequate control of variables such as surface roughness, residual stresses, and decarburization depths. However, other data differences are not so simply resolved, partially due to the lack of data, such as using two or three specimens to define the endurance limit and non-analytical curve fitting with a small number of specimens. The work reported here is an attempt to more carefully define the experimental variables and to analyze all data statistically.

Applications of Electron Fractography

Utilization of electron microscopy in failure analysis began about

1950. Although still in its infancy, electron microscopy helps to develop quantitative relationships between microstructure, fracture surface morphology, and mechanical properties measurements (11, 69).

Macro-examination of a fracture surface can establish evidence of gross mechanical abuse, whether excessive corrosion exists, whether there are obvious secondary fractures, whether the origin of the crack can be readily identified, and whether the direction of crack propagation can be easily recognized. Micro-examination can establish the mode of failure: brittle fracture, ductile fracture, or fatigue, as well as determine whether surface discontinuities such as forging laps, secondary cracking, and corrosion pits are present in the surface adjacent to the fracture. X-ray energy dispersion analysis is particularly useful in identifying the composition of constituents, inclusions, and surface residues (7, 10, 11, 13, 38, 69).

Previous Fractographic Fatigue Studies

Establishing the origin of a fracture is essential in failure analysis, and the location of the origin may play a major role in determining what measures should be taken to prevent future fractures. One of the most important characteristic patterns of a fatigue fracture is the presence of fatigue striations. The existence of striations can be regarded as positive proof that a condition of cyclic loading existed; however, the absence of striations should not be interpreted as definite proof that the part did not experience cyclic loading. Some materials (particularly high strength steels) do not readily form fatigue striations (7, 46). Macro-striations such as "beach marks" can trace the crack back to its point of origin, where microscopic examination can ascertain whether initiation resulted from an inclusion, a segregated phase, a machining notch, or some other type of discontinuity. Micro-striation patterns can give a complete history of successive positions of the crack front, provide certain approximations as to the origin of the principal applied stress, determine qualitatively the magnitude of the applied stress, give estimates of crack propagation rates, and help categorize mechanisms of fatigue failure (7, 23, 46, 56).

Laird and Smith (48) suggested, as did Christensen and Harmon (21), that the spacing of a fine initial striation would increase as the depth of the crack increased, due to the increased stress. McMillian and Hertzberg (51) conducted studies on aluminum alloys and found that fatigue cracks propagated in a discontinuous way, a theory later substantiated by Grosskreutz (30) and other researchers (10, 38). Sih, van Elst, and Broek (65) postulated, as did Cottrell (22), that fatigue failure initiated with the nucleation and growth of localized micro-cracks. Others (45, 62) further expanded the crack propagation theory by stating that the controlling parameter in fatigue cracking was the stress intensity factor, K.

During this time much concern developed over the presence of inclusions in aluminum alloys. Pelloux (55) stated that the presence of inclusions, ranging in size from one to ten microns, was known to markedly lower the fatigue strength in steels. He conducted tests on aluminum and found, as did the earlier researchers, that the macroscopic crack propagation rate was higher in "dirty" alloys than in "clean" alloys. Schijve (63) reported that the effect of inclusions on crack propagation in aluminum is small when the crack rate is low, but increases as the propagation rate increases or residual stresses appear. He also found that a crack propagated faster in the less ductile alloys, providing, of course, the manufacturing process was the same. This was in agreement with the earlier findings of Weiss, Niedwiedz, and Breuer (70), who reported the propagation rates in steels increased as the degree of embrittlement increased. Broek (16) indicated that fracture of structural alloys resulted from the initiation and growth of voids at second phase particles, pointing out that the cracking of the particles, ranging in size from one to 20 microns, resulted in a large number of voids forming around the crack tip.

Beachem (12) did extensive work with 2024-T3 aluminum and found that striations occur in patches, separated by abrupt steps. The microscopic crack propagation direction was found to operate several tens of degrees off the macroscopic crack propagation direction. This paralleled the studies of Phillips, his colleagues (57), and Grosskreutz (30), all of whom reported that microscopic crack propagation directions deviated several tens of degrees from the macroscopic direction of crack growth. Paris (54) and researchers at Battelle Memorial Institute (10) pointed out that fatigue cracks tend to grow normal to the direction of principal stress, while striations form parallel to the advancing crack front. Hertzberg (37) stated, as did other investigators (7, 10, 30, 50, 51), that each striation forms during one load cycle and defines the advancing crack front at a point in the fatigue life.

Christensen and Harmon (21) reported that the crack growth rate in an aluminum alloy, for a crack of specific length, was accelerated 20 fold when the applied stress was doubled. They concluded that both the applied stress and the instantaneous crack length must be known to correlate stress amplitude and striation spacing, but two years later in 1969, Pelloux (56) stated that a one to one correlation existed between the spacing of ductile fatigue striations, the stress amplitude, and the maximum stress level.

The surge of activity into the mechanisms of fatigue failure prompted many new theories regarding the fracture process. Almen and Black (3) proposed a three stage fracture process: (1) crystal deformation, (2) crack initiation, and (3) crack propagation. However, McEvily and Johnston (50) maintained that only two stages existed: (1) advancement of the fatigue crack along initiating slip planes, and (2) macroscopic crack propagation at right angles to the maximum normal tensile stress. They suggested, as did researchers at Battelle Memorial Institute (10), that no striations are exhibited in the first stage of fatigue, but are formed in the second stage, where the crack front is advancing. A third theory, proposed by Schijve (63), suggested four stages of fatigue failure: (1) crack initiation, (2) microscopic crack propagation, (3) macroscopic crack propagation, and (4) final failure. A similar theory was developed by Zackay, Gerberich, and Parker (71) which eliminated the final failure stage: (1) crack initiation, (2) stable crack propagation, and (3) unstable catastropic crack propagation. Zackay and associates indicated, as did Grosskreutz (30), that possibly more than one frontal movement of the crack existed during a single fatigue cycle. A fifth fracture process theory was postulated by McMillian and Hertzberg (51) which suggested three stages leading to failure: (1) initiation, (2) plane strain propagation, and (3) plane stress propagation.

One of the more informative discussions concerning fatigue striations was reported by Koterazawa and his colleagues (46). They defined two types of striated appearances: (1) striations with mutually parallel spacings, in which the spacing is approximately equal to the macroscopic crack propagation rate, and (2) "quasi-striation," a term introduced by Beachem (11) in which the patterns are unequally spaced and give no correlation to propagation rates, although the crack propagation rates covered by these patterns is about the same as the mutually parallel striations. Koterazawa and colleagues tested both aluminum alloys and carbon steels and found that in the case of the aluminum alloys, striations covered a large part of the fracture surface, but for the carbon steels, the quasi-striation pattern occupied the major part of the fracture surface. In both cases the area covered by striations decreased with decreasing crack growth rates, due to the increased rubbed area (see Appendix D).

It is apparent from the work reported here that microscopic fatigue mechanisms remain to be adequately researched. Striations have been noted to be both continuous and discontinuous, clearly and poorly defined, straight and smoothly curved. The studies which have to date focused mainly on the aluminum alloys are most likely due to the large usage of aluminum alloys in the manufacture of aircraft and the automotive industry's increased search for high strength to weight ratio materials.

Object

The purpose of this study is then two-fold: (1) to focus new attention on the problem of decarburization, with an emphasis on the quantitative aspect of stress-life relationships in fatigue loading, by defining a rigorous set of experimental parameters and adapting the data to current statistical analysis and curve fitting techniques, and (2) to employ extensive scanning electron fractography in the analysis of the fatigue fracture surfaces in order to obtain needed information concerning the nature and morphology of fatigue fractures present in a medium carbon steel.

CHAPTER 2

EXPERIMENTAL METHODS AND PROCEDURES

Selection of Test Material

SAE 1042, a medium carbon steel widely used in shafting applications, was selected for this study mainly because of its association with fatigue in actual service conditions. The 1/2 inch rounds were purchased in 20 foot lengths in the cold finished condition (see Table 2). All material was from a single heat.

Metallography of the as received (A.R.) microstructure, prior to machining, revealed (1) that no surface decarburization existed, and (2) that the austenite and primary ferrite grain distribution was homogeneous. A calculation of the constituents (at 0.42 weight percent carbon) indicated 54% pearlite and 46% primary ferrite.

Fatigue Test Procedures

Previous researchers have often run less than ten fatigue tests to define a S-N curve. Recognizing the inherent scatter in fatigue data, the author decided at the onset of the study to run a minimum of 40 fatigue tests for each S-N curve in order to give a complete and well-documented fatigue life history at all stress levels. A minimum of two tests were run at each stress level, the stress level increments being approximately 3000 psi (21 MN/m^2).

TABLE 2

NOMINAL COMPOSITION OF SAE 1042 STEEL
(Weight Percent)

C	Pmax	Mn	Smax
0.40-0.47	0.04	0.60-0.90	0.05

Test equipment. Fatigue tests were run on a R. R. Moore rotating-beam fatigue testing machine, which provided completely reversed bending of the test specimens. A stress cycle indicative of the rotating-beam test is shown in Figure 1. The minimum allowable stress, which was determined by the machine design, was approximately 18000 psi (124 MN/m^2), and the maximum attainable speed, under no load conditions, was approximately 14000 cpm.

Testing parameters. Failure was defined as the complete separation of the test specimen, in accordance with ASTM standards (9). The endurance limit was defined as 10^8 cycles; all tests in which the specimens remained unbroken after 10^8 cycles were discontinued. Although the testing speeds ranged from 9000 cpm to 12000 cpm (depending on the loads applied), previous researchers (24, 47, 53) found the endurance limit was

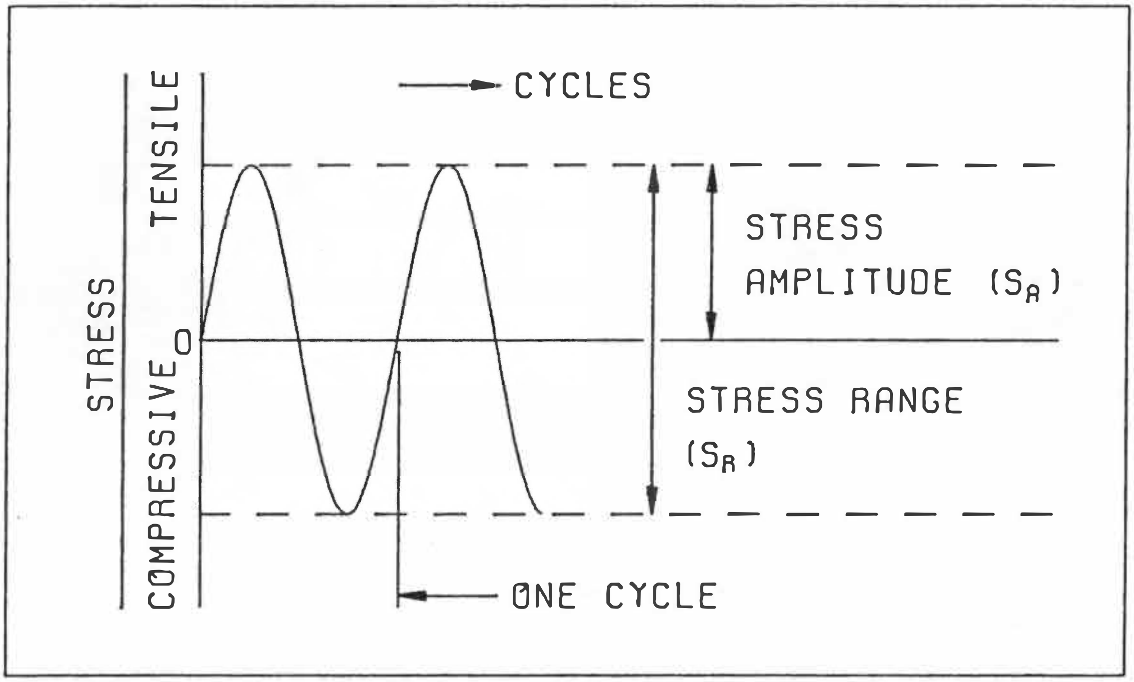

Figure 1. Typical Stress Cycle of a Rotating-Beam Fatigue Test.

not affected by testing speeds in this range. The nominal surface finish for all D-1, D-8, and D-24 fatigue specimens was 20 micro-inches, arithmetical average (AA). Testing was conducted at normal atmospheric conditions (room temperature: 70°F or 21°C).

Preparation of the Fatigue Specimens

Initial machining. Initial machining of the continuous radius (9) was produced on a tracer lathe. Dimensions of the minimum diameters ranged from 0.300 inches (7.62 mm) to 0.303 inches (7.70 mm) with an initial nominal surface roughness of 100 micro-inches, AA.

Decarburization. Three test series were selected for studying the effects of decarburization on fatigue life: (1) specimens having no surface decarburization (series D-1), (2) specimens having a 0.038 inch (0.97 mm) decarburized surface layer (series D-8), and (3) specimens having a 0.080 inch (2.03 mm) decarburized surface layer (series D-24). Although Shah (64) reported that decarburization depths of 0.01 inches (0.3 mm) were considered detrimental to fatigue life, the more than significant amounts of decarburization encountered here were selected for two reasons: (1) due to the oxidizing atmosphere used in the decarburization process, a thick scale (see Table 3) had to be removed prior to testing, which involved removing some of the ferrite layer; and (2) because a hand finishing operation was required, variation in the

TABLE 3

HEAT TREATMENT SPECIFICATIONS

Test Series	Austenite Grain Size at Specimen Center	Depth of Surface Decarburization, inches (mm)	Oxide Thickness, inches (mm)
A.R.	8	0.000 (0.00)	0.000 (0.00)
D-1	10	0.000 (0.00)	0.000-0.001 (0.00-0.03)
D-8	10	0.038 (0.97)	0.002-0.005 (0.05-0.13)
D-24	10	0.080 (2.03)	0.009-0.014 (0.23-0.36)

finished diameters resulting from the polishing would have produced large percentage differences in the decarburization depths of specimens with small decarburized layers (0.005 inches or 0.13 mm, for example).

All fatigue specimens were placed in a furnace preheated to 1550°F (843°C) in lots of twenty. An uncontrolled furnance atmosphere was used to obtain the decarburization. Specimens were placed vertically in a decarburized SAE 1018 steel plate in holes two inches on center. The first series (D-1) was placed in the furnace for one hour, the second series (D-8) was placed in the furnace for eight hours, and the third series (D-24) was placed in the furnace for 24 hours. Upon removal from the furnace, each lot was allowed to air cool to room temperature (70°F or 21°C).

Scale removal and final finishing. Due to the nature of the oxidizing atmosphere, an oxide layer had to be removed after decarburization and subsequent normalization. A sharp blow to the specimen end, in general, caused the scale to flake off. Coarse emery paper (1/0) was used to remove any remaining scale, followed by 2/0 and 3/0 emery paper to produce the final finish. Previous investigators (24, 34) stated that finishing with 2/0 emery paper was standard procedure for fatigue specimens; however, Moore and Alleman (52) suggested using 3/0 emery paper for the final polishing.

The circumferential polishing was performed by chucking the specimen in a lathe and rotating at approximately 100 rpm, taking care to insure no significant temperature rise resulted in the specimen during the process.

Preparation of the Tensile Specimens and Procedures for Their Testing

To aid in the study of the effects of decarburization, tensile properties were obtained from tensile specimens, designated D-1, D-8, and D-24, which had been given the same heat treatment as their respective D-1, D-8, and D-24 fatigue specimens. These specimens, which were machined according to ASTM standards (8), were finished in the same manner as described in the previous section on scale removal and finishing. However, the decarburized surface layer of two of the four specimens from each of the D-8 and D-24 heat treatments was removed by machining prior to testing. This enabled obtaining tensile properties of specimens having D-8 and D-24 heat treatments, but no decarburization.

Tensile tests were conducted on an Instron tensile testing machine, using a strain rate of 0.02 inches (0.5 mm) per minute.

Determination of Decarburization Depths

Light microscopy. Light microscopy of the test specimens yielded three important findings: (1) the austenite grain size of the core microstructure showed no appreciable change with furnace times up to 24 hours, (2) examination of the surface microstructure provided a straightforward method for determining decarburization depths, and

(3) examination of unetched specimens with magnifications up to 500x revealed no intergranular oxides.

Figures 2, 3, and 4 show, respectively, the core microstructures of typical D-1, D-8, and D-24 test specimens. Two methods were used to determine the austenite grain size of the core microstructure: (1) a measurement of the number of grains per square inch at 100x, and (2) a comparison of the austenite grain size at 100x with ASTM standards. In both procedures the austenite grain size of all test specimens was ASTM 10 (see Table 3).

Figure 5 shows the surface microstructure of a typical D-1 test specimen. The micrograph clearly indicates that no surface decarburization exists. Figures 6 and 7 show, respectively, the decarburization depths of typical D-8 and D-24 test specimens. The specks visible in the ferrite grains of Figures 6 and 7 are etch pits.

Because intergranular oxidation was not found in the specimens, no micrograph was published; however, an explanation is in order. As previously mentioned in Chapter 1, intergranular oxidation normally occurs above 1740^{o}F (950^{o}C) (42). The maximum temperature used for decarburization in this work was 1550^{o}F (843^{o}C). If some grain boundary oxidation did occur, it was removed along with the outer portion of the ferrite layer during the scale removal and polishing.

Microhardness traverses. Although a good approximation of the

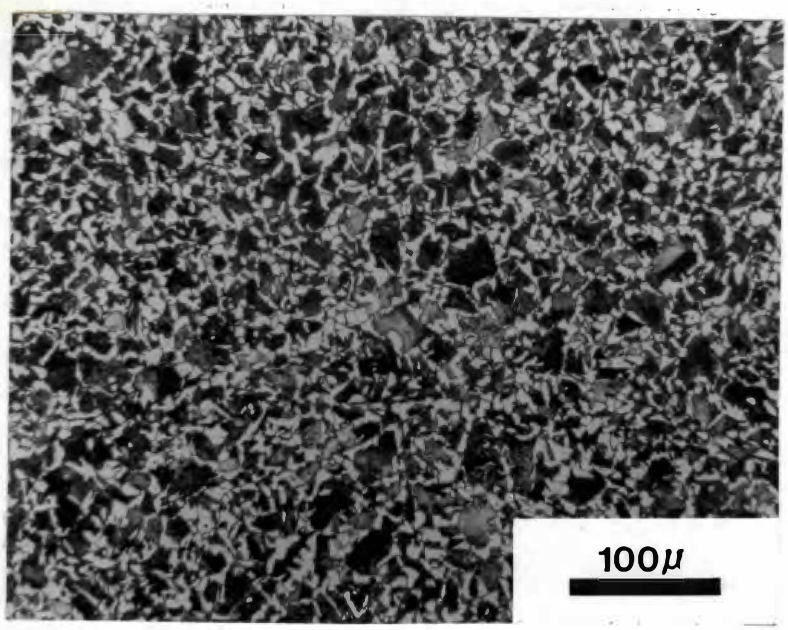

Figure 2. Light Micrograph Showing the Core Microstructure, ASTM 10, of a Typical D-1 Test Specimen. 200x.

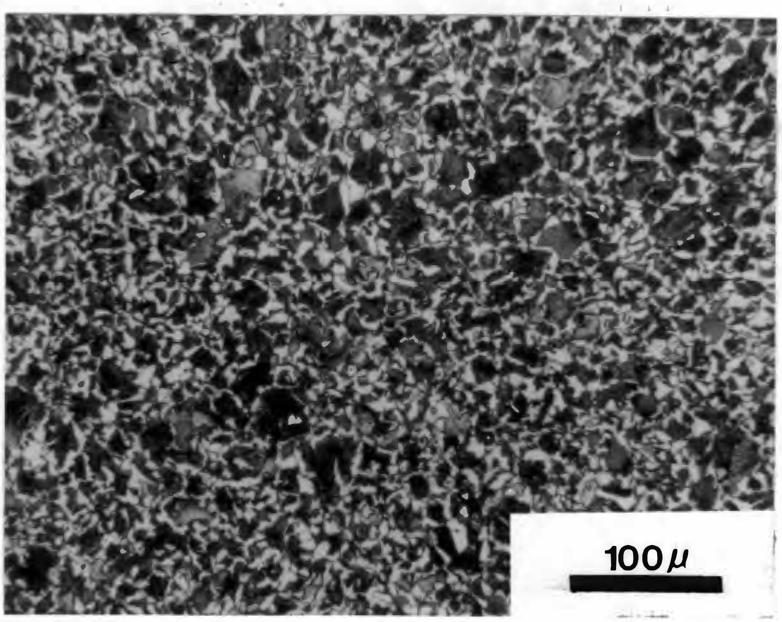

Figure 3. Light Micrograph Showing the Core Microstructure, ASTM 10, of a Typical D-8 Test Specimen. 200x.

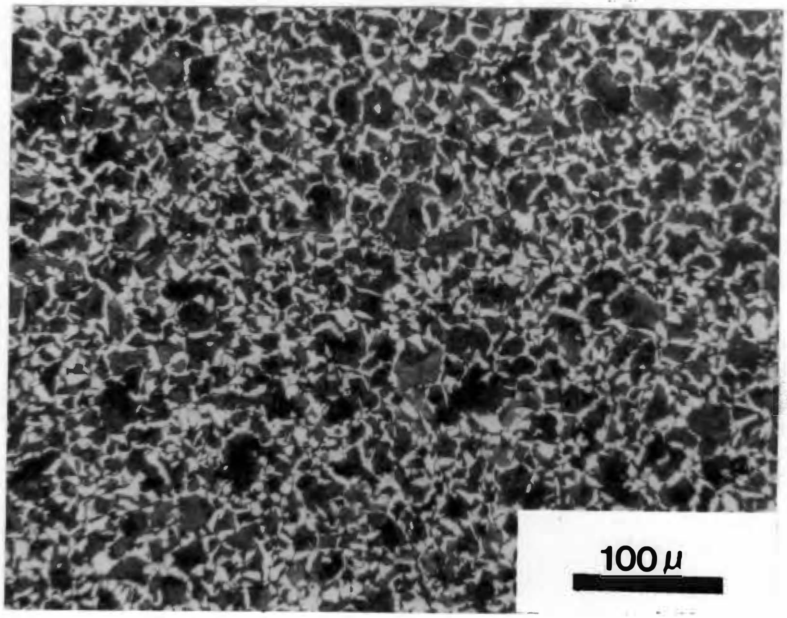

Figure 4. Light Micrograph Showing the Core Microstructure, ASTM 10, of a Typical D-24 Test Specimen. 200x.

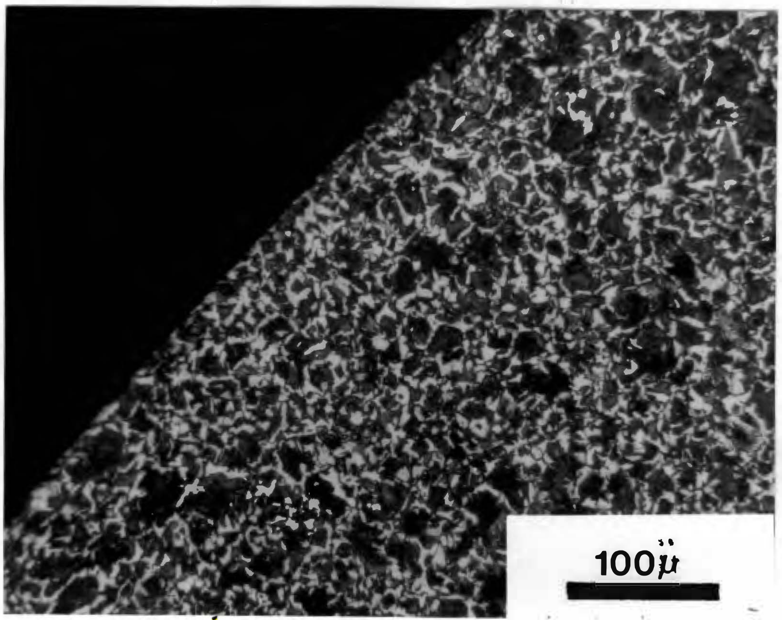

Figure 5. Light Micrograph Showing the Edge Microstructure of a Typical D-1 Test Specimen. 200x.

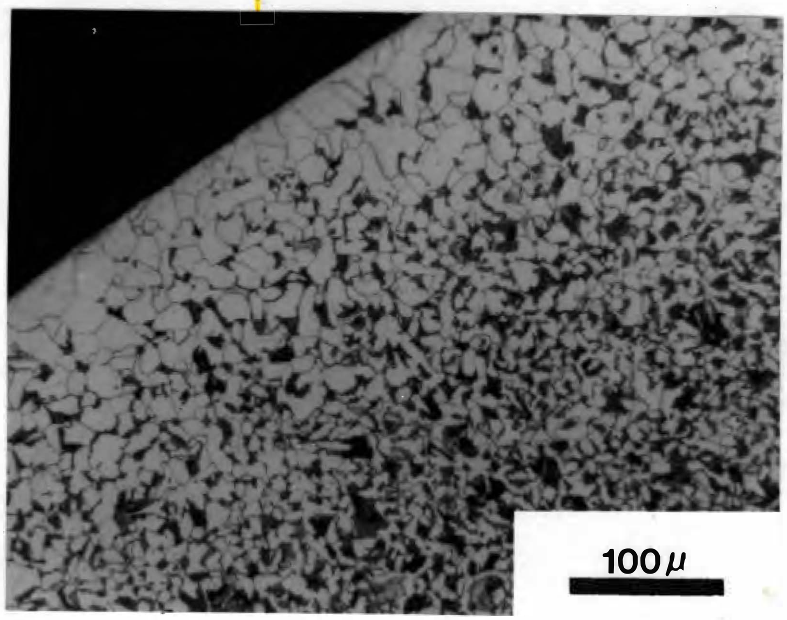

Figure 6. Light Micrograph Showing the Edge Microstructure of a Typical D-8 Test Specimen. 200x.

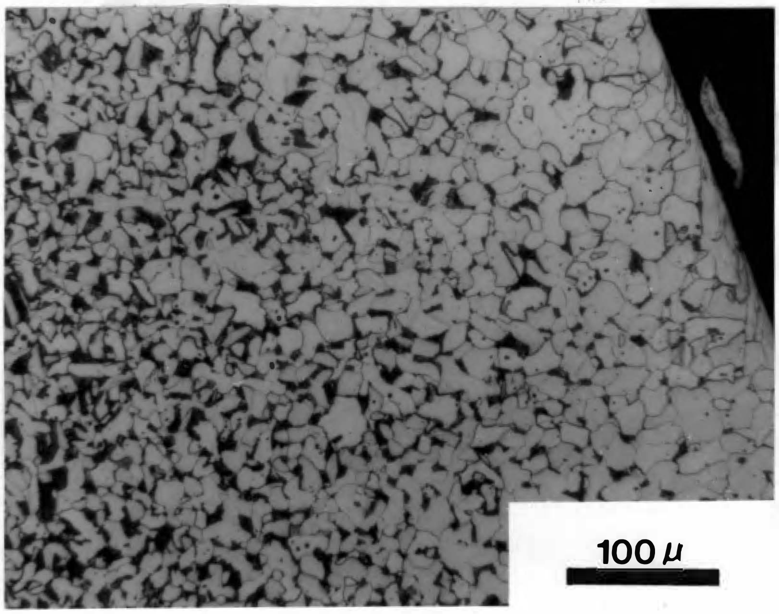

Figure 7. Light Micrograph Showing the Edge Microstructure of a Typical D-24 Test Specimen. 200x.

decarburization depths (such as the free ferrite depth) can be obtained by optical microscopy, a quantitative measure of the decarburization depth is needed for quantitative correlations of decarburization with fatigue life. Several criteria are possible. For purposes of this study, the decarburization depth is defined as that depth to which the hardness is lower than the core hardness. This depth is then the total affected layer rather than the free ferrite layer.

Seven fatigue test specimens, or approximately 15% of the 50 specimens per test set, were randomly selected from each fatigue test set for use in obtaining the microhardness data. These specimens were sectioned at the minimum diameter, mounted, and polished. Microhardness readings were taken in increments of 0.003 inches (0.08 mm) until a constant hardness reading was attained, at which time the incremental spacing was increased to 0.005 inches (0.13 mm) for the remainder of the traverse. The data was then applied to a statistical analysis computer program (a least squares regression analysis). A subsequent curve fitting program produced a schematic representation of the original data and the predicted curves (see Figure 8). Decarburization depths were defined as the points at which the D-8 and D-24 hardness curves intersected the D-1 curve (see Table 3, page 22). As indicated in Figures 6 and 7, these depths were not completely carbon-free.

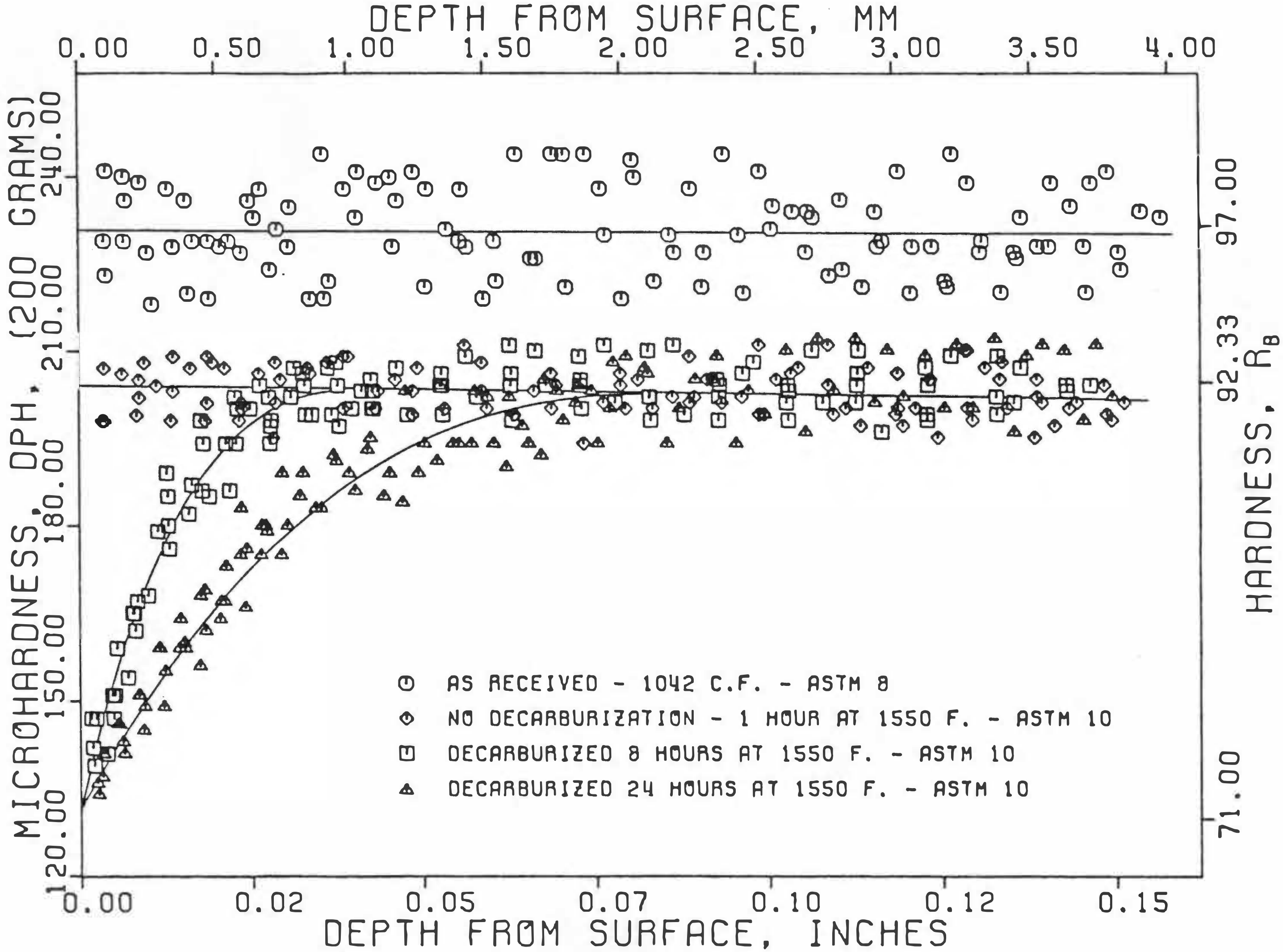

Figure 8. Typical Decarburization Depths as Determined by Hardness.

Surface Roughness Measurements

Although previous studies frequently described machining operations and polishing techniques used in specimen preparation, very few authors reported the actual surface roughness. Several indexes have been used in the past, the most common being the root mean square (RMS). In 1962 the arithmetical average (AA) index was adopted as the standard for surface roughness measurements, although for surface roughness purposes the AA--center line average (CLA) if using the equivalent British index--and the RMS have a negligible difference (15).

A Tally-Surf gage was used to give accurate surface roughness readings of the surface finishes produced by initial machining and final polishing processes (see Figures 9 and 10).

The Tally-Surf, or profilometer, consists of a diamond stylus which traverses along the longitudinal axis of the specimen. A motion of the stylus distorts a Piezo crystal, which generates a minute electric current proportional to the distortion. The current is amplified and conducted to a second Piezo crystal which distorts and moves the pen on a moving chart (see Figure 11). The arithmetical average value is read directly from a meter calibrated in micro-inches.

Arithmetical average is defined as the deviation of the surface from the mean surface. Figures 12 and 13 show, respectively, schematic representations of the mean surface and the derivation of arithmetical average.

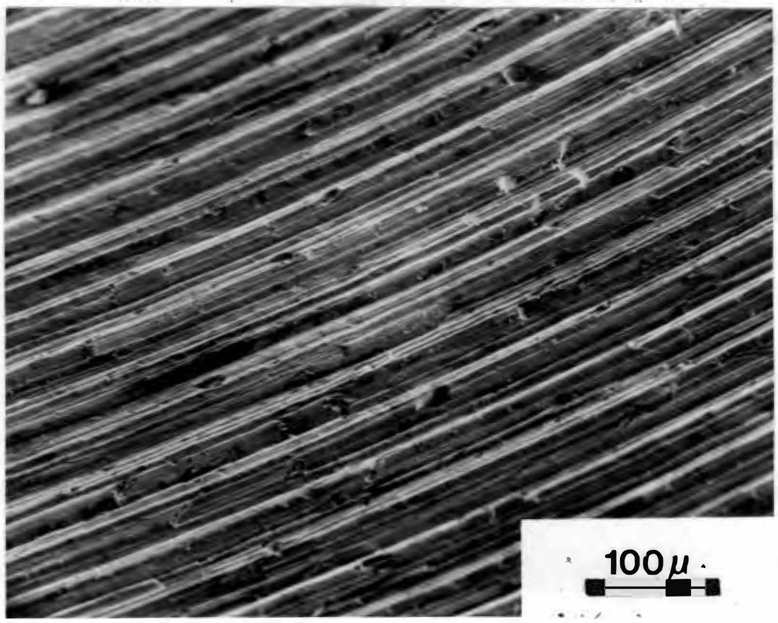

Figure 9. SEM Micrograph of Lathe Marks Resulting from Initial Machining. 170x.

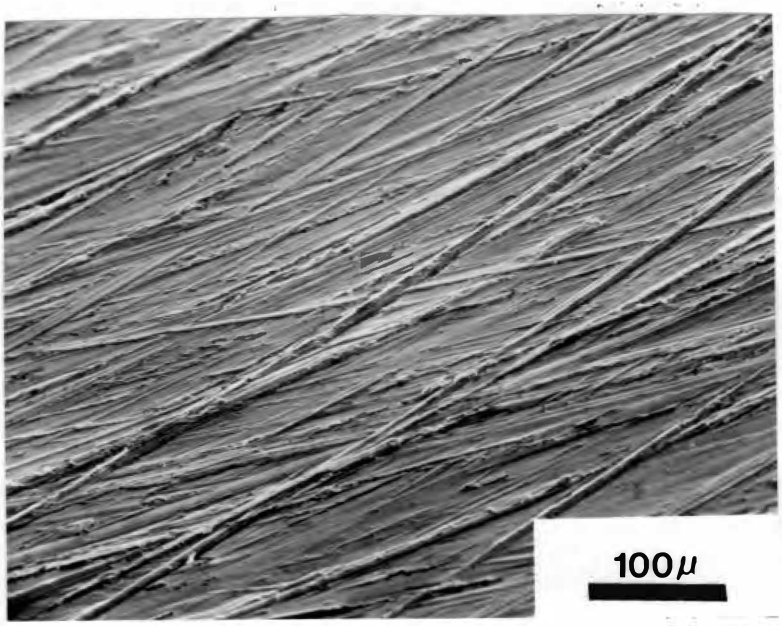

Figure 10. SEM Micrograph Showing Typical Finishing Marks of D-1, D-8, and D-24 Fatigue Test Specimens. 180x.

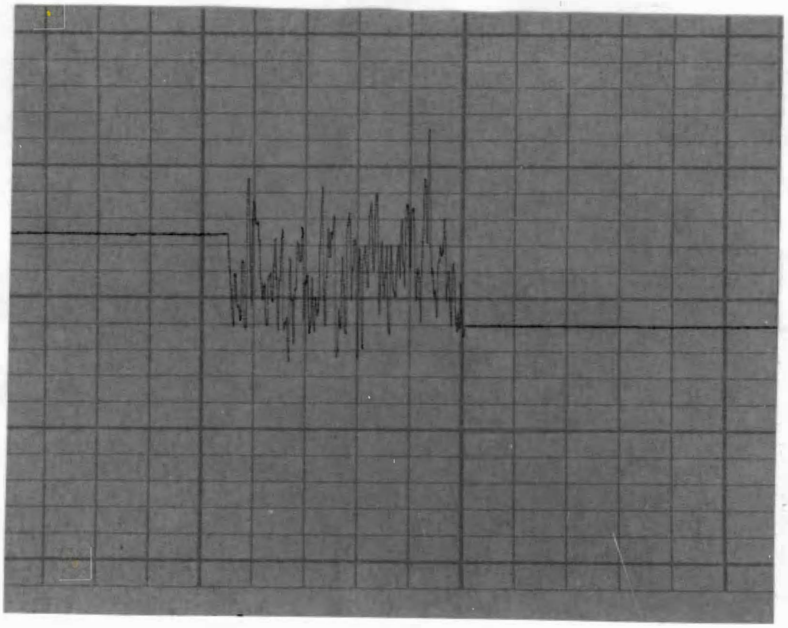

A. 100 μ-in, AA (Full Scale: 200 μ-in, AA).

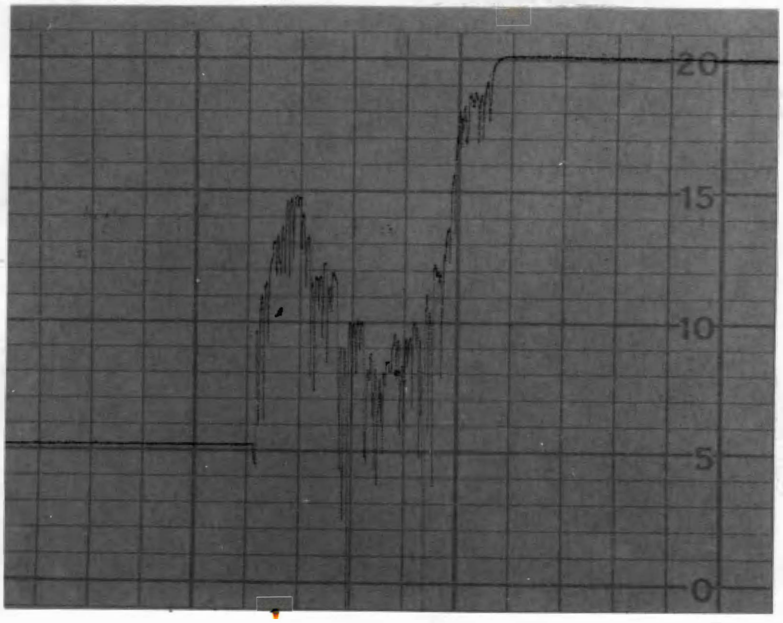

B. 20 μ-in, AA (Full Scale: 40 μ-in, AA).

Figure 11. Photomacrographs of Typical Surface Roughness Measurements as Recorded by the Profilometer.

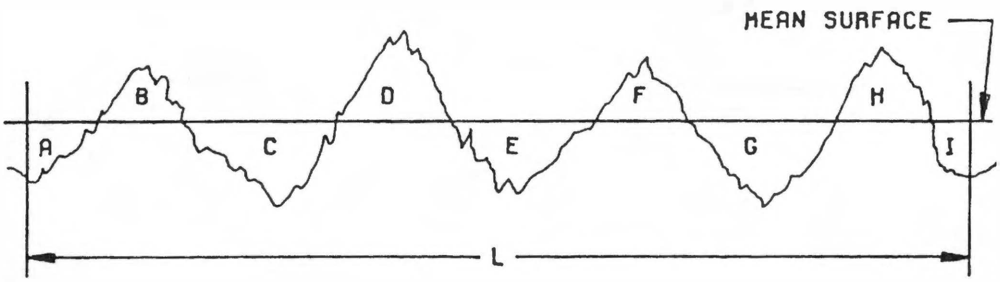

OVER A LENGTH OF SURFACE L, THE MEAN SURFACE IS A LINE DRAWN SUCH THAT THE SUM OF THE AREAS EMBRACED BY THE SURFACE PROFILE ABOVE THE LINE IS EQUAL TO THE SUM OF THOSE BELOW THE LINE.

AREAS B + D + F + H = AREAS A + C + E + G + I.

Figure 12. Definition of Mean Surface.

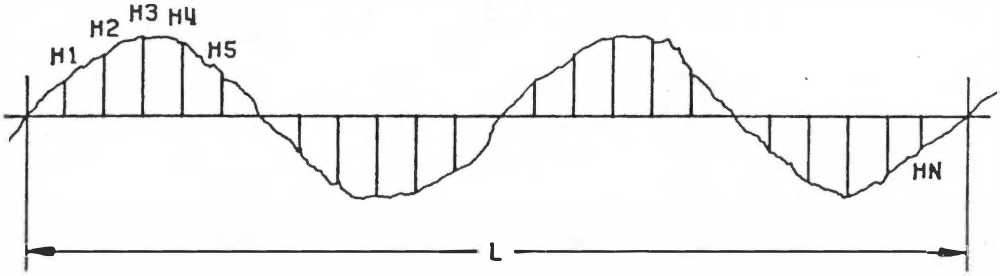

THE AA VALUE OF THE SURFACE IS THE AVERAGE HEIGHT OF THE PROFILE ABOVE AND BELOW THE MEAN SURFACE.

$$AA = \frac{H1 + H2 + H3 - - - HN}{L} = \frac{1}{L}\int_{L}^{ZERO} HNDL$$

WHERE H IS THE HEIGHT OF THE PROFILE ABOVE OR BELOW THE MEAN SURFACE AT POINTS AT UNIT DISTANCES APART.

L UNITS = SAMPLING LENGTH

Figure 13. Derivation of Arithmetical Average Surface Roughness.

Surface roughness measurements were conducted on ten fatigue test specimens from each series, or on approximately 25% of all fatigue specimens. The specimens were randomly selected after completion of each S-N curve, since measurement of the surface roughness prior to testing could have resulted in the profilometer's diamond stylus altering the surface finish of approximately 25% of the specimens (see Table 4).

Fractography of the Test Specimens

Fractographic analysis involved both macro- and micro-examination of the fractured tensile and fatigue specimens. Fractured fatigue specimens were examined macroscopically to identify any correlation between fracture surface appearance and applied stress.

Microscopic examination involved both light microscopy and scanning electron microscopy (SEM). The primary concern of the light microscopy was to determine whether the mode of cracking associated with fatigue failure was transgranular or intergranular, whether deformation was present along the crack, whether intergranular oxides were present, and whether surface scale removal was complete.

SEM observation with its high resolving power and in situ chemical analysis was used to characterize the fractographic features of the test specimens: crack initiation site, influence and compositions of inclusions, crack propagation direction, and striation development.

TABLE 4

FATIGUE TEST SPECIMEN SPECIFICATIONS

Test Series	Number of S-N Tests	Arithmetical Average Surface Roughness, micro-inches (microns)	Minimum Diameter, inches (mm)
A.R.	45	100 ± 20 (0.25 ± 0.05)	0.300 (7.62)
D-1	45	20 ± 4 (0.05 ± 0.01)	0.299-0.303 (7.59-7.70)
D-8	41	20 ± 4 (0.05 ± 0.01)	0.285-0.298 (7.24-7.57)
D-24	41	20 ± 4 (0.05 ± 0.01)	0.269-0.283 (6.83-7.19)

Statistical Data Analysis

All microhardness and fatigue test data were analyzed using a statistical analysis system (SAS) computer program which consisted of eight individual data sets, one data set for each of the four microhardness curves and one data set for each of the four S-N curves. The order of the polynominal for each data set was predicted from a least squares regression analysis which weighted each data point in each data set equally.

The two most important characteristics of the SAS regression analysis are the R-Square value and the PR > F value. The R-Square value is the ratio of the sums of the squares of the regression to the sums of the squares of the original data. The PR > F value is the level of significance associated with the F value and the corresponding degree of freedom for that F value. When the PR > F value is equal to or greater than 0.001, the error in the regression becomes significant. The ideal situation would exist when the R-Square value equalled 1.0, as would be the case if the sums of the squares of the regression equalled the sums of the squares of the original data. As the order of the polynominal increases, the R-Square value increases, but the PR > F value may also increase; therefore, the order of the polynominal which best fits the data is the polynominal which has the highest R-Square value with a PR > F value below 0.001.

The SAS program used in this study listed three regressions for each data set: the first regression was one order below the predicted polynominal, the second regression was the predicted polynominal, and the third regression was one order higher than the predicted polynominal and indicated a higher order polynominal was not acceptable.

Curve Fitting and Plotting Techniques

After the orders of the predicted polynominals for the eight data sets were obtained (see Appendix A), the information was then added to a Calcomp plotting program (see Appendix B) which drew multiple curves of the microhardness data as well as the S-N data and wrote the equation for each curve; however, the presence of non-essential information rendered the data unpresentable for publishing. Hence, two additional sets of data were drawn using a different subroutine, having legends, but no curves or equations. Curves for these data (Figure 8 on page 31, for example) were hand drawn using superpositioning.

CHAPTER 3

RESULTS OF THE FATIGUE TESTS

Introduction

As stated in Chapter 2 in the Fatigue Test Procedures, a decision was made initially to run the fatigue tests at stress level increments of 3000 psi (21 MN/m^2). This proved satisfactory at high stresses, but as the applied stress neared the endurance limit of each S-N curve, it became necessary to adjust the stress level increment in order to adequately define the complete fatigue curve (see Figure 14). Notice that no definite break occurs in the S-N curves shown here as is commonly shown in published literature for plain carbon steels, where often less than ten fatigue tests define a complete S-N curve (25, 26, 27, 44, 52, 53, 67, 70).

Two fatigue tests normally defined a stress level; however, if fracture occurred outside the 10-20% variation normally observed in fatigue testing (19), a third test was run at the stress level in question. The applied stress of the D-1, D-8, and D-24 fatigue specimens ranged from a maximum stress of 86014 psi (593 MN/m^2) (83% of the D-1 UTS and 128% of the D-1 YS) to a minimum stress of 28035 psi (193 MN/m^2) (31% of the D-24 UTS and 46% of the D-24 YS). One other S-N curve was run, that of SAE 1042 steel in the as received condition (A.R.), to obtain initial testing parameters for the fatigue tests. The applied stresses for this particular S-N curve ranged from 95064 psi (655 MN/m^2) (85% of the A.R. UTS and

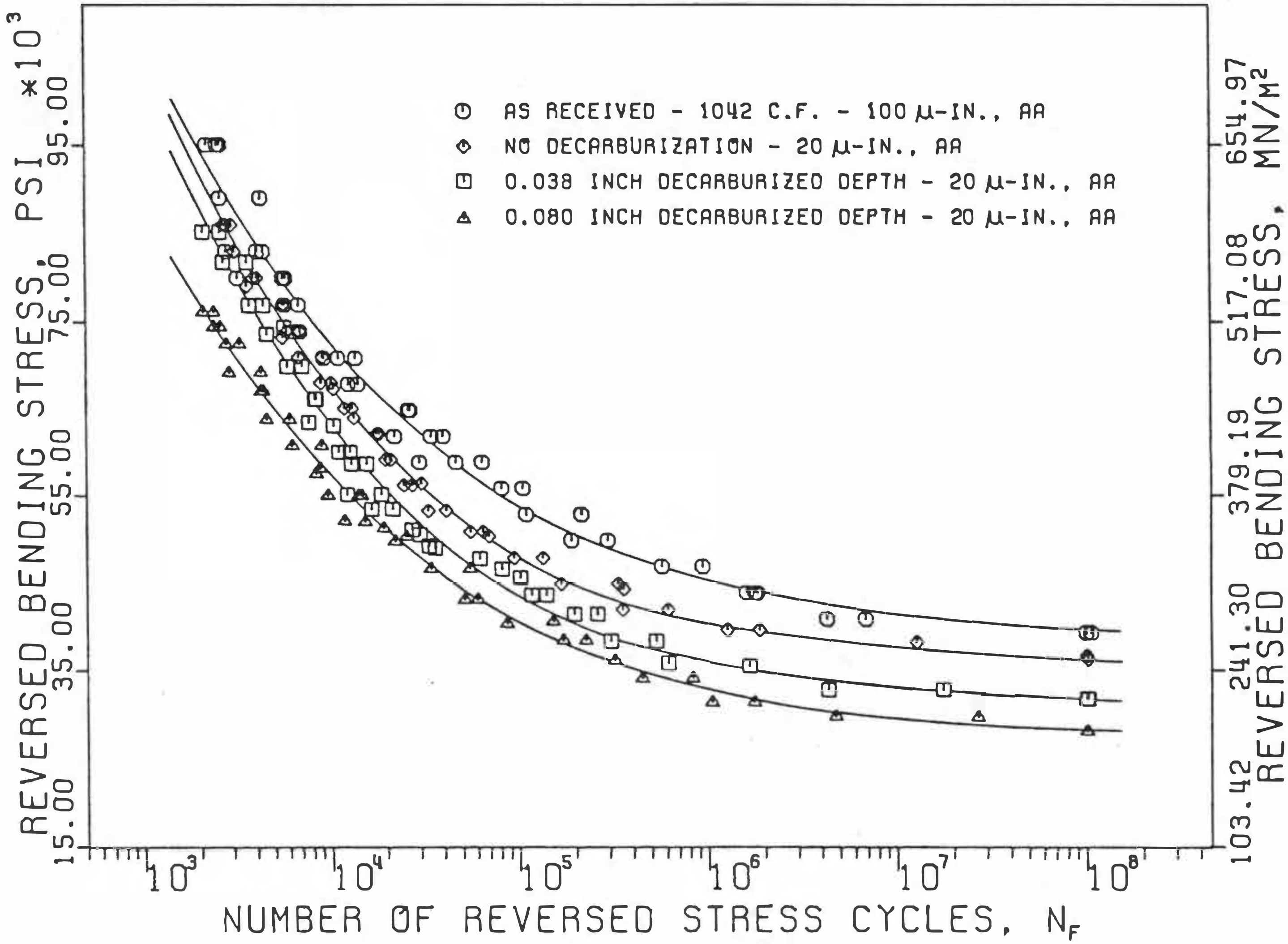

Figure 14. Effect of Surface Decarburization on the Fatigue Life of SAE 1042 Steel.

103% of the A.R. YS) to 39235 psi (271 MN/m^2) (35% of the A.R. UTS and 42% of the A.R. YS).

Effect of Increasing the Decarburization Depth

As illustrated in Figure 14, not only does the initial decarburization reduce fatigue life and fatigue strength, but a continued increase in the depth of decarburization further decreases these quantities. While Figure 14 shows, schematically, the damage caused by decarburization, the fatigue test results are best explained by comparing the degradation in fatigue life for the D-1, D-8, and D-24 S-N curves at incremental levels of stress (see Table 5).

At stress levels of 60000 psi (414 MN/m^2), 55000 psi (379 MN/m^2), and 50000 psi (345 MN/m^2) the percentage differences from the D-1 to D-8 curves and the D-8 to D-24 curves show very little change, but as the endurance limit is approached the percentage differences increase rapidly. While the point of intersection of the S-N curves is not obvious in Figure 14, Appendix C shows that the A.R., D-1, and D-8 curves intersect at 1.2×10^5 psi (827 MN/m^2); the stress which corresponds to the same N_f value on the D-24 curve is 1.0×10^5 psi (689 MN/m^2). A visual comparison of the curves in Figure 14 shows that as the stress decreases, the curves begin to spread apart, demonstrating that decarburization has a much greater effect at low stress levels.

One of the startling observations from Table 5 is the extent of the

TABLE 5

REDUCTION IN FATIGUE LIFE DUE TO SURFACE DECARBURIZATION

Stress, psi (MN/m^2)	S-N Comparisons X		Y	Percentage Change in Fatigue Life*
60000	D-1	to	D-8	-42%
(414)	D-8	to	D-24	-37%
	D-1	to	D-24	-64%
55000	D-1	to	D-8	-44%
(379)	D-8	to	D-24	-38%
	D-1	to	D-24	-65%
50000	D-1	to	D-8	-49%
(345)	D-8	to	D-24	-39%
	D-1	to	D-24	-69%
45000	D-1	to	D-8	-65%
(310)	D-8	to	D-24	-40%
	D-1	to	D-24	-79%
40000	D-1	to	D-8	-90%
(276)	D-8	to	D-24	-50%
	D-1	to	D-24	-95%
36500	D-1	to	D-8	-99%
(252)	D-8	to	D-24	-70%
	D-1	to	D-24	-100%

*Percentage = $[(X-Y)/X] \cdot 100$

damage which results from the initial decarburization. Although the D-24 specimens have more than double the amount of decarburization which the D-8 specimens have, the percentage differences of the D-1 to D-8 comparisons are, in all cases, greater than the percentage differences of the D-8 to D-24 comparisons. To further substanstiate this observation, a ratio of the percentage differences of the D-1 to D-8 curves to the D-1 to D-24 curves indicates that at all stress levels in Table 5 this value equals, or exceeds, 67%, demonstrating that over 2/3 of the total damage resulted from the initial decarburized surface layer.

Endurance limit stresses (Se) of the four S-N curves are as follows:

(1) A.R. curve: 39235 psi (271 MN/m^2) (35% of the A.R. UTS and 42% of the A.R. YS).

(2) D-1 curve: 36217 psi (250 MN/m^2) (35% of the D-1 UTS and 54% of the D-1 YS).

(3) D-8 curve: 31741 psi (219 MN/m^2) (31% of the D-1 UTS and 47% of the D-1 YS).

(4) D-24 curve: 28035 psi (193 MN/m^2) (27% of the D-1 UTS and 42% of the D-1 YS).

The percentage decrease from the D-1 Se to the D-8 Se is 12.4%, the decrease from the D-8 Se to the D-24 Se is 11.7%, and the overall percentage decrease due to decarburization is 22.7% (D-1 Se to D-24 Se). Note that all endurance limit stresses (Se) are within 10-40% of the UTS (the endurance limit stress range previously reported in Chapter 1, under Macroscopic parameters).

The fatigue strength data, although less pronounced than the fatigue life data, indicates the initial surface decarburization to be more detrimental than doubling the decarburization depth.

Fatigue Cracking Modes

In some of the previous studies, researchers were concerned with the presence of intergranular oxidation, which has been postulated to result in intergranular cracking and concurrent degradation in life. However, as stated earlier in Chapter 2 in Determination of Decarburization Depths, under Light microscopy, by criterion of optical metallographic examination, no intergranular oxidation was observed.

The fatigue specimens examined in this study exhibited primarily transgranular cracking (see Figure 15). The crack shown in Figure 15, which was observed in a D-24 specimen, runs parallel to the fracture surface, or normal to the longitudinal axis of the test specimen, and, therefore, normal to the maximum principal stress. The micrograph clearly illustrates that the crack initiated in the decarburized surface layer and propagated inward toward the core microstructure. Deformation is visible along the boundaries of the crack and around the crack tip. Aita and Weertman (1) conducted studies in two phase Fe-C alloys and found that the fatigue crack takes the path of easiest slip and

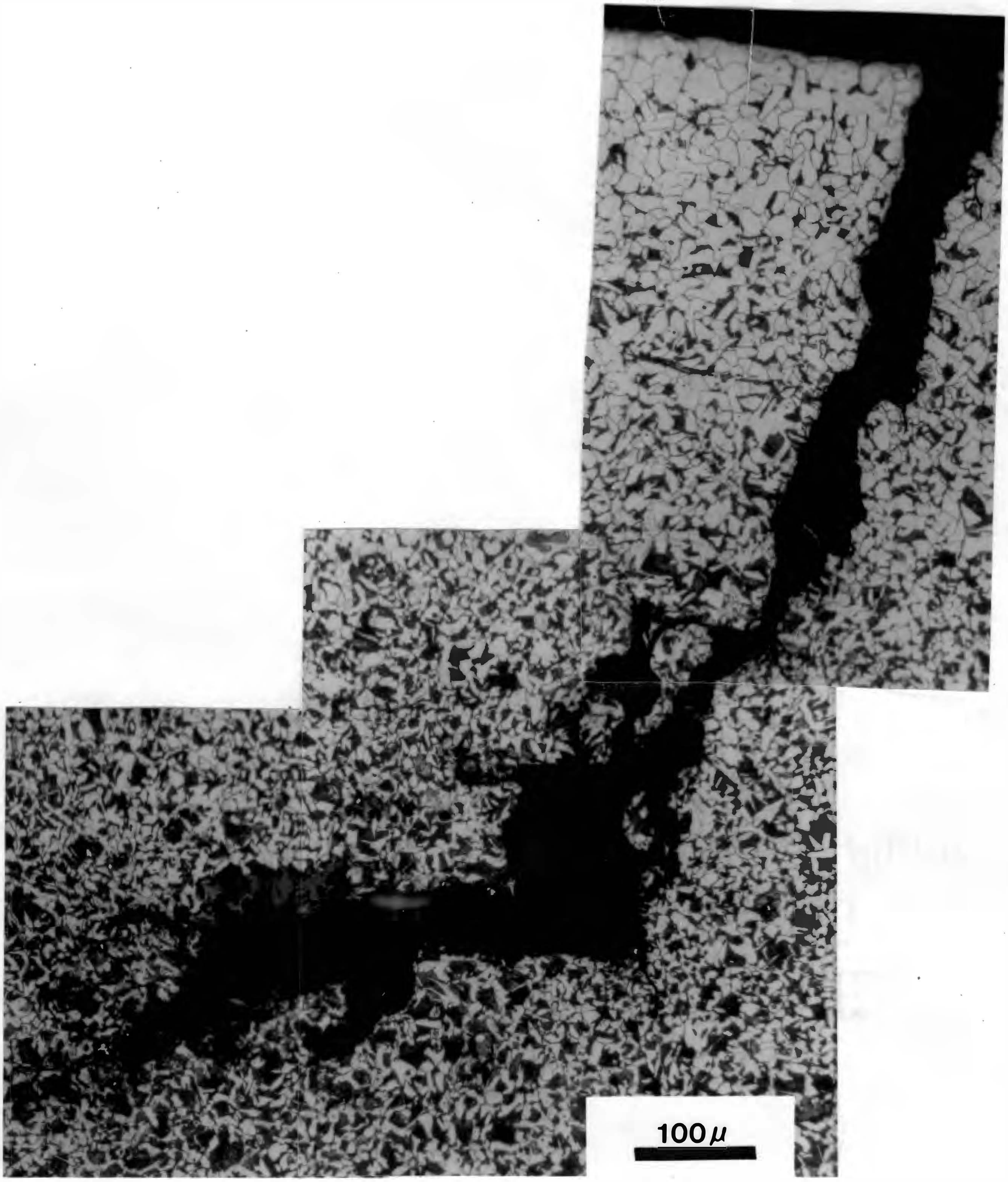

Figure 15. Light Micrograph Showing Transgranular Cracking of a D-24 Fatigue Test Specimen. 200x.

grows in the ferrite whenever possible. At low stresses the brittle second phase is avoided, but at high stresses brittle fracture of the second phase occurs ahead of the main crack. They also found the predominant mode of cracking to be transgranular.

The Influence of Circumferential Finish Marks

Careful examination of the areas below the fracture surfaces revealed that cracking initiated in the valleys of the circumferential finish marks produced by the polishing process (see Figure 16). Since all D-1, D-8, and D-24 specimens were finished in the same manner, the results should show no variation due to this phenomenon.

Discussion

With the exception of the depth of decarburization, all metallurgical variables were held constant: core grain size, core hardness, and core microstructure. The mechanical specimen preparation procedure was also held constant so that all specimens presumably had the same residual stress pattern and the same surface roughness. Metallographic examination showed that surface scale removal was complete and that there was no intergranular oxidation. It also showed the ferrite morphology to be non-columnar.

The only testing variable not held constant was the loading rate, but data indicate, as pointed out earlier, that this was not a variable for the

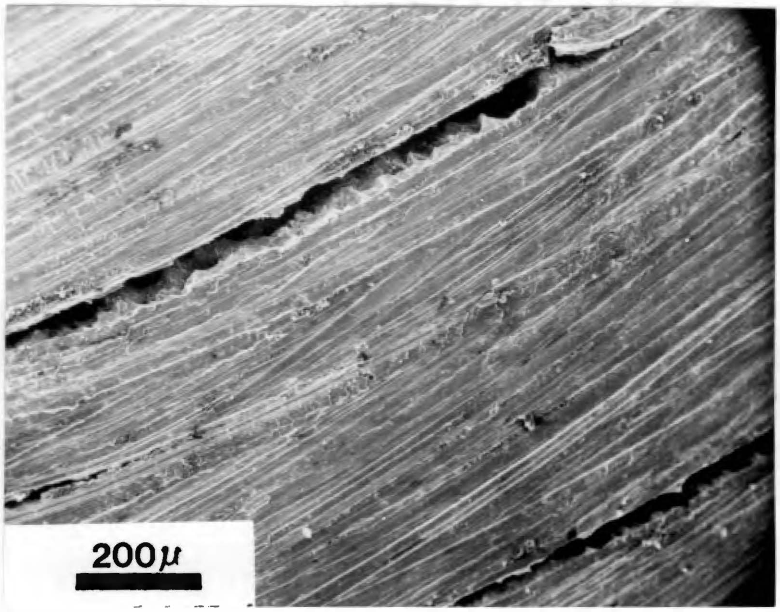

Figure 16. SEM Micrograph Showing Cracking Along Circumferential Finishing Marks. 85x.

loading rates employed. Consequently, any observed degradation in fatigue life is assumed to be due to only the depth of decarburization.

A comparison of the arithmetic differences in the endurance limit stresses (Se) shows a 4% decrease from the D-1 to D-8 curves and a 8% decrease from the D-1 to D-24 curves; however, delta percentage differences at the endurance limit stresses indicate a 12% decrease from the D-1 to D-8 curves and a 23% decrease from the D-1 to D-24 curves, emphasizing the importance of clarifying the comparisons used when reporting quantitative data.

CHAPTER 4

THE TENSILE PROPERTIES TESTS

Introduction

To help determine the total effects of decarburization, tensile properties were obtained from A.R., D-1, D-8, and D-24 specimens which had the same heat treatments and decarburization depths as their respective fatigue specimens. Additional testing was performed on specimens which had D-8 and D-24 heat treatments, but which also had had the decarburized surface layers removed by machining prior to testing (see Table 6).

Two specimens were tested for each designation. The two numbers to the right of the tensile property represent the two specimens; the order in which the numbers are listed is indictive of the specimen number. Hence, the lower yield stress of the first test specimen having a 0.038 inch (0.97 mm) decarburized surface layer is 64108 psi (442 MN/m^2), and the ultimate tensile stress of the same specimen is 100691 psi (694 MN/m^2).

A Comparison of the Decarburized and Non-Decarburized Test Results

A comparison of columns 2, 5, and 6 indicates that as the decarburization depth increases from no decarburization to 0.038 inches (0.97 mm) the UTS decreases by 3968 psi (27 MN/m^2) (3.8%), and increasing the decarburization depth from 0.038 inches to 0.080 inches

TABLE 6

EFFECT OF SURFACE DECARBURIZATION ON TENSILE PROPERTIES

Tensile Property	A.R. (C.F.) No Decarb	D-1 No Decarb	D-8 No Decarb	D-24 No Decarb	D-8 0.038 Inch Decarb	D-24 0.080 Inch Decarb
Ultimate Tensile Strength, psi (MN/m^2)	111421 (768)	103962 (717)	102739 (708)	103650 (715)	100691 (694)	90920 (627)
	111006 (765)	103430 (713)	101501 (700)	102818 (709)	98764 (681)	90057 (621)
Upper Yield Strength, psi (MN/m^2)	-- --	70194 (484)	69792 (481)	69820 (481)	68814 (474)	62851 (433)
	-- --	68386 (471)	68514 (472)	69491 (479)	68731 (474)	61251 (422)
Lower Yield Strength, psi (MN/m^2)	-- --	65940 (455)	64762 (446)	64601 (445)	64108 (442)	58885 (406)
	-- --	64345 (444)	62424 (430)	63676 (439)	62666 (432)	58825 (406)
Yield Strength at 0.2% ϵ, psi (MN/m^2)	93544 (645)	-- --	-- --	-- --	-- --	-- --
	91465 (631)	-- --	-- --	-- --	-- --	-- --
Percent Elongation at Fracture	13.57	23.91	25.56	22.64	21.97	25.58
	15.00	23.19	24.44	22.22	22.56	25.38
Reduction in Area at Fracture (percent)	34.16	53.87	53.36	52.15	52.81	52.76
	34.62	55.81	53.95	53.88	53.25	52.20

(2.03 mm) further reduces the UTS by 9239 psi (64 MN/m^2) (9.3%). A comparison of the upper YS indicates that as the decarburization depth increases from no decarburization to 0.038 inches the YS decreases by 518 psi (4 MN/m^2) (0.8%), but increasing the decarburization depth from 0.038 inches to 0.080 inches results in a reduction in YS of 6722 psi (46 MN/m^2) (9.8%). At the lower YS the change from no decarburization to a 0.038 inch decarburized layer causes the YS to decrease 1755 psi (12 MN/m^2) (2.7%), and an increase from 0.038 inches decarburization to 0.080 inches results in an additional 4532 psi (31 MN/m^2) (7.2%) reduction in YS. These results indicate that the tensile properties are more greatly affected by the depth of decarburization than by the presence of an initial decarburized surface layer, a trend opposite to that found in the fatigue tests.

In comparing columns 2, 3, and 4, the only variable was the heat treatment times; none of the D-8 or D-24 specimens tested here had any surface decarburization. These results indicate (1) that the variation in heat treatment times did not affect the tensile properties of the core microstructure, and (2) that the removal of the decarburization restored the initial tensile properties.

An additional study was made using scanning electron microscopy (SEM) to ascertain if a variation in surface appearance resulted from the presence of surface decarburization. Following extensive examination, it was concluded that no distinction could be made between any of the twelve fracture surfaces (see Figure 17).

The important conclusion is, of course, that monotonic tensile loading does not indicate degradation of fatigue strength. Although there is some degradation in both the yield and tensile strengths with decarburization, the amount of degradation is insignificant until a large amount of decarburization is observed. The tensile fracture strains are unaffected. Assuming that decarburization observed in commercial practice would not exceed 0.020-0.025 inches or 0.61 mm-0.64 mm (more likely near 0.005-0.010 inches or 0.13-0.25 mm maximum), routine tensile testing for quality control would not reveal the presence of a decarburized layer, and, therefore, would not indicate the degraded fatigue life. At these decarburized depths, Rockwell hardness readings would also not indicate the presence of a decarburized layer.

Summary

A restatement of the fatigue and tensile data can best define the findings of the study thus far.

A comparison of the decarburized D-8 and D-24 ultimate tensile strengths (UTS) with the non-decarburized D-1 UTS indicates that the UTS decreases 4% from no decarburization to 0.038 inches (0.97 mm) decarburization and decreases 13% from no decarburization to 0.080 inches (2.03 mm) decarburization, while a comparison of the decarburized D-8

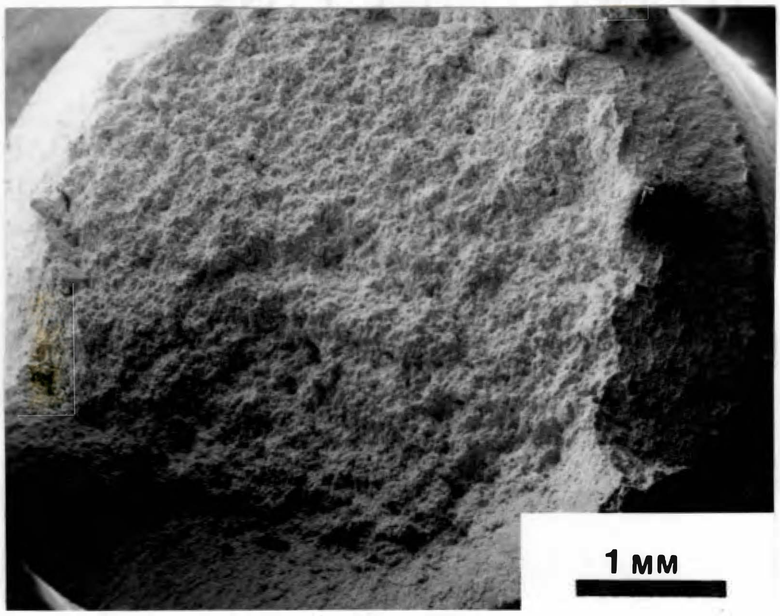

Figure 17. SEM Micrograph of a Fractured D-1 Tensile Test Specimen. 20x.

and D-24 yield strengths (YS) with the non-decarburized D-1 YS indicate that the YS decreases 2% from no decarburization to 0.038 inches decarburization and decreases 10% from no decarburization to 0.080 inches decarburization. However, delta percentage differences indicate that the endurance limit stress (Se) decreases 12% for the D-1 to D-8 curves and decreases 23% for the D-1 to D-24 curves. Delta percentage differences for the fatigue data indicate that the presence of 0.038-0.080 inches (0.97-2.03 mm) decarburization can reduce fatigue life as much as 100% at stress levels near the D-1 endurance limit stress (at 36500 psi or 252 MN/m^2).

The implication is that decarburization observed in production is normally less than 0.038 inches (generally 0.003-0.010 inches or 0.08-0.25 mm). Therefore, routine monotonic tensile testing would not indicate a degradation in fatigue life or fatigue strength; however, fatigue tests indicate a large decrease in fatigue life and fatigue strength initially and a less pronounced effect as the depth of decarburization is increased.

Finally, it cannot be emphasized enough that a clear statement of the method for comparing data must be reported; this is one of the reasons for some of the conflict in the conclusions reported in the past.

CHAPTER 5

FRACTOGRAPHY OF THE FATIGUE FAILED TEST SPECIMENS

Introduction

Technically important materials such as high strength aluminum alloys and steels exhibit fatigue strengths at 10^7 cycles well below the macroscopic yield strength of the alloys, and, as shown in Chapter 3, severe degradation in fatigue life is caused by surface decarburization (5, 50, 68).

The information furnished here is an attempt to provide a general overview of both the macroscopic and the microscopic fracture surface details which existed in this investigation. Although quantitative results are not so easily resolved as in Chapters 3 and 4, it is anticipated that the qualitative results can provide information regarding the trends and patterns which are exhibited by similar fatigue failures and eventually result in the expediency of future fractographic analysis.

Macroscopic Cracking Modes

Careful macroscopic examination of the fractured fatigue specimens revealed that three distinct fracture surface appearances exist in the applied stress range of a fatigue curve: (1) a "jagged" fracture surface at high stresses (above the YS), (2) a "ratcheted" surface appearance at medium stresses (approximately 1/2 of the UTS), and (3) a "smooth" fracture surface appearance at low stresses (approximately 1/2 of the YS) (see Figure 18). These three modes of fracture were observed in the D-1 series (see Figures 19, 20, and 21), in the D-8 series (see Figures 22, 23, and 24), and in the D-24 series (see Figures 25, 26, and 27). This phenomenon is most likely due to variations in the mode of macroscopic cracking, which is greatly affected by the applied stress. For example, the D-8 specimen in Figure 22 was tested at 85199 psi (587 MN/m^2) (85% of the D-8 UTS and 129% of the D-8 YS) and failed after 2600 cycles, or approximately 30 seconds; however, the D-8 specimen in Figure 24 was tested at an applied stress of 32730 psi (226 MN/m^2) (33% of the D-8 UTS and 50% of the D-8 YS) and ran for approximately 4.23×10^6 cycles, or 7.3 hours before failing.

At high stress levels the first crack which initiates will most likely result in the fracture of the specimen, due to the short initiation stage and high crack propagation rate. The result is a highly irregular, or "jagged," surface appearance (see Figure 18). The term "jagged" refers to the large variation in the maximum and minimum points of the fracture surface if measured from an arbitrary datum line drawn circumferentially about the specimen's longitudinal axis. Although the fracture surface may appear, at first, to be "ratcheted" (see Figure 19), there are few actual ratchet marks when compared to specimens which fracture at medium stress levels (see Figures 22 and 23). At medium stress levels multiple

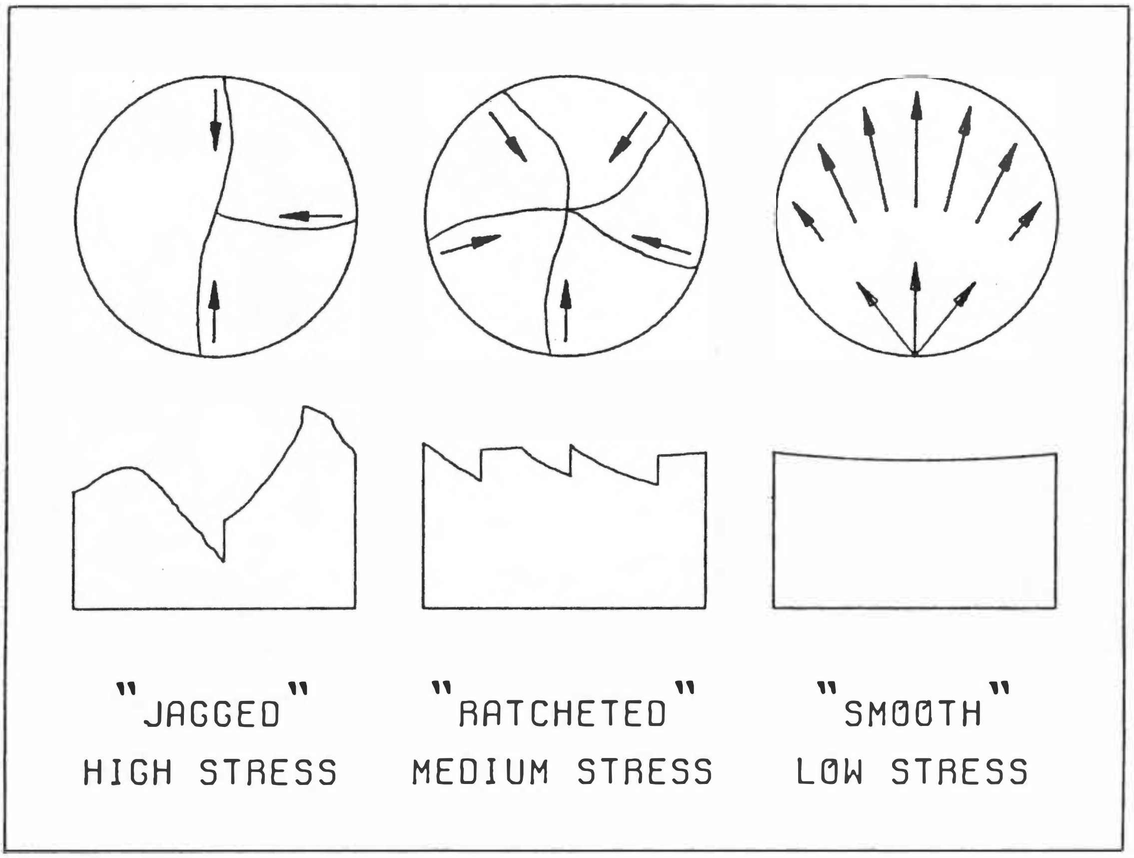

Figure 18. Proposed Modes of Macroscopic Crack Propagation.

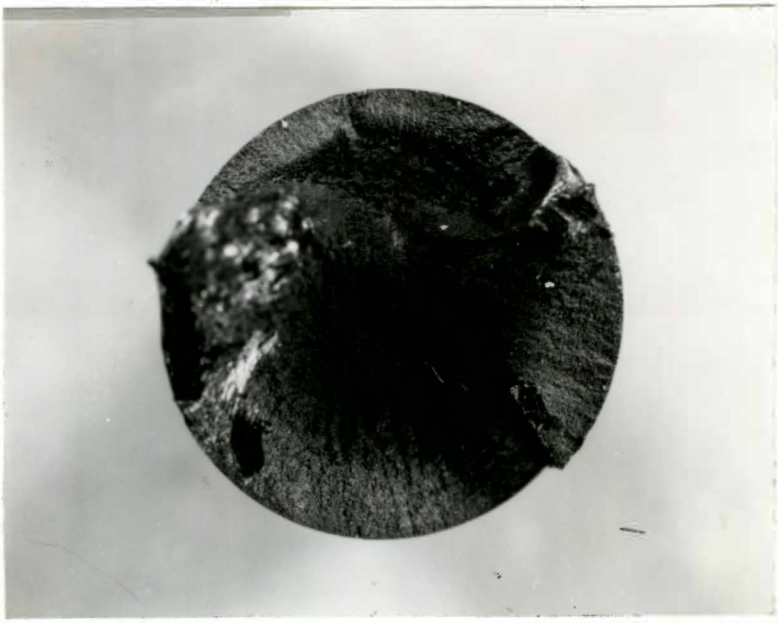

Figure 19. Photomacrograph of a D-1 Fracture Surface. Specimen Failed after 6800 Cycles; Applied Stress, 71004 psi (490 MN/m^2) (106% of the YS). 8x.

Figure 20. Photomacrograph of a D-1 Fracture Surface. Specimen Failed after 24700 Cycles; Applied Stress, 56211 psi (388 MN/m^2) (84% of the YS). 8x.

Figure 21. Photomacrograph of a D-1 Fracture Surface. Specimen Failed after 3.34×10^5 Cycles; Applied Stress, 44821 psi (309 MN/m^2) (67% of the YS). 8x.

Figure 22. Photomacrograph of a D-8 Fracture Surface. Specimen Failed after 2600 Cycles; Applied Stress, 85199 psi (587 MN/m^2) (129% of the YS). 8x.

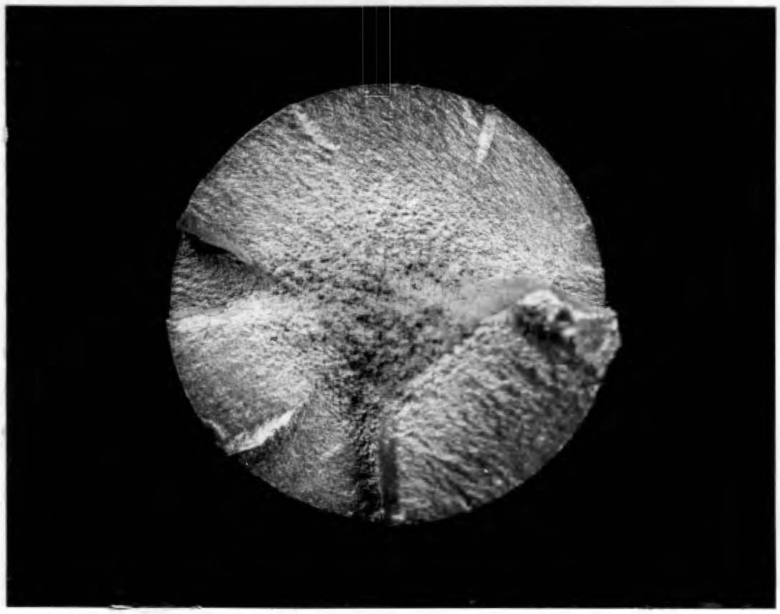

Figure 23. Photomacrograph of a D-8 Fracture Surface. Specimen Failed after 33300 Cycles; Applied Stress, 49199 psi (339 MN/m^2) (74% of the YS). 8x.

Figure 24. Photomacrograph of a D-8 Fracture Surface. Specimen Failed after 4.32 x 10^6 Cycles; Applied Stress, 32730 psi (226 MN/m^2) (50% of the YS). 8x.

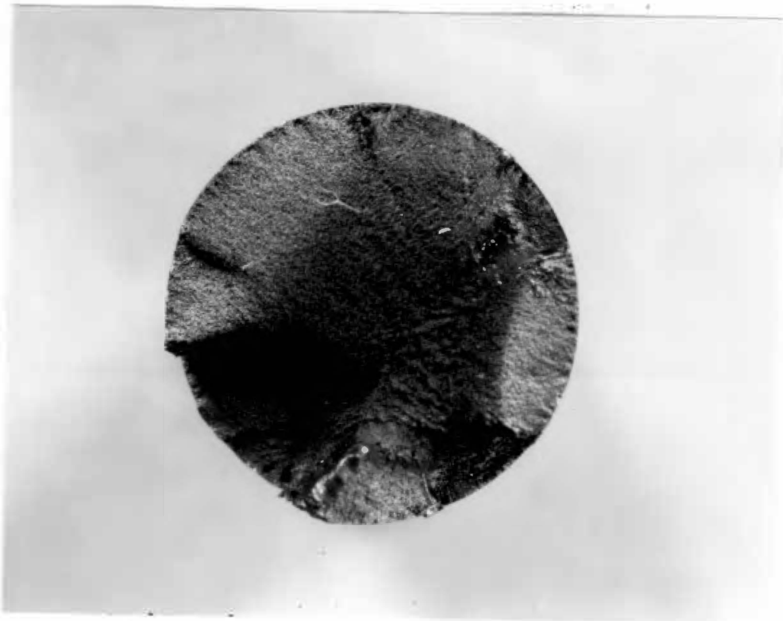

Figure 25. Photomacrograph of a D-24 Fracture Surface. Specimen Failed after 4300 Cycles; Applied Stress, 69232 psi (477 MN/m^2) (115% of the YS). 8x.

Figure 26. Photomacrograph of a D-24 Fracture Surface. Specimen Failed after 14200 Cycles; Applied Stress, 54995 psi (379 MN/m^2) (91% of the YS). 8x.

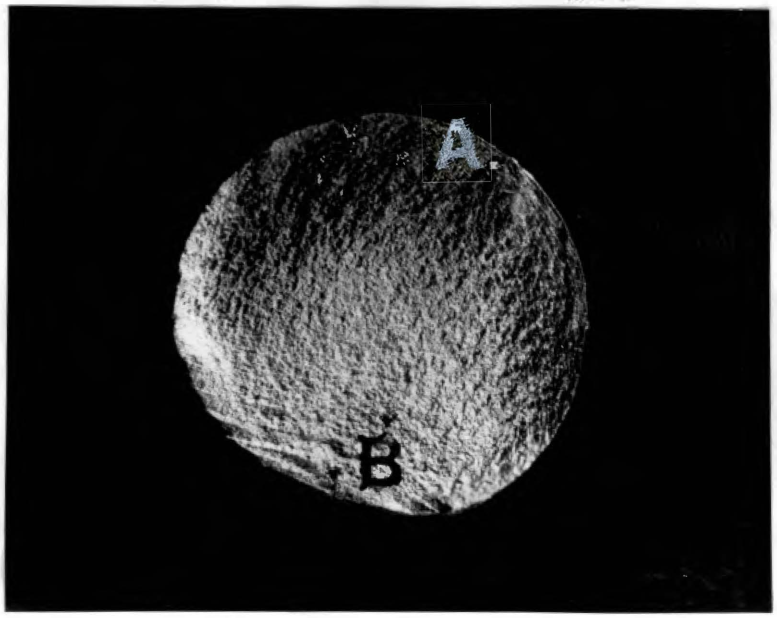

Figure 27. Photomacrograph of a D-24 Fracture Surface. Specimen Failed after 1.76×10^6 Cycles; Applied Stress, 31346 psi (216 MN/m^2) (52% of the YS). Crack Initiated at Point A and Terminated at Point B. 8x.

cracks may initiate due to the increased initiation stage time, and fracture may result from several crack propagations with a "ratcheted" surface appearance being exhibited (see Figure 18). For stress levels which are near the endurance limit, the time required to complete a fatigue test may range from several hours to several days, depending on the applied stress, and, as noted by previous authors, cracks at these stresses have lengthy initiation stages and very low propagation rates (21, 30, 38, 51). In general, only one or two points of crack initiation are observed (see Figure 27). In Figure 27 the crack initiated at point A and propagated to point B. The crack tends to fan out to the right and to the left of the initiation site, the result being a "smooth" fracture surface (see Figure 18, page 59).

Microscopic Surface Details

Although the primary concern of the scanning electron microscopy (SEM) was striation morphology, its implementation enabled regions of ductile fracture to be defined, and the use of x-ray analysis provided a qualitative look at inclusion composition. The micrographs discussed here are categorized in the following series: D-1, D-8, and D-24. Each series is presented in order of decreasing stress, each micrograph listing the applied stress, the number of cycles to failure, and the region in which the particular feature appeared.

Figures 28 and 29 show a D-1 specimen which was tested at an applied

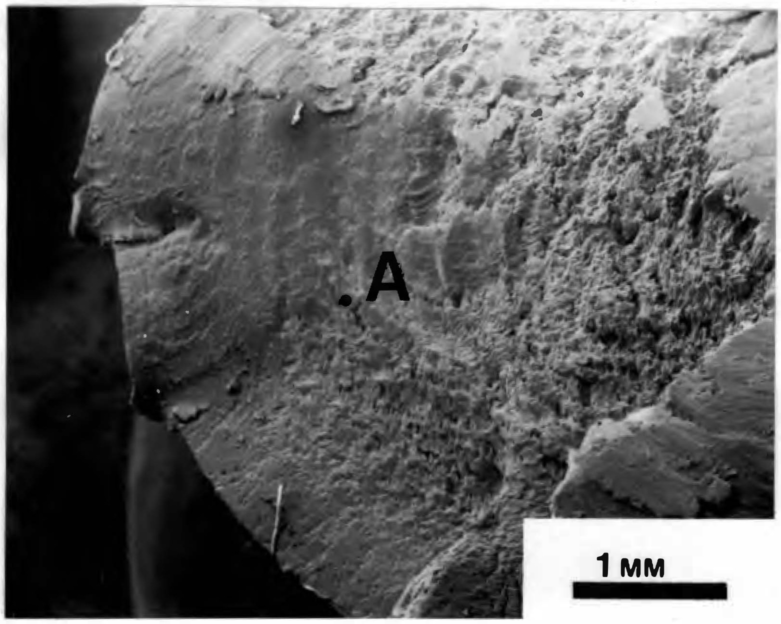

Figure 28. SEM Micrograph of a D-1 Fracture Surface. Specimen Failed after 3100 Cycles; Applied Stress, 82996 psi (572 MN/m^2) (123% of the YS). Point A is 0.06 Inches (1.5 mm) from Edge of Fracture Surface. 20x.

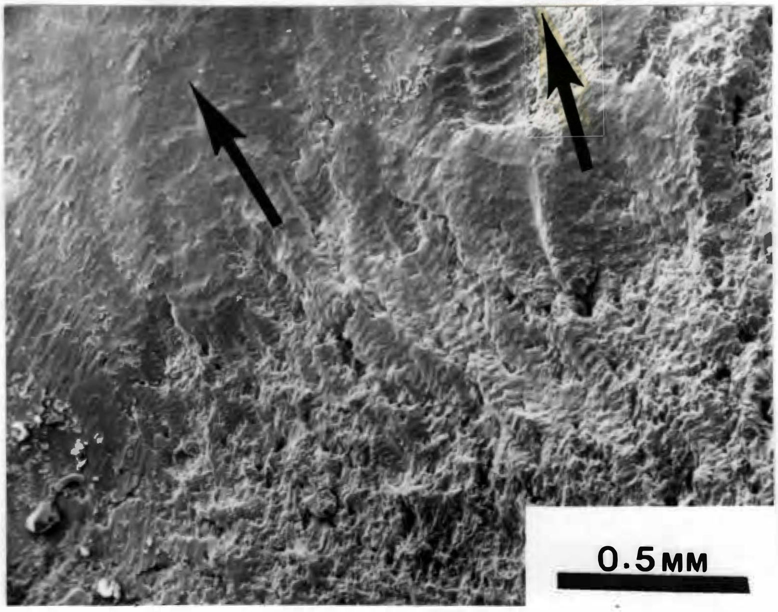

Figure 29. SEM Micrograph of Striations Present at Point A in Figure 28. Arrows Show Microscopic Crack Propagation Directions. 50x.

stress of 82996 psi (572 MN/m^2) (80% of the D-1 UTS and 123% of the D-1 YS). At this stress the crack propagation rates are extremely high, resulting in the striations being visible at unusually low magnifications, 20x and 50x. In Figure 30 the applied stress has been reduced to 56211 psi (388 MN/m^2) (54% of the D-1 UTS and 84% of the D-1 YS), and a ratcheted fracture surface is observed. Figure 31 shows a region at the center of Figure 30, particularly point B. In this region numerous inclusions are evident in the form of spheres and elipsoids. Subsequent x-ray analysis revealed the composition of these and most other inclusions to be manganese sulfide (MnS). Figure 32 shows a D-1 specimen which was tested at 53253 psi (367 MN/m^2) (51% of the D-1 UTS and 79% of the D-1 YS). Point C, which is shown in Figure 33, is approximately 0.02 inches (0.5 mm) from the edge of the fracture surface. The mutually parallel striations exhibited in Figure 33 were rarely observed. The spacing of these striations is approximately 6.3×10^{-5} inches (0.2 microns). Figures 34 and 35 show a specimen which was tested at 50299 psi (347 MN/m^2) (49% of the D-1 UTS and 75% of the D-1 YS). In Figure 35A one can determine, by visual examination, the striations which exist at point D in Figure 34; however, a much higher magnification (see Figure 35B) is required in order to determine the striation spacing, approximately 6.6×10^{-5} inches (0.2 microns). It should be mentioned that, in general, striations were not visible below 450x, although there are some exceptions (see Figures 28 and 29).

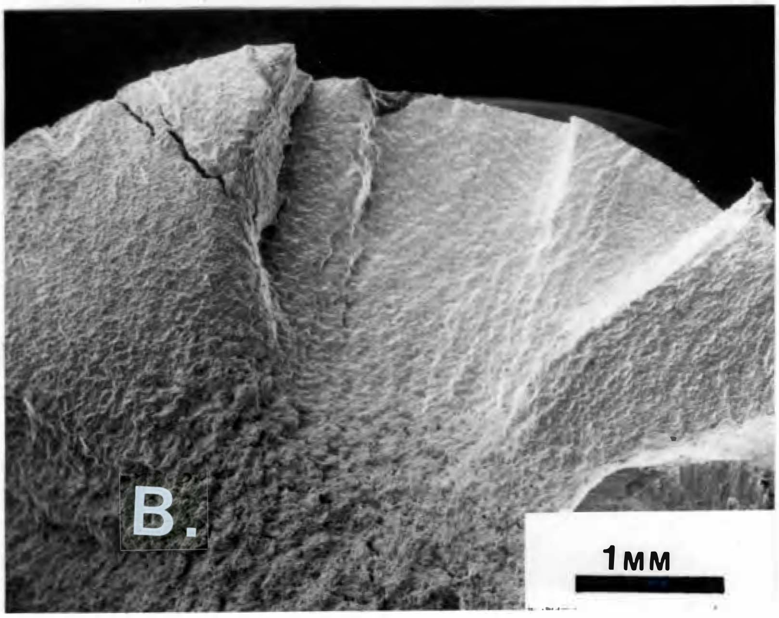

Figure 30. SEM Micrograph of a D-1 Fracture Surface. Specimen Failed after 27200 Cycles; Applied Stress, 56211 psi (388 MN/m^2) (84% of the YS). Point B is 0.11 Inches (2.8 mm) from Edge of Fracture Surface. 20x.

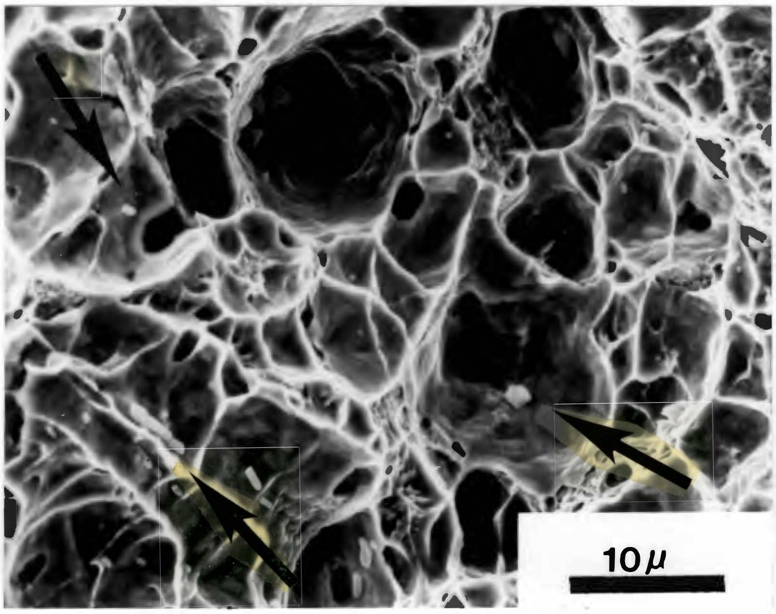

Figure 31. SEM Micrograph of Ductile Fracture at Point B in Figure 30; Note Numerous Inclusions (See Arrows). 2000x.

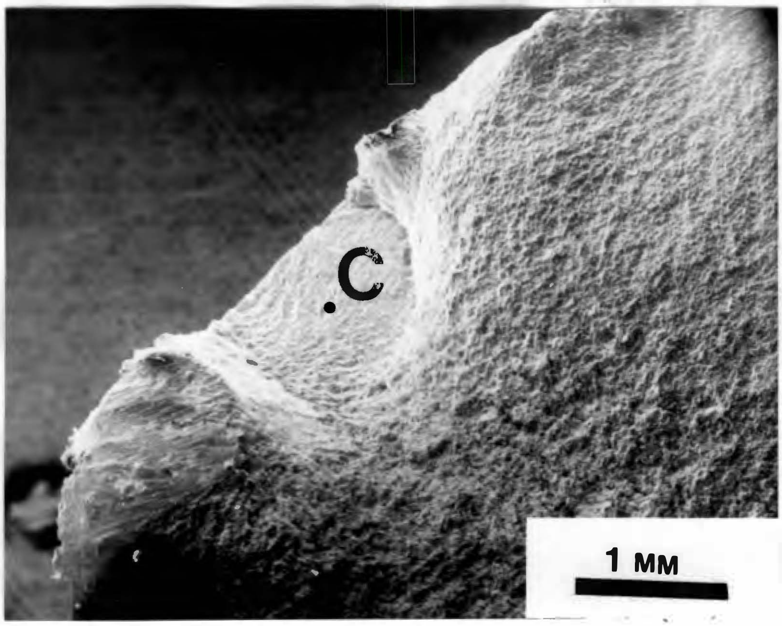

Figure 32. SEM Micrograph of a D-1 Fracture Surface. Specimen Failed after 41200 Cycles; Applied Stress, 53253 psi (367 MN/m^2) (79% of the YS). Point C is 0.02 Inches (0.5 mm) from Edge of Fracture Surface. 20x.

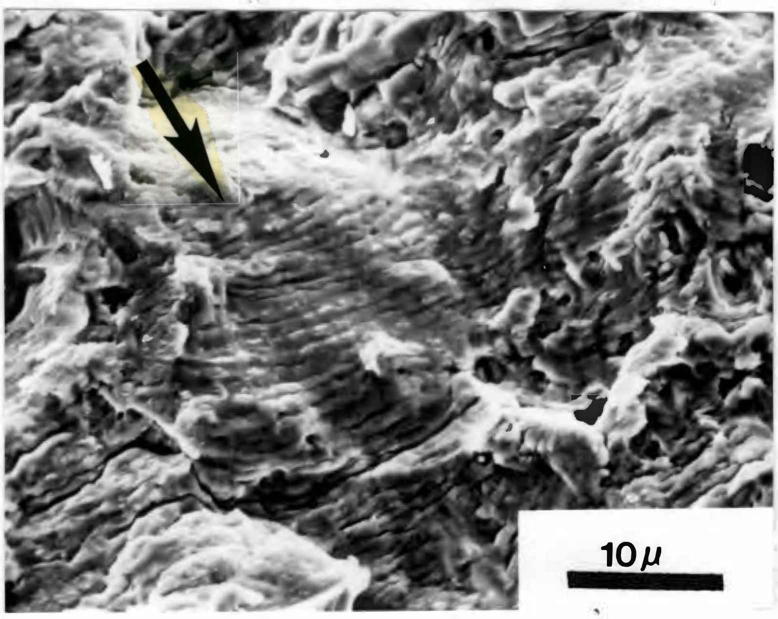

Figure 33. SEM Micrograph Showing Striations and Secondary Cracking at Point C in Figure 32. Arrow Indicates Macroscopic Crack Propagation Direction. 2000x.

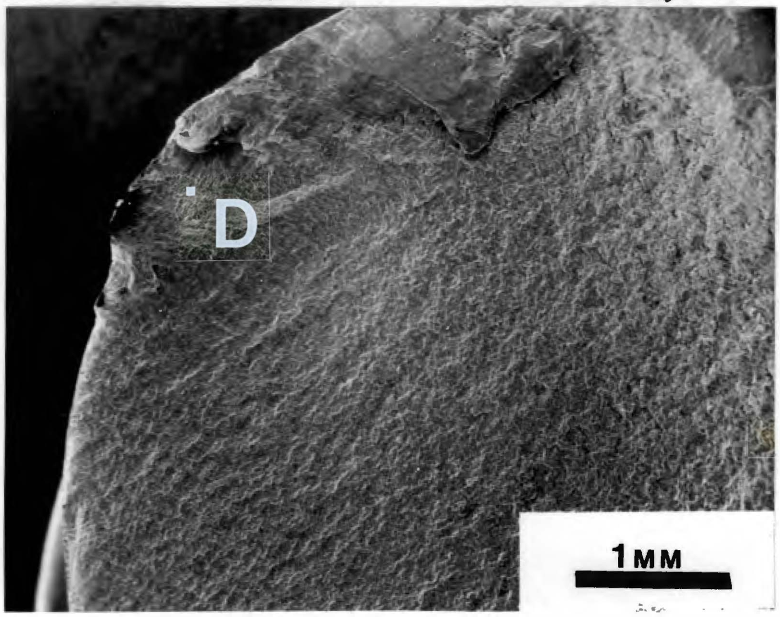

Figure 34. SEM Micrograph of a D-1 Fracture Surface. Specimen Failed after 69300 Cycles; Applied Stress, 50299 psi (347 MN/m^2) (75% of the YS). Point D is 0.01 Inches (0.3 mm) from the Edge of Fracture Surface. 19x.

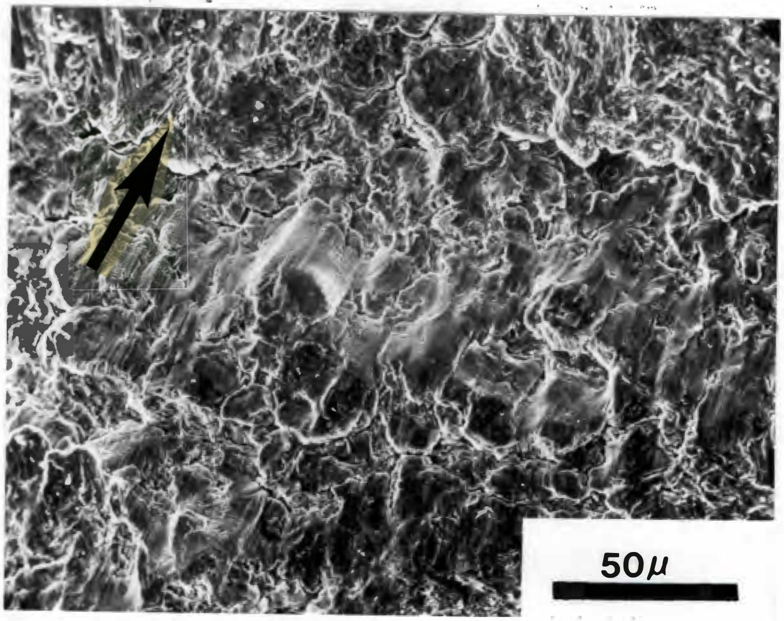

A. 475x.

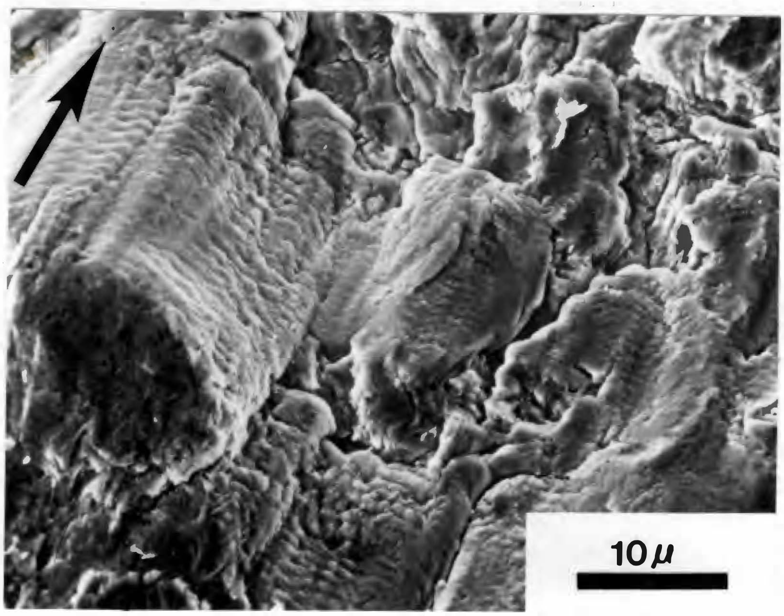

B. 1900x.

Figure 35. SEM Micrographs Showing Striations Present at Point D in Figure 34. Arrows Indicate Macroscopic Crack Propagation Direction.

Figure 36 is a micrograph of a D-8 specimen which was tested at a stress of 66203 psi (456 MN/m^2) (66% of the D-8 UTS and 100% of the D-8 YS). The striation pattern shown here, termed "quasi-striation" because of its unequal spacing, was the type of striation characteristic most commonly observed in the study. This particular set of striations was 0.04 inches (1.0 mm) from the edge of the fracture surface or 0.002 inches (5.08 microns) inward from the case/core juncture. In previous micrographs one could approximate the crack propagation rates by measuring the striation spacing; however, because the quasi-striation pattern spacing is not constant, an approximation of the crack propagation rate is virtually impossible. Figure 37 is a micrograph of a D-8 specimen which was tested 48951 psi (337 MN/m^2) (49% of the D-8 UTS and 74% of the D-8 YS). The micrograph clearly depicts the ratcheted surface appearance which occurs at medium stress levels. Point A is located approximately 0.02 inches (0.5 mm) from the edge of the fracture surface, or approximately midway in the decarburized surface layer. Figure 38 shows a series of increasing magnifications of the striations observed at point A. In Figure 38A the striations are barely visible, but at 2000x in Figure 38B they are easily recognized. In Figure 38C note, again, the difference in the spacings at the lower left and near the center of the micrograph. The spacing at the center of Figure 38D is approximately 6.0×10^{-5} inches (0.2 microns).

In Figure 39 the applied stress has decreased to 43535 psi (300 MN/m^2)

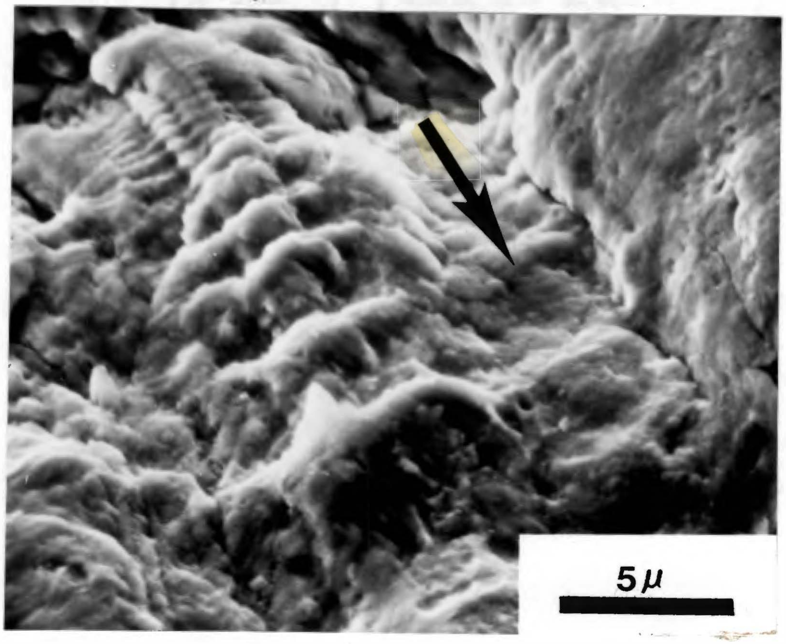

Figure 36. SEM Micrograph Showing "Quasi-Striations" Observed at a Point 0.04 Inches (1.0 mm) from the Edge of a D-8 Fracture Surface. Specimen Failed after 8300 Cycles; Applied Stress, 66203 psi (456 MN/m^2) (the YS). Arrow Indicates Microscopic Crack Propagation Direction. 4500x.

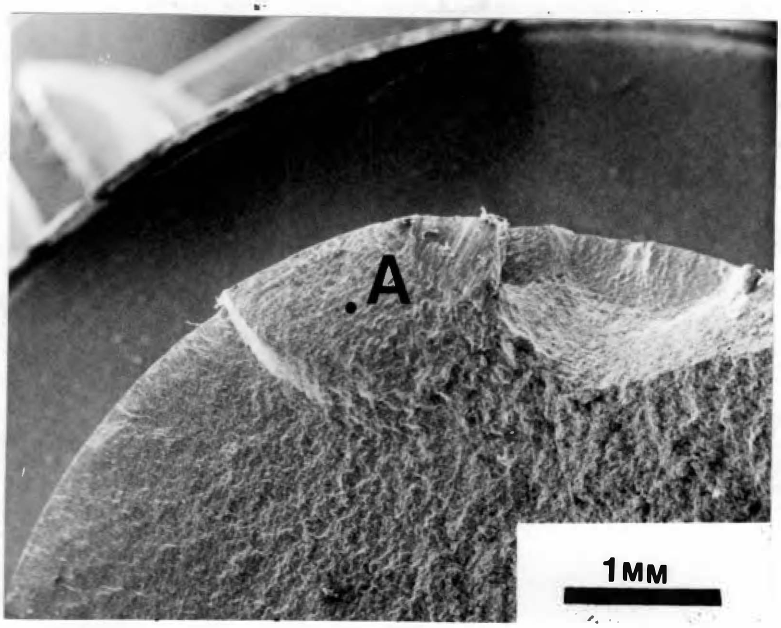

Figure 37. SEM Micrograph of a D-8 Fracture Surface. Specimen Failed after 35900 Cycles; Applied Stress, 48951 psi (337 MN/m^2) (74% of the YS). Point A is 0.02 Inches (0.5 mm) from Edge of Fracture Surface. 20x.

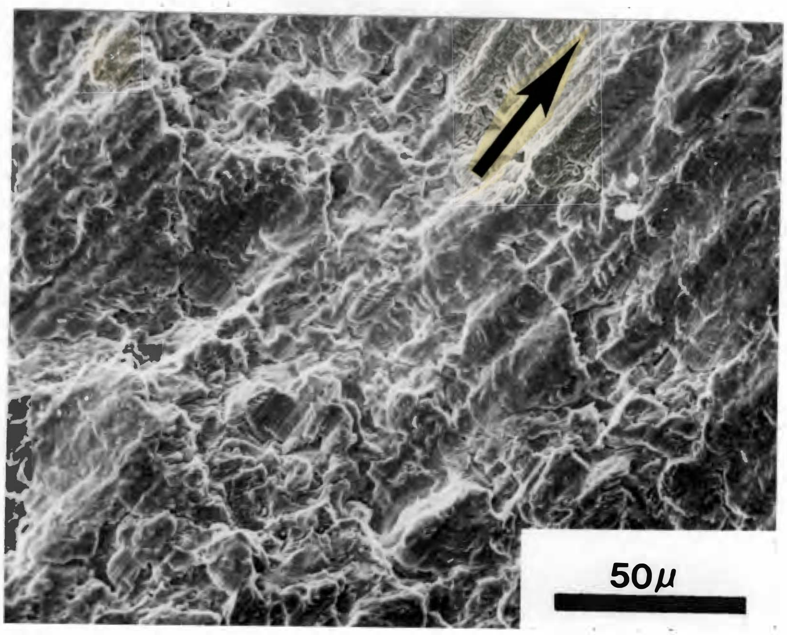

A. 500x.

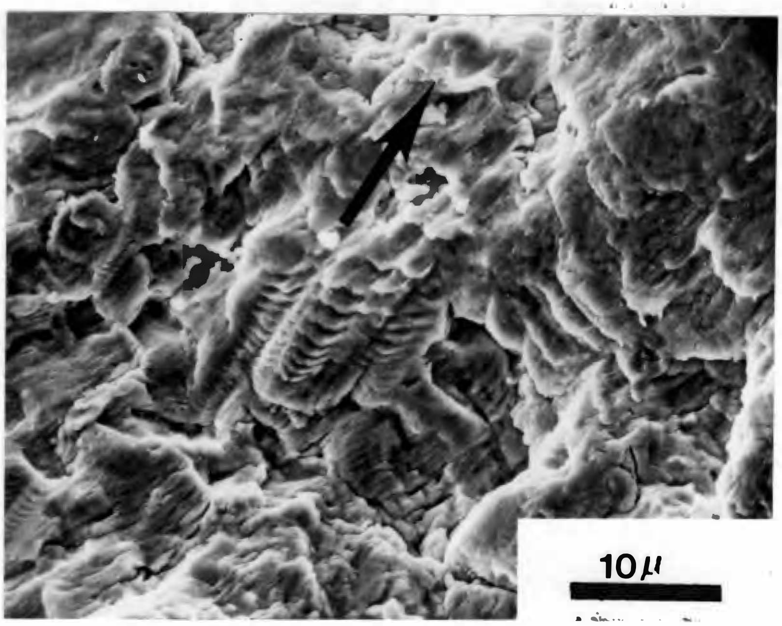

B. 2000x.

Figure 38. SEM Micrographs of Striations Present at Point A in Figure 37. Arrows Show Microscopic Crack Propagation Direction.

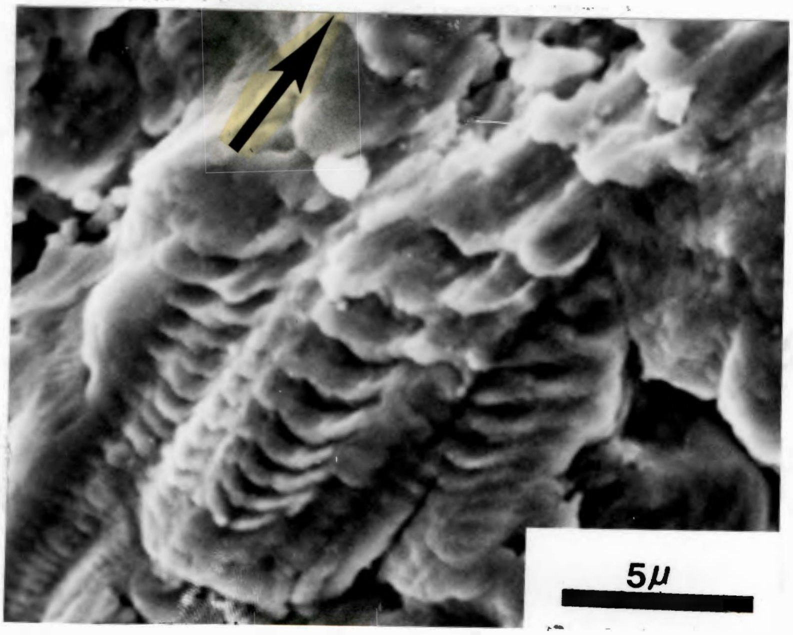

C. 5000x.

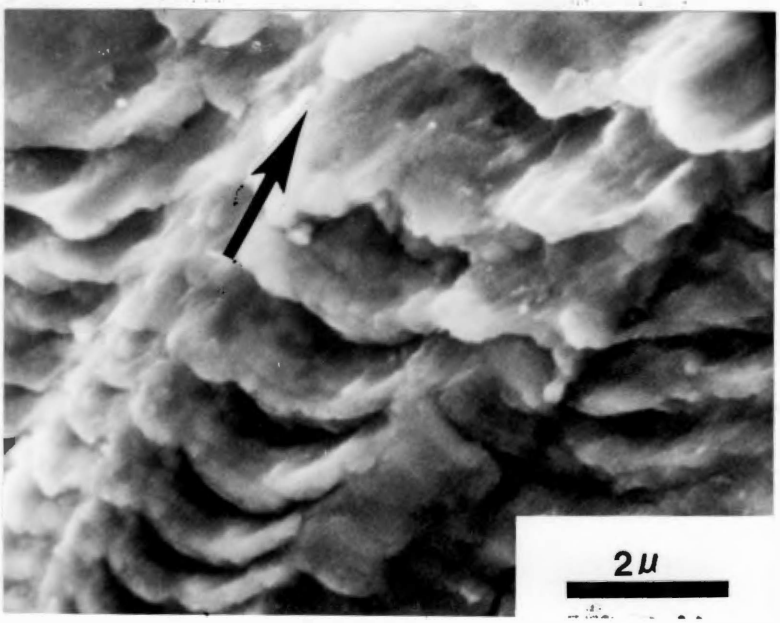

D. 10000x.

Figure 38. (Continued).

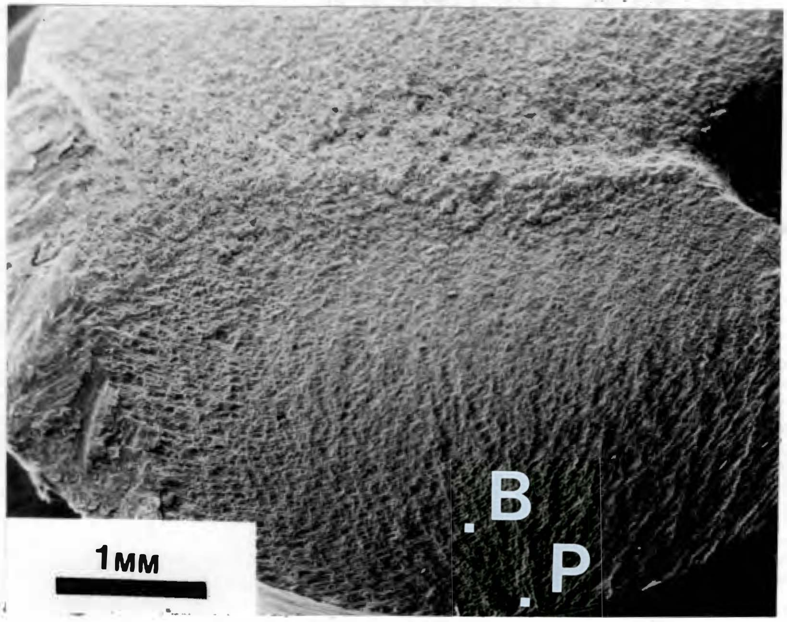

Figure 39. SEM Micrograph Showing the Crack Initiation Site (Point P). The D-8 Specimen Failed after 1.17 x 10^5 Cycles; Applied Stress, 43535 psi (300 MN/m^2) (66% of the YS). Point B is 0.02 Inches (0.5 mm) from Edge of Fracture Surface. 20x.

(44% of the D-8 UTS and 66% of the D-8 YS), and the fracture surface has changed from the ratcheted appearance to the smooth appearance with the point of crack initiation visible at point P, near the bottom of the micrograph. Figure 40 shows striations which appear at point B in Figure 39. Although the macroscopic crack propagation direction appears to proceed vertically (see Figure 39), the microscopic crack propagation direction is toward the left of the micrograph, several tens of degrees off the macroscopic crack propagation direction. Figure 40C shows the striation spacing increasing from 2.0×10^{-5} inches (0.05 microns) to 1.4×10^{-4} inches (0.4 microns) (an increase of 600%) over a distance of approximately 7.0×10^{-4} inches (1.8 microns).

Care must be taken not to confuse pearlite in a fracture surface of steel with striations. A typical pearlite colony is shown in Figure 41. The pearlite spacing of the colony exhibited in Figure 41 is approximately 1.0×10^{-5} inches (0.~~0~~3 microns).

The remaining micrographs are from the D-24 series of test specimens; for these particular specimens the depth of decarburization is 0.080 inches (2.03 mm). Figure 42 shows a specimen which was tested at 69232 psi (477 MN/m^2) (77% of the D-24 UTS and 115% of the D-24 YS). Since point A is only 0.02 inches (0.5 mm) from the edge of the fracture surface, the striations shown in Figure 43 are in the primary ferrite. These striations are very well defined, and the spacing is essentially constant. The striation spacing at the center of Figure 43C is approximately 1.1×10^{-4} inches

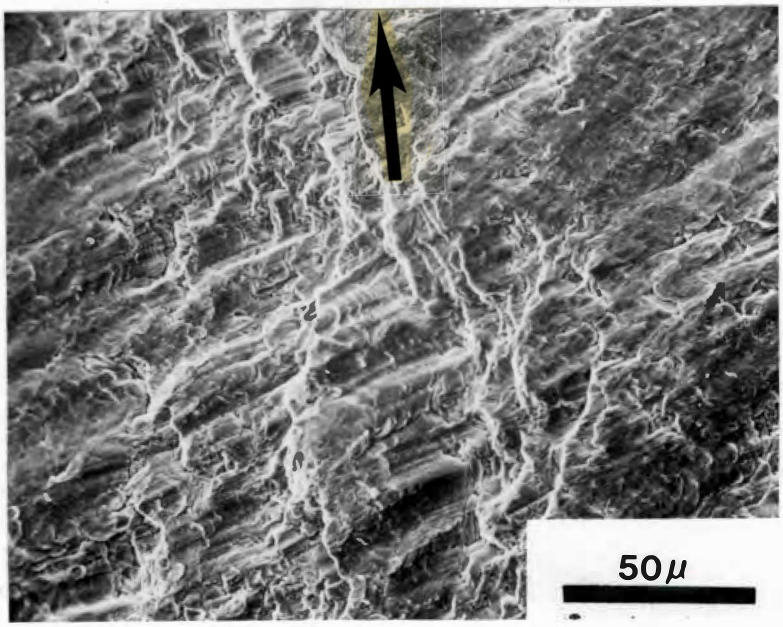

A. 500x.

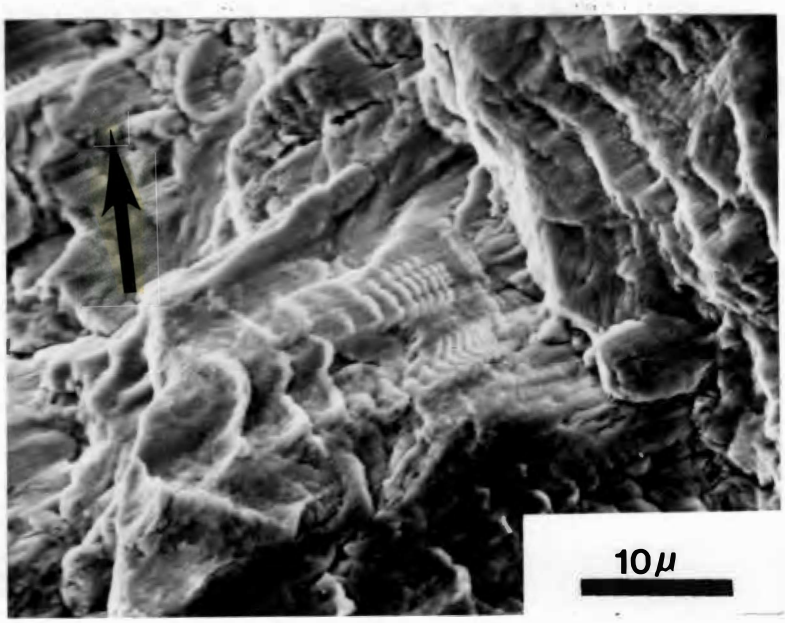

B. 2000x.

Figure 40. SEM Micrographs of Striations Present at Point B in Figure 39. Arrows Show Macroscopic Crack Propagation Direction.

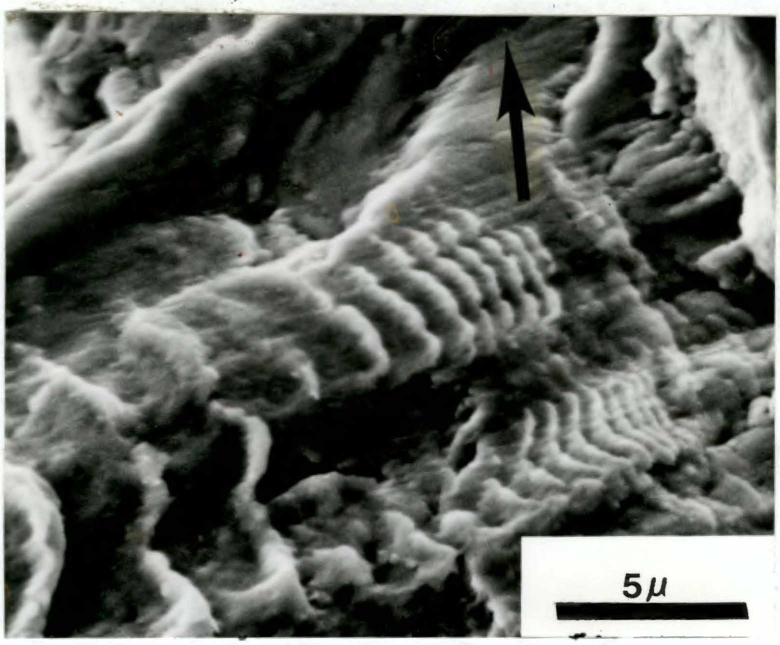

C. 5000x.

Figure 40. (Continued).

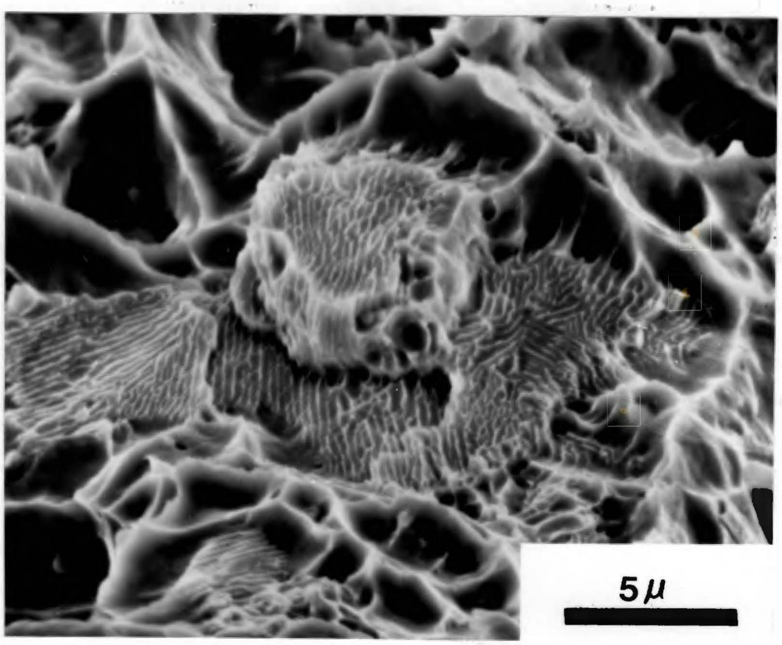

Figure 41. SEM Micrograph of Pearlite Observed at the Center of a D-8 Fracture Surface in a Region of Ductile Fracture. Specimen Failed after 1.65 x 10^6 Cycles; Applied Stress, 35448 psi (244 MN/m^2) (54% of the YS). 4500x.

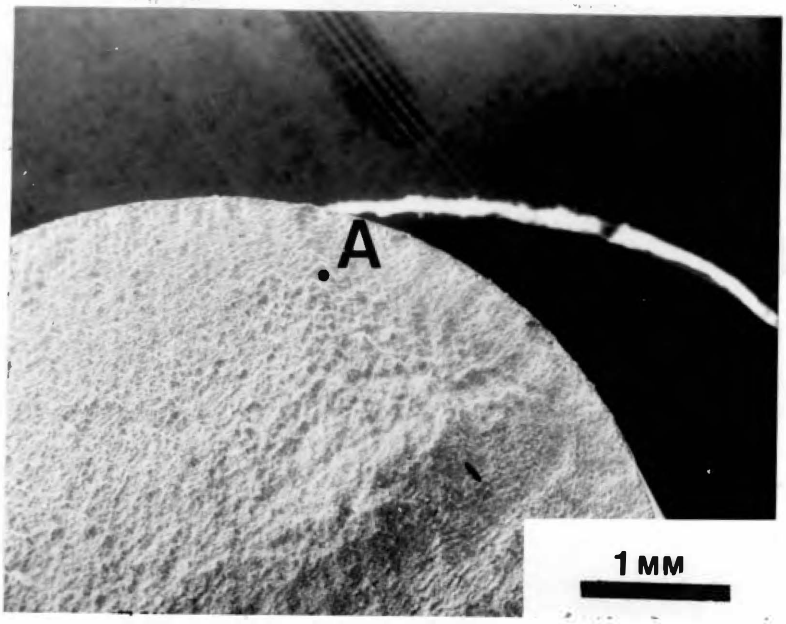

Figure 42. SEM Micrograph of a D-24 Fracture Surface. Specimen Failed after 4300 Cycles; Applied Stress, 69232 psi (477 MN/m^2) (115% of the YS). Point A is 0.02 Inches (0.5 mm) from Edge of Fracture Surface. 20x.

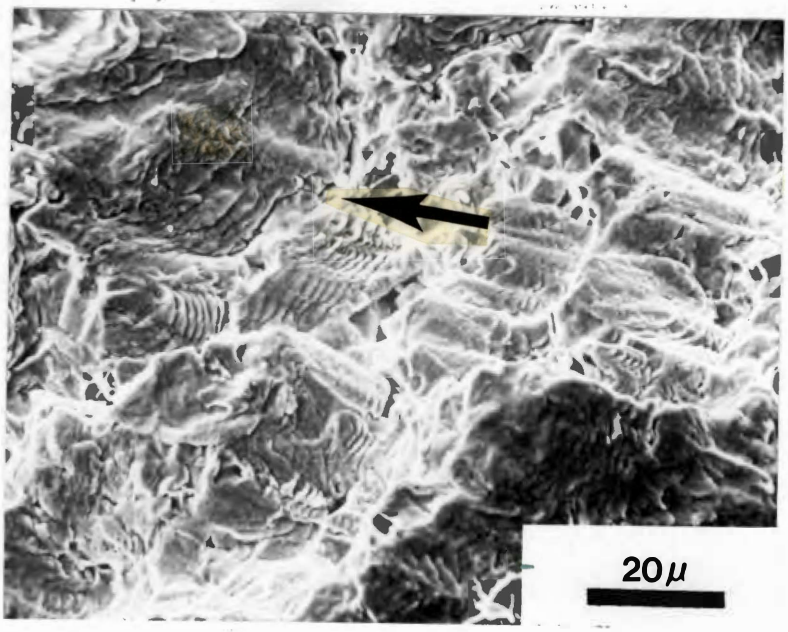

A. 900x.

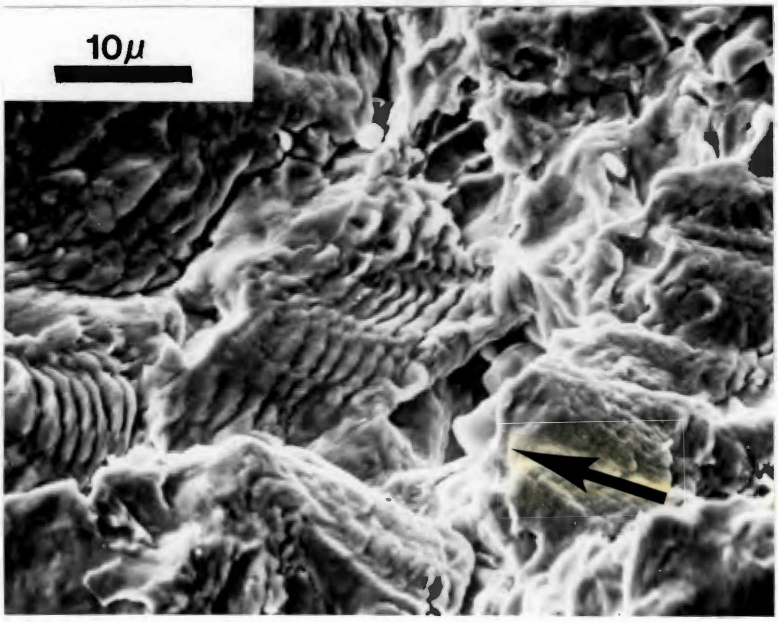

B. 1800x.

Figure 43. SEM Micrographs Showing Striations Present at Point A in Figure 42. Arrows Indicate Microscopic Crack Propagation Direction.

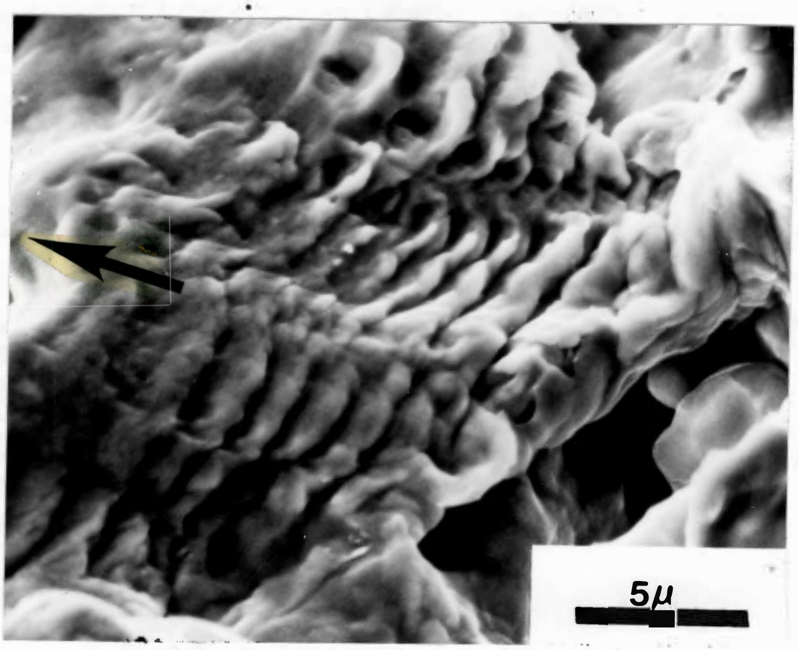

C. 4500x.

Figure 43. (Continued).

(0.3 microns). Figure 44 shows, again, the ratcheting effect which occurs at medium stress levels, and Figure 45 exhibits the striations which appear at point B in Figure 44. The striations are visible at 450x; however, one finds the unequal spacing to be the predominant fatigue pattern.

The D-24 specimen in Figure 46 was tested at a stress of 40493 psi (279 MN/m^2) (45% of the D-24 UTS and 67% of the D-24 YS). Here, the surface appears smooth, and the crack initiation site can be seen at point P. Figure 47 shows a fatigue pattern, frequently called a "tire track," which existed at point C in Figure 46. Note that point C is 0.08 inches (2.0 mm) from the edge of the fracture surface, directly at the case/core juncture. The surface in Figure 47 appears rubbed, and the upper row of the striations appears to have been pierced. This characteristic resulted from the continued piercing of the fracture surface by a protrusion from the mating fracture surface as the crack closed, during the compressive stress portion of each load cycle (10, 12, 46). Figure 47B depicts the increased spacing which results as the fracture stress increases, and Figures 47C and 47D show higher magnifications of the initiation of the tire tracks. The spacing of the tire tracks in Figure 47D ranges from 4.0×10^{-5} inches (0.1 microns) to 2.0×10^{-4} inches (0.5 microns).

Figures 48A and 48B are micrographs of striations which were observed in the core microstructure of a fatigue specimen at a point 0.10 inches (2.5 mm) from the edge of the fracture surface. The applied stress

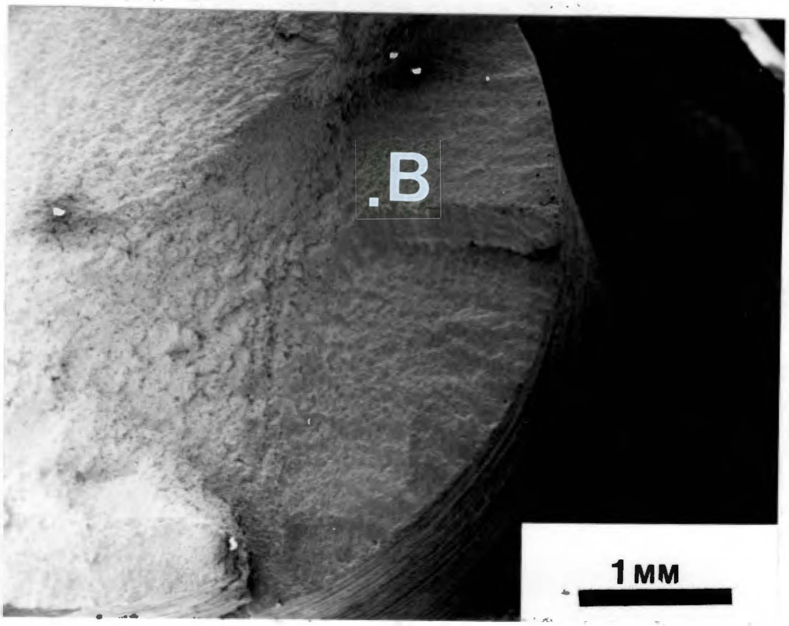

Figure 44. SEM Micrograph Showing a "Ratcheted" Fracture Surface. The D-24 Specimen Failed after 11900 Cycles; Applied Stress, 52065 psi (359 MN/m^2) (86% of the YS). Point B is 0.05 Inches (1.3 mm) from Edge of Fracture Surface. 19x.

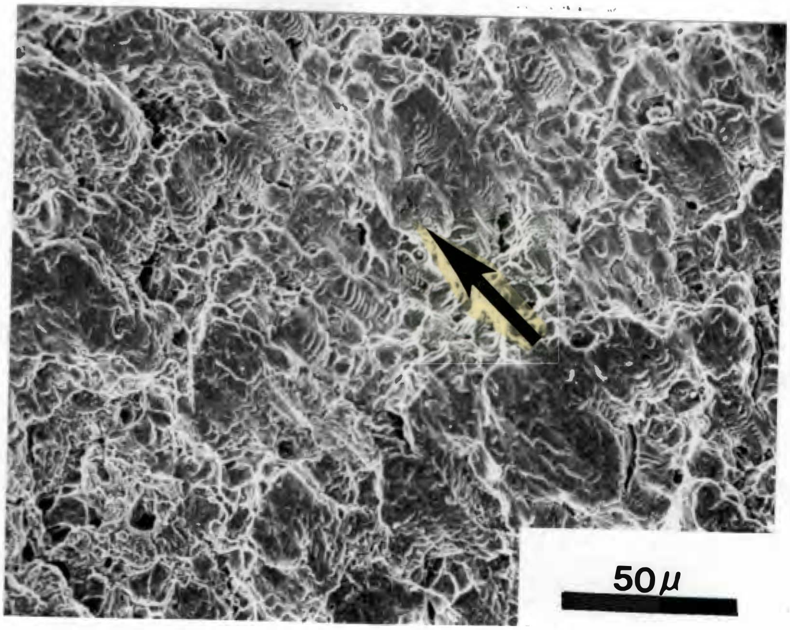

A. 450x.

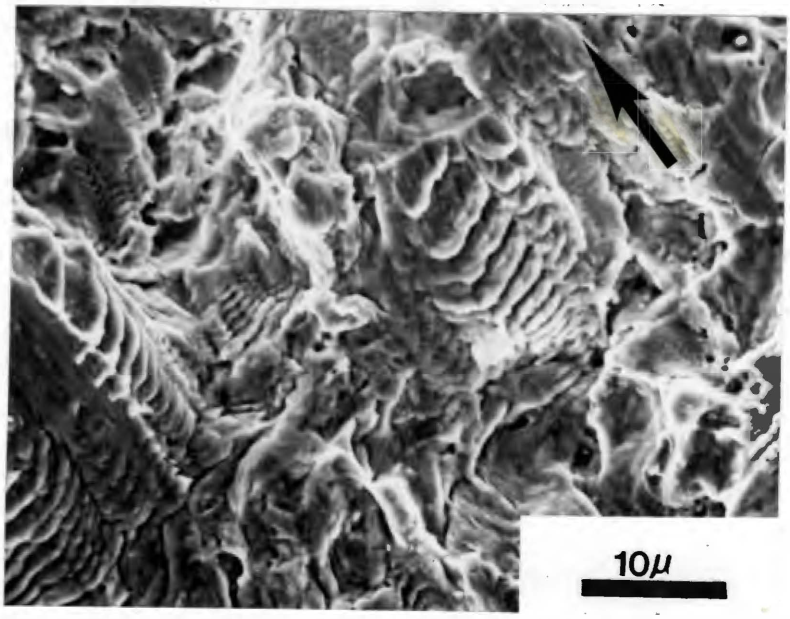

B. 1800x.

Figure 45. SEM Micrographs of Striations Present at Point B in Figure 44. Arrows Show Microscopic Crack Propagation Direction.

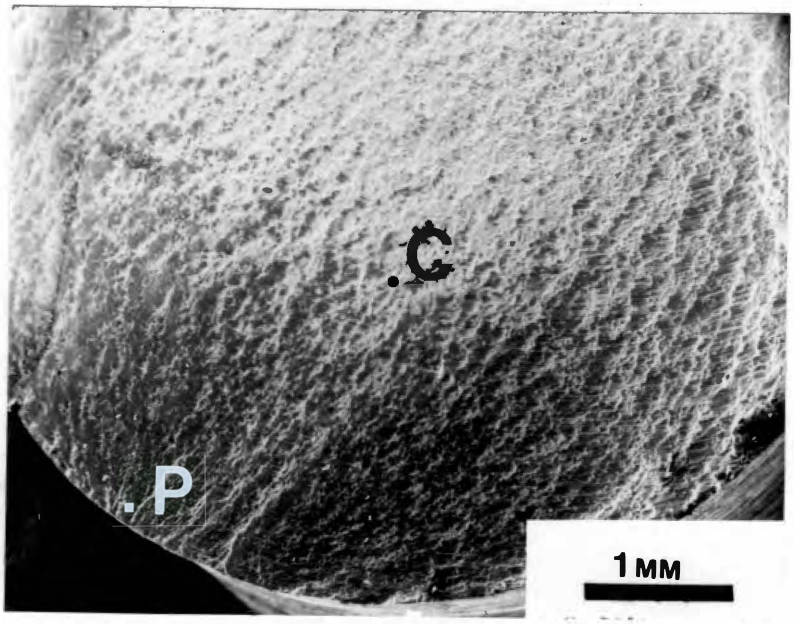

Figure 46. SEM Micrograph of a D-24 Fracture Surface. Specimen Failed after 1.52×10^5 Cycles; Applied Stress, 40493 psi (279 MN/m^2) (67% of the YS). Point C is 0.08 Inches (2.0 mm) (the Decarburized Depth) from Edge of Fracture Surface. Point P Shows the Crack Initiation Site. 20x.

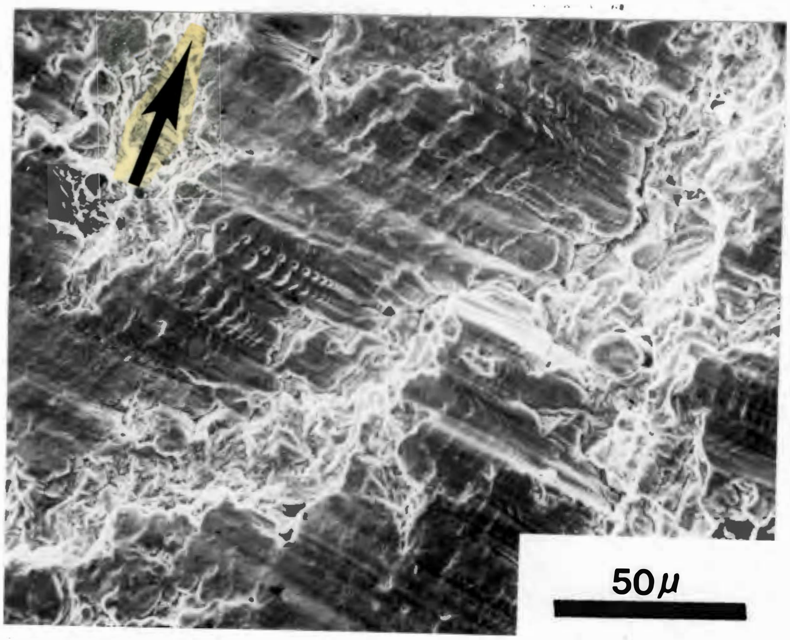

A. 500x.

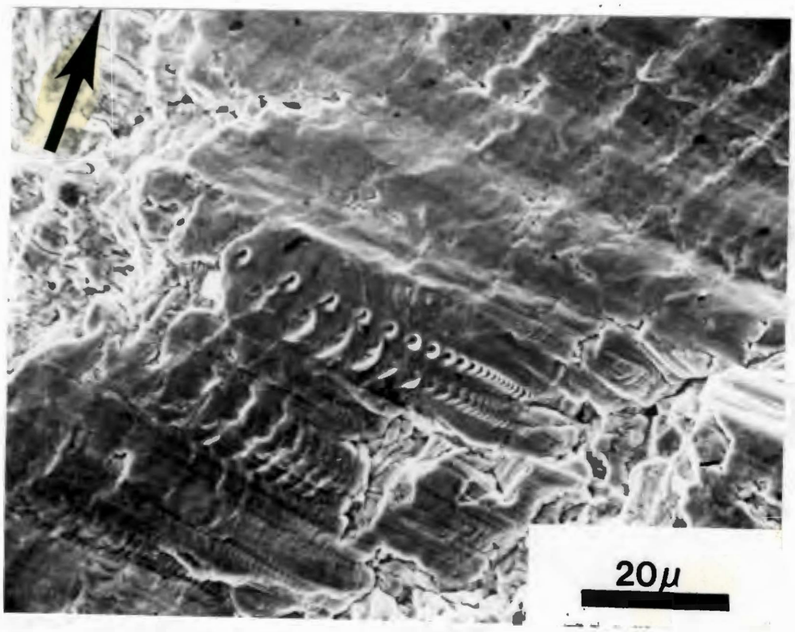

B. 1000x.

Figure 47. SEM Micrographs Showing Striations Present at Point C in Figure 46. Arrows Indicate Macroscopic Crack Propagation Direction.

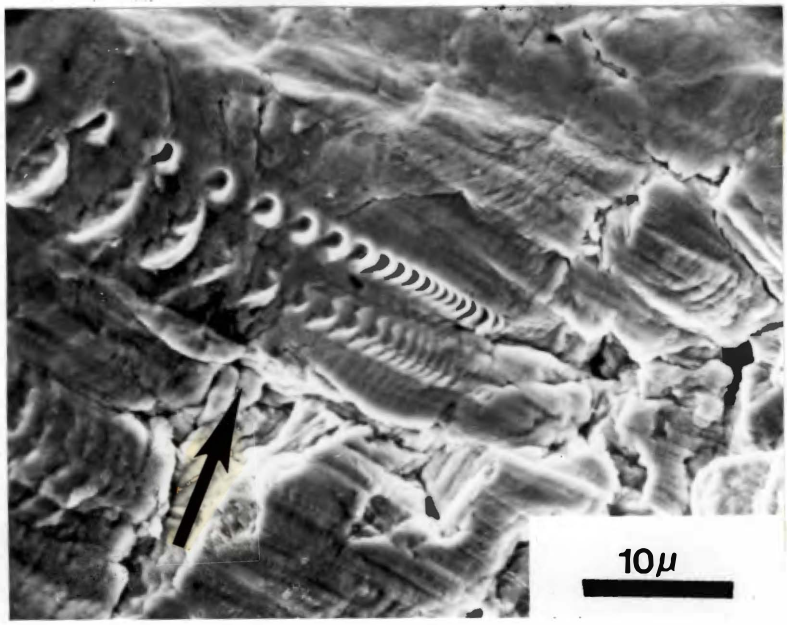

C. 2000x.

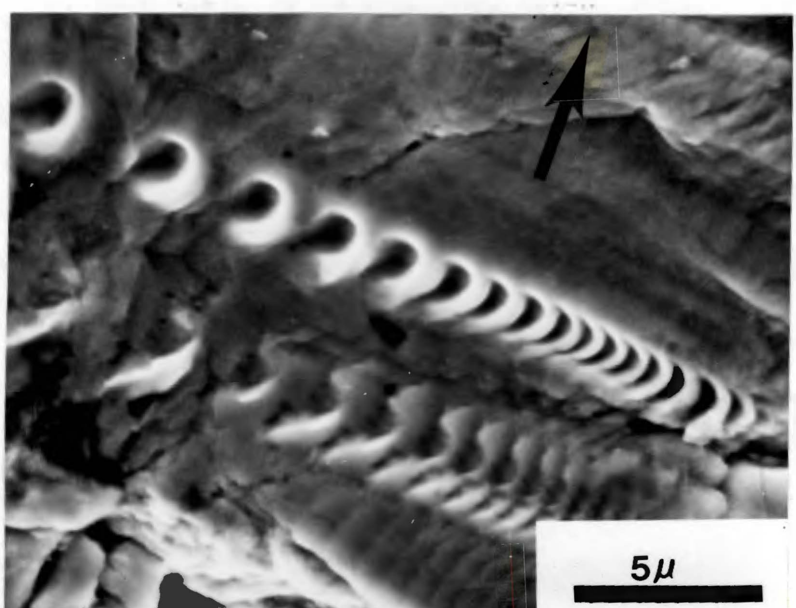

D. 5000x.

Figure 47. (Continued).

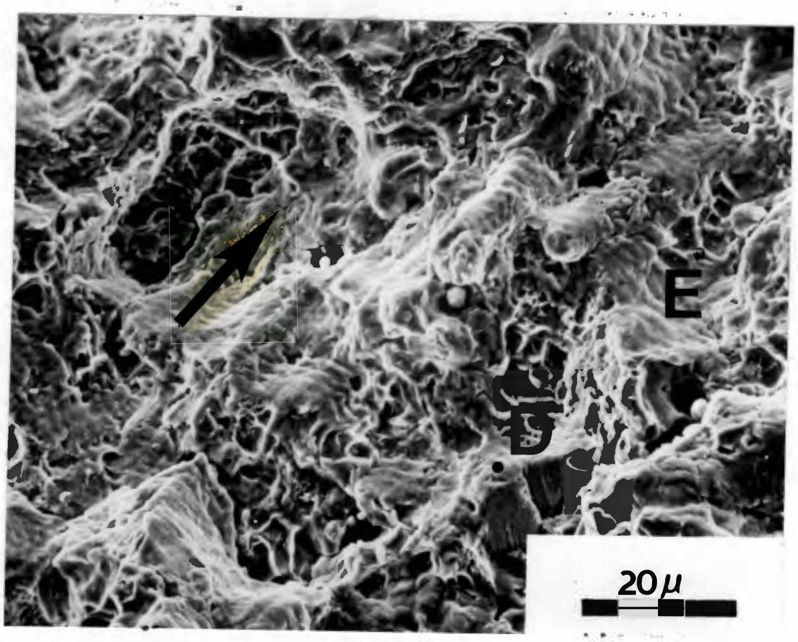

A. 1000x.

Figure 48. SEM Micrographs of Striations Observed at a Point 0.10 Inches (2.5 mm) from the Edge of a D-24 Fracture Surface. Specimen Failed after 8.30×10^5 Cycles; Applied Stress, 34042 psi (235 MN/m^2) (56% of the YS). Points D, E, and F Show, Respectively, a Pearlite Colony, a Region of Ductile Fracture, and Inclusions. Arrows Show Microscopic Crack Propagation Direction.

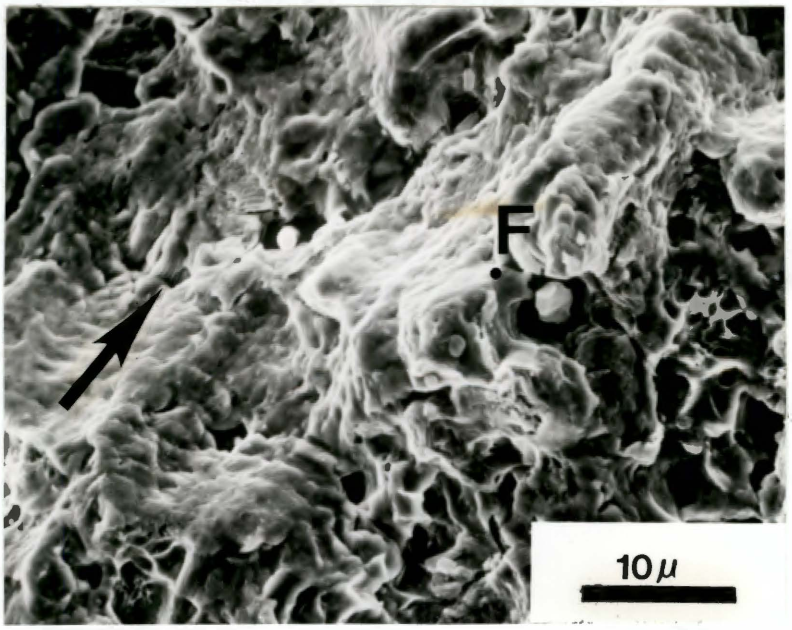

B. 2000x.

Figure 48. (Continued).

was 34042 psi (235 MN/m^2) (38% of the D-24 UTS and 56% of the D-24 YS). Figure 48A shows that striations cover the major portion of the micrograph. Unlike most of the striations observed in primary ferrite areas, the striations observed here are poorly defined and have a spacing which is essentially constant (approximately 5.0×10^{-5} inches or 0.1 microns). Point D in Figure 48A shows a pearlite colony, and point E in the same figure shows a region of ductile fracture. In Figure 48B several inclusions are evident in the vicinity of point F.

The Influence of Decarburization on Surface Appearance

Although decarburization had a negligible effect on the macroscopic surface appearance, the scanning electron microscopy (SEM) proved that the presence of surface decarburization greatly affects the striation morphology. While striations were observed in both decarburized and non-decarburized regions, the evidence presented in the fractographic analysis of these specimens clearly indicates that striations are invariably more prone to form in the primary ferrite. This has also recently been reported by Aita and Weertman (1). The striations shown here correlate closely with the work of Koterazawa and associates (46) who found, as did this author, the quasi-striation to be the predominant fatigue pattern in medium carbon steel.

Summary

While the macroscopic surface appearances observed here were found to show three different morphologies, none of the specimens exhibited the classical beach marks which are commonly associated with fatigue failures. Although the origin of crack initiation was easily determined for most specimens which were tested at low and medium applied stresses, recognition of the crack initiation site for specimens tested at high stresses (above the YS) was not always possible.

Micro-examination (SEM observation for the most part) indicated that two types of fatigue striations existed: (1) mutually parallel striations, and (2) quasi-striations. While both types were present in the fracture surfaces, quasi-striations were commonly observed. Striation density, which was greatly enhanced by an increase in depth of decarburization, was affected by the applied in the following ways: at stresses near and above the YS, an area of ductile fracture covered the major portion of the fracture surface, but as the applied stress decreased the percentage of area covered by ductile fracture decreased and the precentage of area covered by striations (both mutually parallel and quasi-striation) increased; however, as the endurance limit of each S-N curve was approached the area covered by striations (both mutually parallel and quasi-striation) decreased and was replaced by a rubbed surface appearance. The fatigue pattern most common to these conditions was tire tracks, a characteristic which resulted from the continued piercing of the fracture surface by a protrusion from the mating fracture surface.

Visibility of all fatigue patterns was, in general, limited to magnifications of 450x and above, although for applied stresses above the yield strength striations were observed at lower magnifications. Striations observed in the non-decarburized regions (core microstructure) were, for the most part, poorly defined and, in general, surrounded by pearlite colonies, inclusions and regions of ductile fracture. Microscopic crack propagation directions were found to deviate several tens of degrees from the macroscopic direction. The non-constant spacing of quasi-striations prevented the correlation of applied stress with striation spacing, a correlation which as been found to exist in the classical studies conducted using aluminum alloys.

Although much research remains to be conducted for carbon steels, this study has provided information regarding striation morphology in both decarburized and non-decarburized medium carbon steels. Furthermore, the combination of the fatigue tests, tensile tests, and fatigue fractography has provided a more detailed examination of decarburization in SAE 1042 steel than has been previously reported.

CHAPTER 6

CONCLUSIONS

The studies of decarburization in SAE 1042 steel and its effect on fatigue life, tensile properties, and fatigue fractography have yielded conclusions which are categorized in the following three areas.

Effects of Decarburization

1. The presence of a decarburized surface layer severly reduces the fatigue life in a normalized medium carbon steel. Although additional damage to fatigue life is incurred as the depth of decarburization is increased, the initial decarburization has the greatest effect on the fraction of life degradation.

2. Monotonic tensile loading does not indicate degradation of fatigue strength. Although there is some degradation in both the yield and tensile strengths with decarburization, the amount of degradation is insignificant until a large amount of decarburization is observed.

3. The removal of the decarburized surface layer by a subsequent machining operation can completely restore the initial tensile properties.

Macroscopic Surface Appearance

While decarburization has a negligible effect on the macroscopic surface appearance in fatigue failures, variation in the applied stress of fatigue tests results in the occurrence of three distinct fracture surface appearances: (1) a "jagged" fracture surface at high stresses (above the YS), (2) a "ratcheted" fracture surface at medium stresses (approximately 1/2 of the UTS) (below the YS), and (3) a "smooth" fracture surface at low stresses (approximately 1/2 of the YS). Numerical stress values at which one surface appearance surrenders to another surface appearance are not clearly defined, but the regions of change are apparently related to the tensile and yield strengths.

Striation Visibility, Density, and Spacing

1. Ductile fatigue striations, in general, are visible at magnifications above 450x. Striations are observed in both decarburized and non-decarburized regions, but are more prevalent in the primary ferrite.

2. Striation density is enhanced by (1) a reduction in the applied stress, and (2) an increase in the depth of surface decarburization.

3. Although striation spacing was found to increase with an increase in the fracture stress, no direct correlation between the applied stress and striation spacing can be determined for materials which exhibit primarily "quasi-striation" fatigue patterns.

CHAPTER 7

FUTURE WORK

The study of the effects of decarburization on fatigue life, tensile properties, and fatigue fractography in SAE 1042 steel has shown the necessity for expanded research in the following related areas.

1. Fatigue tests should be run using specimens which are initially decarburized, but will have had the decarburized surface layer removed by machining prior to testing.

2. Striation morphology in steels should be studied, utilizing unidirectional bending.

3. A categorization of fatigue patterns and the materials in which they are found should be implemented.

4. A thorough investigation of the crack initiation stage should be conducted in microstructures common to carbon steels to determine crack initiation times for various levels of applied stress.

5. Microscopic crack propagation rates should be examined in microstructures such as ferrite, pearlite, and martensite to give quantitative crack propagation rates.

LIST OF REFERENCES

LIST OF REFERENCES

1. Aita, C. R., and Weertman, J. R., "Effects of Tensile Overloads and Crack Closure on Fatigue Crack Propagation," Northwestern University Materials Research Center Annual Technical Report, No. 17, Northwestern University Research Center, August, 1976, pp. 60-61.

2. Almen, J. O., "Fatigue Weakness of Surfaces," Product Engineering, vol. 21, November, 1950, pp. 117-125.

3. Almen, J. O., and Black, P. H., Residual Stresses and Fatigue in Metals, McGraw-Hill, 1963, pp. 42-58, and pp. 78-79.

4. Andrew, J. H., and Richardson, G. T., "An Investigation of Spring Steels," J. Iron and Steel Institute, vol. 131, No. 1, 1935, pp. 129-136.

5. ASM, "Selection for Fatigue Resistance," Metals Handbook, 8th ed., vol. 1, American Society for Metals, 1961, pp. 223-224.

6. ASM, "Induction Hardening and Tempering," Metals Handbook, 8th ed., vol. 2, American Society for Metals, 1964, pp. 178-181.

7. ASM, "Use of Fractography for Failure Analysis," Metals Handbook, 8th ed., vol. 9, American Society for Metals, 1974, pp. 106-122.

8. ASTM, "Tension Testing of Metallic Materials (E 8)," Annual Book of ASTM Standards, American Society for Testing and Materials, 1972, p. 207.

9. ASTM, "Constant Amplitude Axial Fatigue Tests of Metallic Materials (E 466)," Annual Book of ASTM Standards, American Society for Testing and Materials, 1972, pp. 1063-1067.

10. Battelle Memorial Institute, SEM/TEM Fractography Handbook, Metals and Ceramics Information Center, December, 1975, pp. 25-46.

11. Beachem, C. D., Brown, B. F., and Edwards, A. J., "Characterizing Fractures by Electron Fractography," Part 12, Defense Documentation Center, U.S. Naval Research Laboratory, Washington, D. C., June, 1963, pp. 1-10.

12. Beachem, C. D., "Microscopic Fatigue Fracture Surface Features in 2024-T3 Aluminum and the Influence of Crack Propagation Angle Upon Their Formation," Trans. ASM, vol. 60, 1967, pp. 324-342.

13. Beachem, C. D., "Microscopic Fracture Processes," Fracture, An Advanced Treatise, vol. 1, Academic Press, 1968, pp. 346-347.

14. Boegehold, A. L., "Plain Carbon Steel: Its Utility for Automobiles," Metals Progress, vol. 31, 1937, pp. 147-152.

15. Broadston, J.A., "Surface-Finish Requirements in Design," ASME Handbook, Metals Engineering Design, 2nd ed., McGraw-Hill, 1965, pp. 593-604.

16. Broek, D., "Particles and Crack Growth in Aluminum Alloys," Proceedings of an International Conference on Prospects of Fracture Mechanics, Noordhoph International Publishing, 1974, pp. 19-25.

17. Bullens, D. K., Steel and Its Heat Treatment, 5th ed., vol. 3, John Wiley and Sons, 1949, pp. 303-313.

18. Burns, G., "The Properties of Some Silco-Manganese Steels," J. Iron and Steel Institute, vol. 125, No. 1, 1932, pp. 379-384.

19. Byars, E. F., and Snyder, R. D., Engineering Mechanics of Deformable Bodies, 2nd ed., International Textbook Company, 1969, pp. 369-371.

20. Cazaud, R., and Fenner, A. J., Fatigue of Metals, Chapman and Hall, 1953, pp. 180-187.

21. Christensen, R. H., and Harmon, M. B., "Limitations of Fatigue-Crack Research in the Design of Flight Vehicle Structures," Fatigue Crack Propagation, ASTM STP 415, American Society for Testing and Materials, 1967, pp. 5-22.

22. Cottrell, A. H., "Theoretical Aspects of Fracture," Fracture, The Massachusetts Institute of Technology Press, 1959, pp. 40-42.

23. Crussard, C., Plateau, J., Tamhankar, R., Henry, G., and Lajeunesse, D., "A Comparison of Ductile and Fatigue Fractures," Fracture, The Massachusetts Institute of Technology Press, 1959, pp. 524-558.

24. Dolan, T. J., "Method of Testing," ASME Handbook, Metals Engineering Design, 2nd ed., McGraw-Hill, 1965, pp. 199-206.

25. Edgerton, C. T., "Abstract of Progress Report No. 3 on Heavy Helical Springs," Trans. ASME, vol. 59, 1937, pp. 609-616.

26. Fluck, P. G., "The Influence of Surface Roughness on The Fatigue Life and Scatter of Test Results of Two Steels," Proc. ASTM, vol. 51, 1951, pp. 584-591.

27. France, R. D., "Endurance Testing of Steel: Comparison of Results Obtained with Rotating-Beam verses Axially-Loaded Specimens," Proc. ASTM, vol. 31, Part 2, 1931, pp. 176-191.

28. Gill, E. T., and Goodacre, R., "Some Aspects of the Fatigue Properties of Patented Steel Wire," J. Iron and Steel Institute, vol. 130, No. 2, 1934, pp. 293-316.

29. Gough, H. J., and Hanson, D., "The Behavior of Metals Subjected to Repeated Stresses," Proc. Royal Society London, Series A, vol. 104, 1923, pp. 538-551.

30. Grosskreutz, J. C., "The Mechanisms of Metal Fatigue (2)," Physica Status Solidi, vol. 47, Part 1, 1971, pp. 359-394.

31. Grover, H. J., Gordon, S. A., and Jackson, L. R., Fatigue of Metals and Structures, Bureau of Aeronautics, Department of the Navy, U.S. Government Printing Office, 1954, pp. 16-41, pp. 63-68, and pp. 86-113.

32. Hankins, G. A., and Becker, M. L., "The Effect of Surface Conditions Produced by Heat Treatment on the Fatigue Resistance of Spring Steels," J. Iron and Steel Institute, vol. 124, No. 2, 1931, pp. 387-460.

33. Hankins, G. A., Becker, M. L., and Mills, H. R., "Further Experiments on the Effect of Surface Conditions on Fatigue Resistance of Steels," J. Iron and Steel Institute, vol. 133, No. 1, 1936, pp. 399-419.

34. Hanley, B. C., and Dolan, T. J., "Surface Finish," ASME Handbook, Metals Engineering Design, 2nd ed., McGraw-Hill, 1965, pp. 215-224.

35. Haythorne, P. A., "Decarburization in Highly Stressed Steels," Iron Age, vol. 158, July, 1946, pp. 52-61.

36. Henriksen, E. K., "Residual Stresses in Machined Surfaces," Trans. ASME, vol. 73, January, 1951, pp. 69-76.

37. Hertzberg, R. W., "Fatigue Fracture Surface Appearance," Fatigue Crack Propagation, ASTM STP 415, American Society for Testing and Materials, 1967, pp. 205-225.

38. Hertzberg, R. W., and Mills, W. J., "Character of Fatigue Fracture Surface Micromorphology in the Ultra-Low Growth Rate Regime," Fractography-Microscopic Cracking Processes, ASTM STP 600, American Society for Testing and Materials, 1976, pp. 220-234.

39. Horger, O. J., "Fatigue Strength-1," Product Engineering, vol. 11, 1940, pp. 490-493.

40. Horger, O. J., "Fatigue Strength-3," Product Engineering, vol. 12, 1941, pp. 22-24.

41. Horger, O. J., "Stressing Axles by Cold Rolling," Surface Stressing of Metals, American Society for Metals, 1947, pp. 119-135.

42. Horger, O. J., "Decarburization," ASME Handbook, Metals Engineering Design, 2nd ed., McGraw-Hill, 1965, pp. 278-282.

43. Horger, O. J., "Residual Stresses," ASME Handbook, Metals Engineering Design, 2nd ed., McGraw-Hill, 1965, pp. 135-151.

44. Jackson, L. R., and Pochapsky, T. E., "The Effect of Composition on the Fatigue Strength of Decarburized Steel," Trans. ASM, vol. 39, 1947, pp. 45-57.

45. Joshi, S. R., and Shewchuk, J., "Fatigue-Crack Propagation in a Biaxial-Stress Field," Experimental Mechanics, vol. 10, December, 1970, pp. 529-533.

46. Koterazawa, R., Mori, M., Matsui, T., and Shimo, D., Fractographic Study of Fatigue Crack Propagation," Trans. ASME, and J. Engineering Materials and Technology, vol. 95, No. 4, Series H, October, 1973, pp. 202-211.

47. Krouse, G. N., "A High-Speed Fatigue-Testing Machine and Some Tests of Speed Effect on Endurance Limit," Proc. ASTM, vol. 34, Part 2, 1934, pp. 156-160.

48. Laird, C., and Smith, G. C., "Crack Propagation in High Stress Fatigue," Philosophical Magazine, 8th Series, vol. 7, Part 1, No. 77, May, 1962, pp. 847-856.

49. Lipson, C., Noll, G. C., and Clock, L.S., Stress and Strength of Manufactured Parts, 1st ed., McGraw-Hill, 1950, pp. 6-56.

50. McEvily, A. J., and Johnston, T. L., "The Role of Cross-Slip in Brittle Fracture and Fatigue," International Conference on Fracture, 1st, Sendai, Japan, 1965, pp. 515-546.

51. McMillian, J. C., and Hertzberg, R. W., "Application of Electron Fractography to Fatigue Studies," Electron Fractography, ASTM STP 436, American Society for Testing and Materials, 1968, pp. 89-123.

52. Moore, H. F., and Alleman, N. J., "Fatigue Tests of Carburized Steel," Trans. A.S.S.T., vol. 13, No. 3, March, 1928, pp. 405-417.

53. Oberg, T. T., and Johnson, J. B., "Fatigue Properties of Metals Used in Aircraft Construction at 3450 and 10,600 Cycles," Proc. ASTM, vol. 37, Part 2, 1935, pp. 195-205.

54. Paris, P. C., "The Fracture Mechanics Approach to Fatigue," Sagamore Army Materials Research Conference and Proceedings, vol. 11, The Syracuse University Press, 1964, pp. 107-126.

55. Pelloux, R. M. N., "Fractographic Analysis of the Influence of Constituent Particles on Fatigue Crack Propagation in Aluminum Alloys," Trans. ASM, vol. 57, 1964, pp. 511-518.

56. Pelloux, R. M. N., "Mechanisms of Formation of Ductile Fatigue Striations," Trans. ASM, vol. 62, 1969, pp. 281-285.

57. Phillips, A., et al., Electron Fractography Handbook, AFML-TR-64-416, Air Force Materials Laboratory, Wright-Patterson Air Force Base, January, 1965, pp. (2-1)-(2-19).

58. Polakowski, N. H., and Palchoudhuri, A., "Softening of Certain Cold-Worked Metals Under the Action of Fatigue Loads," Proc. ASM, vol. 54, 1954, pp. 701-712.

59. Polakowski, N. H., and Ripling, E. J., Strength and Structure of Engineering Materials, Prentice-Hall, 1966, pp. 458-521.

60. Richards, D. G., "Relief and Redistribution of Stresses," Residual Stress Measurements, American Society for Metals, 1952, pp. 152-163.

61. Robinson, G. H., "The Effect of Surface Condition on the Fatigue Resistance of Hardened Steel," Fatigue Durability of Carburized Steel, American Society for Metals, 1957, pp. 11-22.

62. Rozovsky, E., Weiss, B.Z., and Niedzwiedz, S., "Fatigue Crack Propagation in a Si-Mn Steel Under Constant Deflection," Trans. ASM, vol. 60, 1967, pp. 187-193.

63. Schijve, J., "Significance of Fatigue Cracks in Micro-Range and Macro-Range," Fatigue Crack Propagation, ASTM STP 415, American Society for Testing and Materials, 1967, pp. 415-451.

64. Shah, J. B., "Failure Analysis of Aircraft Accidents-Part 2," Metals Engineering Quarterly, November, 1974, pp. 23-29.

65. Sih, G. C., van Elst, H. C., and Broek, D., "Reflections on the Conference," Proceedings of an International Conference on Prospects of Fracture Mechanics, Noordhopf International Publishing, 1974, pp. xiii-xviii.

66. Sines, G., and Waisman, J. L., Metal Fatigue, University of California Extension Series, McGraw-Hill, 1959, pp. 32-34.

67. Spiegler, B., Weiss, B. Z., and Taub, A., "Influence of Decarburization on the Fatigue Properties and the Propagation of Cracks in Silicon Steels," J. Iron and Steel Institute, vol. 202, June, 1964, pp. 509-517.

68. Spotts, M. F., Design of Machine Parts, Prentice-Hall, 1971, pp. 83-89.

69. Van Stone, R. H., and Cox, T. B., "Use of Fractography and Sectioning Techniques to Study Fracture Mechanisms," Fractography-Microscopic Cracking Processes, ASTM STP 600, American Society for Testing and Materials, 1976, pp. 5-29.

70. Weiss, B. Z., Niedzwiedz, S., and Breuer, M., "Influence of Temper Brittleness on Fatigue Properties and the Initiation and Propagation of Fatigue Cracks in Silicon Steels," J. Iron and Steel Institute, vol. 204, February, 1966, pp. 152-156.

71. Zackay, V. F., Gerberich, W. W., and Parker, E. R., "Structural Modes of Fracture," Fracture, An Advanced Treatise, Academic Press, vol. 1, 1968, pp. 416-423.

APPENDIXES

APPENDIX A

```
      *******************************************************************
      * THIS PROGRAM PLOTS FOUR GRAPHS USING DATA COLLECTED DURING THE *
      * STUDY OF THE EFFECTS OF DECARBURIZATION ON THE FATIGUE LIFE    *
      * OF SAE 1042 STEEL.  GRAPHS 1 & 2 CONTAIN S-N DATA AND GRAPHS   *
      * 3 & 4 CONTAIN MICROHARDNESS DATA.  GRAPHS 2 & 4 HAVE 'DEGREE   *
      * OF BEST FIT' CURVES DRAWN AND THE EQUATION OF THE CURVE        *
      * DETERMINED BY A LEAST SQUARES REGRESSION ANALYSIS LISTED.      *
      *******************************************************************

      DIMENSION X5(47),    Y5(47),
     $          X10(47),   Y10(47),
     $          X15(43),   Y15(43),
     $          X20(43),   Y20(43),
     $          X30(110),  Y30(110),
     $          X35(102),  Y35(102),
     $          X40(112),  Y40(112),
     $          X45(110),  Y45(110), IAREA(554)
      REAL LG5X(47), LG10X(47), LG15X(43), LG20X(43)
      INTEGER INT(2)/5,0/
      INTEGER INTE(2)/3,0/
      INTEGER INTEG(2)/1,0/
      CALL PLOTS (IAREA,664,120.0)
      CALL ZIPOFF
      CALL PLOT (3.0,2.5,-3)

      S-N DATA - AS RECEIVED - SAE 1042 C.F.
      READ (5,580) X
      READ (5,590) (Y5(I),  X5(I),  I=1,45)

      S-N DATA - NO DECARBURIZATION
      READ (5,580) X
      READ (5,590) (Y10(I), X10(I), I=1,45)

      S-N DATA - 38 MIL DECARBURIZED DEPTH
      READ (5,580) X
      READ (5,590) (Y15(I), X15(I), I=1,41)

      S-N DATA - 80 MIL DECARBURIZED DEPTH
      READ (5,580) X
      READ (5,590) (Y20(I), X20(I), I=1,41)

      MICROHARDNESS DATA - AS RECEIVED - SAE 1042 C.F.
      READ (5,580) X
      READ (5,560) (Y30(I), X30(I), I=1,108)

      MICROHARDNESS DATA - 1 HOUR AT 1550 F. - NO DECARBURIZATION
      READ (5,580) X
      READ (5,560) (Y35(I), X35(I), I=1,100)

      MICROHARDNESS DATA - 8 HRS. AT 1550 F. - 38 MIL DECARBURIZED DEPTH
      READ (5,580) X
      READ (5,560) (Y40(I), X40(I), I=1,110)

      MICROHARDNESS DATA - 24 HRS. AT 1550 F. - 80 MIL DECARBURIZED DEPTH
      READ (5,580) X
      READ (5,560) (Y45(I), X45(I), I=1,108)
```

S-N DATA - AS RECEIVED - SAE 1042 C.F.

OBS	Y	X	LX	LX2	LX3	LX4
1	95069	2600	3.41497	11.6620	39.826	136.00
2	95069	2200	3.34242	11.1718	37.341	124.81
3	95069	2500	3.39794	11.5460	39.233	133.31
4	89032	2600	3.41497	11.6620	39.826	136.00
5	89032	4300	3.63347	13.2021	47.969	174.30
6	89032	4300	3.63347	13.2021	47.969	174.30
7	82996	2800	3.44716	11.8829	40.962	141.20
8	82996	4100	3.61278	13.0522	47.155	170.36
9	82996	4400	3.64345	13.2747	48.366	176.22
10	79978	3200	3.50515	12.2861	43.065	150.95
11	79978	5800	3.76343	14.1634	53.303	200.60
12	79978	5600	3.74819	14.0489	52.658	197.37
13	76960	5700	3.75587	14.1066	52.983	199.00
14	76960	6800	3.83251	14.6881	56.292	215.74
15	73942	6400	3.80618	14.4870	55.140	209.87
16	73942	6900	3.83885	14.7368	56.572	217.17
17	70924	13800	4.13988	17.1386	70.952	293.73
18	70924	9200	3.96379	15.7116	62.278	246.85
19	70924	11000	4.04139	16.3329	66.007	266.76
20	67906	12500	4.09691	16.7847	68.765	281.73
21	67906	14100	4.14922	17.2160	71.433	296.39
22	64888	26000	4.41497	19.4920	86.057	379.94
23	64888	26500	4.42325	19.5651	86.541	382.79
24	61870	39800	4.59988	21.1589	97.329	447.70
25	61870	21900	4.34044	18.8395	81.772	354.93
26	61870	34200	4.53403	20.5574	93.208	422.61
27	58852	64000	4.80618	23.0994	111.020	533.58
28	58852	29600	4.47129	19.9924	89.392	399.70
29	58852	46300	4.66558	21.7676	101.559	473.83
30	55834	104600	5.01953	25.1957	126.471	634.82
31	55834	80800	4.90741	24.0827	118.184	579.98
32	52816	108600	5.03583	25.3596	127.707	643.11
33	52816	213900	5.33021	28.4111	151.437	807.19
34	52816	212500	5.32736	28.3808	151.194	805.47
35	49798	293500	5.46761	29.8947	163.453	893.70
36	49798	188800	5.27600	27.8362	146.864	774.85
37	46780	567800	5.75420	33.1108	190.526	1096.32
38	46780	932400	5.96960	35.6362	212.734	1269.94
39	43762	1597200	6.20336	38.4817	238.716	1480.84
40	43762	1772400	6.24856	39.0445	243.972	1524.47
41	43762	1812800	6.25835	39.1669	245.120	1534.05
42	40744	4272300	6.63066	43.9657	291.522	1932.98
43	40744	6824600	6.83408	46.7046	319.183	2181.32
44	39235	106000000	8.02531	64.4055	516.874	4148.07
45	39235	100000000	8.00000	64.0000	512.000	4096.00

S-N DATA - AS RECEIVED - SAE 1042 C.F.

GENERAL LINEAR MODELS PROCEDURE

DEPENDENT VARIABLE: Y

SOURCE	DF	SUM OF SQUARES	MEAN SQUARE	F VALUE	PR > F	R-SQUARE	C.V.
MODEL	3	12070914954.5490090	4023638318.1830030	510.80	0.0001	0.973942	4.2987
ERROR	41	322960180.6510029	7877077.5768537		STD DEV		Y MEAN
CORRECTED TOTAL	44	12393875135.2000120			2806.6131862		65290.46666667

SOURCE	DF	TYPE I SS	F VALUE	PR > F	DF	TYPE IV SS	F VALUE	PR > F
LX	1	10331164193.2145940	1311.55	0.0001	1	350620415.0382301	44.51	0.0001
LX2	1	1618091586.3024511	205.42	0.0001	1	194723837.0441604	24.72	0.0001
LX3	1	121659175.0319634	15.44	0.0003	1	121659175.0319634	15.44	0.0003

PARAMETER	ESTIMATE	T FOR H0: PARAMETER=0	PR > |T|	STD ERROR OF ESTIMATE
INTERCEPT	342395.25964182	10.80	0.0001	31694.31719785
LX	-122414.74848047	-6.67	0.0001	18348.37916498
LX2	16937.62755493	4.97	0.0001	3406.63481713
LX3	-797.52060521	-3.93	0.0003	202.93270309

S-N DATA - 1 HOUR AT 1550 F. - NO DECARBURIZATION

OBS	Y	X	LX	LX2	LX3	LX4
1	86014	3000	3.47712	12.0904	42.040	146.18
2	86014	2800	3.44716	11.8829	40.962	141.20
3	86014	2700	3.43136	11.7743	40.402	138.63
4	82996	3100	3.49136	12.1896	42.558	148.59
5	82996	3100	3.49136	12.1896	42.558	148.59
6	79978	3900	3.59106	12.8957	46.309	166.30
7	79978	4100	3.61278	13.0522	47.155	170.36
8	79091	3600	3.55630	12.6473	44.978	159.95
9	76960	5700	3.75587	14.1066	52.983	199.00
10	76960	5600	3.74819	14.0489	52.658	197.37
11	73962	5900	3.77085	14.2193	53.619	202.19
12	73962	6900	3.83885	14.7368	56.572	217.17
13	73232	5600	3.74819	14.0489	52.658	197.37
14	71004	6800	3.83251	14.6881	56.292	215.74
15	71004	9100	3.95904	15.6740	62.054	245.67
16	68045	8900	3.94939	15.5977	61.601	243.29
17	68045	10100	4.00432	16.0346	64.208	257.11
18	67374	10400	4.01703	16.1366	64.821	260.39
19	65087	11900	4.07555	16.6101	67.695	275.89
20	65087	13200	4.12057	16.9791	69.964	288.29
21	64017	13500	4.13033	17.0597	70.462	291.03
22	62128	18300	4.26245	18.1685	77.442	330.09
23	62128	17800	4.25042	18.0661	76.788	326.38
24	59170	19800	4.29667	18.4613	79.322	340.82
25	59170	21000	4.32222	18.6816	80.746	349.00
26	56396	30400	4.48287	20.0962	90.089	403.86
27	56211	27200	4.43457	19.6654	87.208	386.73
28	56211	24700	4.39270	19.2958	84.761	372.33
29	53253	41200	4.61490	21.2973	98.285	453.57
30	53253	33100	4.51983	20.4288	92.335	417.34
31	50797	64600	4.81023	23.1383	111.301	535.38
32	50797	55500	4.74429	22.5083	106.786	506.62
33	50299	69300	4.84073	23.4327	113.431	549.09
34	47809	133500	5.12548	26.2706	134.649	690.14
35	47809	94100	4.97359	24.7366	123.030	611.90
36	44821	334300	5.52414	30.5161	168.575	931.23
37	44821	166800	5.22220	27.2713	142.416	743.73
38	44202	357400	5.55315	30.8375	171.246	950.95
39	41833	351900	5.54642	30.7628	170.623	946.35
40	41833	613100	5.78753	33.4955	193.856	1121.95
41	39545	1267500	6.10295	37.2460	227.310	1387.26
42	39545	1875700	6.27316	39.3526	246.865	1548.63
43	38081	12768000	7.10612	50.4970	358.838	2549.95
44	36581	101000000	8.00432	64.0692	512.830	4104.86
45	36217	102000000	8.00860	64.1377	513.653	4113.64

S-N DATA - 1 HOUR AT 1550 F. - NO DECARBURIZATION

GENERAL LINEAR MODELS PROCEDURE

DEPENDENT VARIABLE: Y

SOURCE	DF	SUM OF SQUARES	MEAN SQUARE	F VALUE	PR > F	R-SQUARE	C.V.
MODEL	3	10274276171.9353100	3424758723.9784367	2383.61	0.0001	0.994299	1.9609
ERROR	41	58908524.0646896	1436793.2698705		STD DEV		Y MEAN
CORRECTED TOTAL	44	10333184696.0000000			1198.6631178		61127.33333333

SOURCE	DF	TYPE I SS	F VALUE	PR > F	DF	TYPE IV SS	F VALUE	PR > F
LX	1	8090254049.9191950	5630.77	0.0001	1	396619730.7494764	276.05	0.0001
LX2	1	2030680677.3811317	1413.34	0.0001	1	235303182.2425726	163.77	0.0001
LX3	1	153341444.6349840	106.72	0.0001	1	153341444.6349840	106.72	0.0001

PARAMETER	ESTIMATE	T FOR H0: PARAMETER=0	PR > |T|	STD ERROR OF ESTIMATE
INTERCEPT	389014.11671104	25.02	0.0001	15549.63670932
LX	-149847.11057136	-16.61	0.0001	9018.99939734
LX2	21510.81565472	12.80	0.0001	1680.89320145
LX3	-1036.29836926	-10.33	0.0001	100.31183662

S-N DATA - 8 HOURS AT 1550 F. - 38 MIL DECARBURIZED DEPTH

OBS	Y	X	LX	LX2	LX3	LX4
1	85199	2100	3.32222	11.0371	36.668	121.82
2	85199	2600	3.41497	11.6620	39.826	136.00
3	81824	2700	3.43136	11.7743	40.402	138.63
4	81824	3600	3.55630	12.6473	44.978	159.95
5	76915	3700	3.56820	12.7321	45.431	162.11
6	76915	4400	3.64345	13.2747	48.366	176.22
7	74404	5700	3.75587	14.1066	52.983	199.00
8	73642	4600	3.66276	13.4158	49.139	179.98
9	69930	7100	3.85126	14.8322	57.123	219.99
10	69930	5900	3.77085	14.2193	53.619	202.19
11	66203	8300	3.91908	15.3592	60.194	235.90
12	66203	8400	3.92428	15.4000	60.434	237.16
13	63482	7700	3.88649	15.1048	58.705	228.16
14	63108	10400	4.01703	16.1366	64.821	260.39
15	60045	11100	4.04532	16.3646	66.200	267.80
16	60045	12800	4.10721	16.8692	69.285	284.57
17	58721	15700	4.19590	17.6056	73.871	309.96
18	58721	13000	4.11394	16.9245	69.627	286.44
19	55129	18800	4.27416	18.2684	78.082	333.74
20	55129	12300	4.08991	16.7273	68.413	279.80
21	53429	21500	4.33244	18.7700	81.320	352.31
22	53429	16700	4.22272	17.8313	75.297	317.96
23	51042	27100	4.43297	19.6512	87.113	386.17
24	50508	29800	4.47422	20.0186	89.568	400.74
25	49199	33300	4.52244	20.4525	92.495	418.30
26	48951	35900	4.55509	20.7489	94.513	430.52
27	47757	61800	4.79099	22.9536	109.970	526.87
28	46535	81100	4.90902	24.0985	118.300	580.74
29	45575	101300	5.00561	25.0561	125.421	627.81
30	43535	116500	5.06633	25.6677	130.041	658.83
31	43535	139000	5.14301	26.4506	136.036	699.63
32	41364	195800	5.29181	28.0033	148.188	784.18
33	41364	258200	5.41196	29.2893	158.512	857.86
34	38316	304600	5.48373	30.0713	164.903	904.28
35	38316	528100	5.72272	32.7495	187.416	1072.53
36	35818	614900	5.78880	33.5103	193.984	1122.94
37	35448	1651300	6.21783	38.6614	240.390	1494.70
38	32730	4320900	6.63557	44.0308	292.170	1938.72
39	32730	17534900	7.24390	52.4741	380.118	2753.53
40	31741	101000000	8.00432	64.0692	512.830	4104.86
41	31741	103000000	8.01284	64.2056	514.469	4122.35

S-N DATA - 8 HOURS AT 1550 F. - 38 MIL DECARBURIZED DEPTH

GENERAL LINEAR MODELS PROCEDURE

DEPENDENT VARIABLE: Y

SOURCE	DF	SUM OF SQUARES	MEAN SQUARE	F VALUE	PR > F	R-SQUARE	C.V.
MODEL	3	10037212797.3021420	3345737599.1007140	810.78	0.0001	0.985016	3.6600
ERROR	37	152682743.1368837	4126560.6253212		STD DEV		Y MEAN
CORRECTED TOTAL	40	10189895540.4390250			2031.3937642		55503.19512195

SOURCE	DF	TYPE I SS	F VALUE	PR > F	DF	TYPE IV SS	F VALUE	PR > F
LX	1	7774147451.3371770	1883.93	0.0001	1	507905222.4189825	123.08	0.0001
LX2	1	2043875277.2433345	495.30	0.0001	1	318951396.4266123	77.29	0.0001
LX3	1	219190068.7216312	53.12	0.0001	1	219190068.7216312	53.12	0.0001

PARAMETER	ESTIMATE	T FOR H0: PARAMETER=0	PR > |T|	STD ERROR OF ESTIMATE
INTERCEPT	417449.17967473	15.93	0.0001	26203.19456597
LX	-168101.65362136	-11.09	0.0001	15152.16745795
LX2	24775.14723953	8.79	0.0001	2818.04617662
LX3	-1224.75681450	-7.29	0.0001	168.04807543

S-N DATA - 24 HOURS AT 1550 F. - 80 MIL DECARBURIZED DEPTH

OBS	Y	X	LX	LX2	LX3	LX4
1	76097	2100	3.32222	11.0371	36.668	121.82
2	76097	2400	3.38021	11.4258	38.622	130.55
3	74447	2400	3.38021	11.4258	38.622	130.55
4	74447	2600	3.41497	11.6620	39.826	136.00
5	72488	3300	3.51851	12.3799	43.559	153.26
6	72488	2800	3.44716	11.8829	40.962	141.20
7	69232	2900	3.46240	11.9882	41.508	143.72
8	69232	4300	3.63347	13.2021	47.969	174.30
9	67095	4400	3.64345	13.2747	48.366	176.22
10	67095	4300	3.63347	13.2021	47.969	174.30
11	63786	4600	3.66276	13.4158	49.139	179.98
12	63786	6100	3.78533	14.3287	54.239	205.31
13	60733	6300	3.79934	14.4350	54.843	208.37
14	60733	9000	3.95424	15.6360	61.829	244.49
15	58158	8800	3.94448	15.5589	61.372	242.08
16	57510	8400	3.92428	15.4000	60.434	237.16
17	54995	9700	3.98677	15.8943	63.367	252.63
18	54995	14800	4.17026	17.3911	72.525	302.45
19	54995	14200	4.15229	17.2415	71.592	297.27
20	52065	11900	4.07555	16.6101	67.695	275.89
21	51969	15500	4.19033	17.5589	73.578	308.31
22	51179	19400	4.28780	18.3852	78.832	338.02
23	50236	25400	4.40483	19.4026	85.465	376.46
24	49680	22200	4.34635	18.8908	82.106	356.86
25	46567	55000	4.74036	22.4710	106.521	504.95
26	46567	34300	4.53529	20.5689	93.286	423.08
27	42990	51600	4.71265	22.2091	104.664	493.24
28	42990	60800	4.78390	22.8857	109.483	523.76
29	40493	151800	5.18127	26.8456	139.094	720.69
30	40257	86300	4.93601	24.3642	120.262	593.61
31	38340	171600	5.23452	27.4002	143.427	750.77
32	38340	225700	5.35353	28.6603	153.434	821.41
33	36045	320200	5.50542	30.3097	166.867	918.68
34	34042	830400	5.91929	35.0380	207.400	1227.66
35	34042	445900	5.64924	31.9139	180.289	1018.50
36	31346	1759600	6.24541	39.0052	243.604	1521.41
37	31346	1049300	6.02090	36.2512	218.265	1314.15
38	29697	4763900	6.67796	44.5952	297.805	1988.73
39	29661	26932500	7.43028	55.2090	410.218	3048.03
40	28035	101000000	8.00432	64.0692	512.830	4104.86
41	28035	102000000	8.00860	64.1377	513.653	4113.64

S-N DATA - 24 HOURS AT 1550 F. - 80 MIL DECARBURIZED DEPTH

GENERAL LINEAR MODELS PROCEDURE

DEPENDENT VARIABLE: Y

SOURCE	DF	SUM OF SQUARES	MEAN SQUARE	F VALUE	PR > F	R-SQUARE	C.V.
MODEL	3	9266808746.18270300	3088936248.72756760	1320.98	0.0001	0.990750	2.9541
ERROR	37	86519715.62218284	2338370.69249143		STD DEV		Y MEAN
CORRECTED TOTAL	40	9353328461.80488500			1529.17320552		51764.17073171

SOURCE	DF	TYPE I SS	F VALUE	PR > F	DF	TYPE IV SS	F VALUE	PR > F
LX	1	7689282525.39726300	3288.31	0.0001	1	267584700.25013385	114.43	0.0001
LX2	1	1487403013.66800050	636.09	0.0001	1	146891257.59536393	62.82	0.0001
LX3	1	90123207.11743975	38.54	0.0001	1	90123207.11743974	38.54	0.0001

PARAMETER	ESTIMATE	T FOR H0: PARAMETER=0	PR > |T|	STD ERROR OF ESTIMATE
INTERCEPT	308201.52427222	16.88	0.0001	18262.43840966
LX	-114171.70075203	-10.70	0.0001	10672.95089119
LX2	15840.65027630	7.93	0.0001	1998.62681999
LX3	-743.54854967	-6.21	0.0001	119.76990123

MICROHARDNESS DATA - AS RECEIVED - SAE 1042 C.F.

OBS	Y	X
1	229	65
2	218	105
3	236	155
4	228	205
5	233	255
6	228	305
7	244	355
8	233	405
9	240	455
10	221	505
11	229	555
12	229	605
13	244	705
14	243	805
15	221	905
16	231	1005
17	227	1055
18	236	1105
19	234	1155
20	220	1205
21	222	1255
22	227	1305
23	227	1355
24	228	1405
25	228	1455
26	227	1505
27	240	65
28	229	165
29	238	265
30	222	365
31	236	465
32	228	565
33	226	665
34	230	765
35	227	865
36	220	965
37	233	1065
38	229	1165
39	244	1265
40	233	1365
41	239	1465
42	233	1565
43	229	36
44	228	136
45	227	236
46	219	336

MICROHARDNESS DATA - AS RECEIVED - SAE 1042 C.F.

OBS	Y	X
47	239	436
48	231	536
49	244	636
50	244	736
51	222	836
52	244	936
53	234	1036
54	221	1136
55	228	1236
56	220	1336
57	235	1436
58	234	1536
59	223	39
60	239	89
61	219	189
62	231	289
63	238	389
64	241	489
65	219	589
66	244	689
67	219	789
68	238	889
69	241	989
70	223	1089
71	241	1189
72	239	1289
73	228	1389
74	241	1489
75	241	38
76	236	68
77	227	98
78	238	128
79	220	158
80	229	188
81	229	218
82	236	248
83	224	278
84	235	308
85	219	358
86	241	408
87	228	458
88	238	508
89	238	558
90	222	608
91	226	658
92	221	708

MICROHARDNESS DATA - AS RECEIVED - SAE 1042 C.F.

OBS	Y	X
93	238	758
94	240	808
95	230	858
96	227	908
97	230	958
98	235	1008
99	234	1058
100	224	1108
101	228	1158
102	228	1208
103	221	1258
104	229	1308
105	226	1358
106	239	1408
107	220	1458
108	224	1508

MICROHARDNESS DATA - AS RECEIVED - SAE 1042 C.F.

GENERAL LINEAR MODELS PROCEDURE

DEPENDENT VARIABLE: Y

SOURCE	DF	SUM OF SQUARES	MEAN SQUARE	F VALUE	PR > F	R-SQUARE	C.V.
MODEL	1	9.86760564	9.86760564	0.17	0.6767	0.001646	3.2545
ERROR	106	5984.31757955	56.45582622		STD DEV		Y MEAN
CORRECTED TOTAL	107	5994.18518519			7.51370922		230.87037037

SOURCE	DF	TYPE I SS	F VALUE	PR > F	DF	TYPE IV SS	F VALUE	PR > F
X	1	9.86760564	0.17	0.6767	1	9.86760564	0.17	0.6767

PARAMETER	ESTIMATE	T FOR H0: PARAMETER=0	PR > |T|	STD ERROR OF ESTIMATE
INTERCEPT	231.36797103	166.14	0.0001	1.39261520
X	-0.00065696	-0.42	0.6767	0.00157141

MICROHARDNESS DATA - 1 HOUR AT 1550 F. - NO DECARBURIZATION

OBS	Y	X
1	198	37
2	202	87
3	209	137
4	209	187
5	200	237
6	201	287
7	206	337
8	209	387
9	203	437
10	203	487
11	203	587
12	200	687
13	204	787
14	201	887
15	199	987
16	204	1087
17	200	1187
18	200	1287
19	202	1387
20	199	1487
21	208	94
22	208	194
23	205	294
24	209	394
25	207	494
26	200	594
27	204	694
28	200	794
29	202	894
30	199	994
31	207	1044
32	199	1094
33	207	1144
34	197	1194
35	195	1244
36	198	1294
37	200	1344
38	201	1394
39	201	1444
40	198	1494
41	207	36
42	205	86
43	203	136
44	201	186
45	201	236
46	208	286

MICROHARDNESS DATA - 1 HOUR AT 1550 F. - NO DECARBURIZATION

OBS	Y	X
47	200	386
48	199	486
49	208	586
50	206	686
51	206	786
52	209	886
53	211	986
54	211	1086
55	206	1186
56	210	1286
57	208	1336
58	205	1386
59	198	33
60	199	83
61	198	133
62	198	183
63	198	233
64	195	283
65	207	333
66	200	433
67	200	533
68	199	633
69	194	733
70	200	833
71	201	933
72	206	1033
73	197	1133
74	199	1183
75	205	1233
76	210	1283
77	205	1333
78	195	1383
79	200	1433
80	204	1483
81	206	62
82	204	112
83	207	162
84	207	212
85	206	262
86	208	362
87	205	462
88	211	562
89	203	662
90	201	762
91	205	812
92	202	862

MICROHARDNESS DATA - 1 HOUR AT 1550 F. - NO DECARBURIZATION

OBS	Y	X
93	205	912
94	202	962
95	205	1012
96	200	1112
97	200	1212
98	207	1312
99	197	1412
100	201	1512

MICROHARDNESS DATA - 1 HOUR AT 1550 F. - NO DECARBURIZATION

GENERAL LINEAR MODELS PROCEDURE

DEPENDENT VARIABLE: Y

SOURCE	DF	SUM OF SQUARES	MEAN SQUARE	F VALUE	PR > F	R-SQUARE	C.V.
MODEL	1	41.21794757	41.21794757	2.43	0.1221	0.024215	2.0289
ERROR	98	1660.97205243	16.94869441		STD DEV		Y MEAN
CORRECTED TOTAL	99	1702.19000000			4.11687921		202.91000000

SOURCE	DF	TYPE I SS	F VALUE	PR > F	DF	TYPE IV SS	F VALUE	PR > F
X	1	41.21794757	2.43	0.1221	1	41.21794757	2.43	0.1221

PARAMETER	ESTIMATE	T FOR H0: PARAMETER=0	PR > |T|	STD ERROR OF ESTIMATE
INTERCEPT	203.95223065	259.83	0.0001	0.78495061
X	-0.00139365	-1.56	0.1221	0.00089368

MICROHARDNESS DATA - 8 HOURS AT 1550 F. - 38 MIL DECARBURIZED DEPTH

OBS	Y	X	X2	X3	X4	X5	X6
1	147	16	256	4096	65536	1048576	16777216
2	151	46	2116	97336	4477456	205962976	9474296896
3	165	76	5776	438976	33362176	2535525376	192699928576
4	189	126	15876	2000376	252047376	31757969376	4.00150E+12
5	198	176	30976	5451776	959512576	168874213376	2.97219E+13
6	202	226	51076	11543176	2608757776	589579257376	1.33245E+14
7	202	276	76176	21024576	5802782976	1.60157E+12	4.42033E+14
8	206	326	106276	34645976	11294588176	3.68204E+12	1.20034E+15
9	208	376	141376	53157376	19987173376	7.51518E+12	2.82571E+15
10	205	426	181476	77308776	32933538576	1.40297E+13	5.97665E+15
11	204	526	276676	145531576	76549608976	4.02651E+13	2.11794E+16
12	211	626	391876	245314376	153566799376	9.61328E+13	6.01791E+16
13	209	726	527076	382657176	277809109776	2.01689E+14	1.46427E+17
14	210	826	682276	563559976	465500540176	3.84503E+14	3.17600E+17
15	205	926	857476	794022776	735265090576	6.80855E+14	6.30472E+17
16	201	1026	1052676	1080045576	1.10813E+12	1.13694E+15	1.16650E+18
17	201	1126	1267876	1427628376	1.60751E+12	1.81006E+15	2.03812E+18
18	207	1226	1503076	1842771176	2.25924E+12	2.76983E+15	3.39581E+18
19	201	1354	1833316	2482309864	3.36105E+12	4.55086E+15	6.16186E+18
20	142	18	324	5832	104976	1889568	34012224
21	147	48	2304	110592	5308416	254803968	12230590464
22	165	78	6084	474552	37015056	2887174368	225199600704
23	185	128	16384	2097152	268435456	34359738368	4.39805E+12
24	186	178	31684	5639752	1003875856	178689902368	3.18068E+13
25	194	228	51984	11852352	2702336256	616132666368	1.40478E+14
26	194	278	77284	21484952	5972816656	1.66044E+12	4.61603E+14
27	204	328	107584	35287552	11574317056	3.79638E+12	1.24521E+15
28	204	378	142884	54010152	20415837456	7.71719E+12	2.91710E+15
29	200	428	183184	78402752	33556377856	1.43621E+13	6.14699E+15
30	206	528	278784	147197952	77720518656	4.10364E+13	2.16672E+16
31	204	628	394384	247673152	155538739456	9.76783E+13	6.13420E+16
32	204	728	529984	385828352	280883040256	2.04483E+14	1.48864E+17
33	202	828	685584	567663552	470025421056	3.89181E+14	3.22242E+17
34	198	928	861184	799178752	741637881856	6.88240E+14	6.38687E+17
35	204	1028	1056784	1086373952	1.11679E+12	1.14806E+15	1.18021E+18
36	204	1128	1272384	1435249152	1.61896E+12	1.82619E+15	2.05994E+18
37	199	1228	1507984	1851804352	2.27402E+12	2.79249E+15	3.42918E+18
38	202	1328	1763584	2342039552	3.11023E+12	4.13038E+15	5.48515E+18
39	139	20	400	8000	160000	3200000	64000000
40	151	50	2500	125000	6250000	312500000	15625000000
41	162	80	6400	512000	40960000	3276800000	262144000000
42	176	130	16900	2197000	285610000	37129300000	4.82681E+12
43	194	180	32400	5832000	1049760000	188956800000	3.40122E+13
44	200	230	52900	12167000	2798410000	643634300000	1.48036E+14
45	198	280	78400	21952000	6146560000	1.72104E+12	4.81890E+14
46	199	330	108900	35937000	11859210000	3.91354E+12	1.29147E+15

MICROHARDNESS DATA - 8 HOURS AT 1550 F. - 38 MIL DECARBURIZED DEPTH

OBS	Y	X	X2	X3	X4	X5	X6
47	197	380	144400	54872000	20851360000	7.92352E+12	3.01094E+15
48	200	430	184900	79507000	34188010000	1.47008E+13	6.32136E+15
49	199	530	280900	148877000	78904810000	4.18195E+13	2.21644E+16
50	198	630	396900	250047000	157529610000	9.92437E+13	6.25235E+16
51	200	730	532900	389017000	283982410000	2.07307E+14	1.51334E+17
52	198	830	688900	571787000	474583210000	3.93904E+14	3.26940E+17
53	204	930	864900	804357000	748052010000	6.95688E+14	6.46990E+17
54	203	1030	1060900	1092727000	1.12551E+12	1.15927E+15	1.19405E+18
55	210	1130	1276900	1442897000	1.63047E+12	1.84244E+15	2.08195E+18
56	204	1230	1512900	1860867000	2.28887E+12	2.81531E+15	3.46283E+18
57	209	1330	1768900	2352637000	3.12901E+12	4.16158E+15	5.53490E+18
58	203	1430	2044900	2924207000	4.18162E+12	5.97971E+15	8.55099E+18
59	147	23	529	12167	279841	6436343	148035889
60	159	53	2809	148877	7890481	418195493	22164361129
61	167	83	6889	571787	47458321	3939040643	326940373369
62	179	113	12769	1442897	163047361	18424351793	2.08195E+12
63	187	163	26569	4330747	705911761	115063617043	1.87554E+13
64	194	213	45369	9663597	2058346161	438427732293	9.33851E+13
65	204	263	69169	18191447	4784350561	1.25828E+12	3.30929E+14
66	207	313	97969	30664297	9597924961	3.00415E+12	9.40299E+14
67	207	363	131769	47832147	17363069361	6.30279E+12	2.28791E+15
68	203	413	170569	70444997	29093783761	1.20157E+13	4.96250E+15
69	207	463	214369	99252847	45954068161	2.12767E+13	9.85113E+15
70	209	563	316969	178453547	100469346961	5.65642E+13	3.18457E+16
71	210	663	439569	291434247	193220905761	1.28105E+14	8.49339E+16
72	211	763	582169	444194947	338920744561	2.58597E+14	1.97309E+17
73	211	863	744769	642735647	554680863361	4.78690E+14	4.13109E+17
74	206	963	927369	893056347	860013262161	8.28193E+14	7.97550E+17
75	210	1063	1129969	1201157047	1.27683E+12	1.35727E+15	1.44278E+18
76	196	1163	1352569	1573037747	1.82944E+12	2.12764E+15	2.47445E+18
77	209	1263	1595169	2014698447	2.54456E+12	3.21378E+15	4.05901E+18
78	207	1363	1857769	2532139147	3.45131E+12	4.70413E+15	6.41173E+18
79	204	1463	2140369	3131359847	4.58118E+12	6.70227E+15	9.80541E+18
80	141	39	1521	59319	2313441	90224199	3518743761
81	154	69	4761	328509	22667121	1564031349	107918163081
82	168	99	9801	970299	96059601	9509900499	941480149401
83	180	129	16641	2146689	276922881	35723051649	4.60827E+12
84	182	159	25281	4019679	639128961	101621504799	1.61578E+13
85	185	189	35721	6751269	1275989841	241162079949	4.55796E+13
86	186	219	47961	10503459	2300257521	503756397099	1.10323E+14
87	200	249	62001	15438249	3844124001	957186876249	2.38340E+14
88	197	279	77841	21717639	6059221281	1.69052E+12	4.71656E+14
89	202	309	95481	29503629	9116621361	2.81704E+12	8.70464E+14
90	199	339	114921	38958219	13206836241	4.47712E+12	1.51774E+15
91	199	369	136161	50243409	18539817921	6.84119E+12	2.52440E+15
92	200	399	159201	63521199	25344958401	1.01126E+13	4.03494E+15

MICROHARDNESS DATA - 8 HOURS AT 1550 F. - 38 MIL DECARBURIZED DEPTH

OBS	Y	X	X2	X3	X4	X5	X6
93	203	429	184041	78953589	33871089681	1.45307E+13	6.23367E+15
94	199	479	229441	109902239	52643172481	2.52161E+13	1.20785E+16
95	204	529	279841	148035889	78310985281	4.14265E+13	2.19146E+16
96	202	579	335241	194104539	112386528081	6.50718E+13	3.76766E+16
97	206	629	395641	248858189	156531800881	9.84585E+13	6.19304E+16
98	204	679	461041	313046839	212558803681	1.44327E+14	9.79983E+16
99	205	729	531441	387420489	282429536481	2.05891E+14	1.50095E+17
100	201	779	606841	472729139	368255999281	2.86871E+14	2.23473E+17
101	202	829	687241	569722789	472300192081	3.91537E+14	3.24584E+17
102	199	879	772641	679151439	596974114881	5.24740E+14	4.61247E+17
103	202	929	863041	801765089	744839767681	6.91956E+14	6.42827E+17
104	208	979	958441	938313739	918609150481	8.99318E+14	8.80433E+17
105	198	1029	1058841	1089547389	1.12114E+12	1.15366E+15	1.18711E+18
106	201	1079	1164241	1256216039	1.35546E+12	1.46254E+15	1.57808E+18
107	206	1129	1274641	1439069689	1.62471E+12	1.83430E+15	2.07092E+18
108	198	1229	1510441	1856331989	2.28143E+12	2.80388E+15	3.44597E+18
109	199	1329	1766241	2347334289	3.11961E+12	4.14596E+15	5.50998E+18
110	204	1429	2042041	2918076589	4.16993E+12	5.95883E+15	8.51517E+18

MICROHARDNESS DATA - 8 HOURS AT 1550 F. - 38 MIL DECARBURIZED DEPTH

GENERAL LINEAR MODELS PROCEDURE

DEPENDENT VARIABLE: Y

SOURCE	DF	SUM OF SQUARES	MEAN SQUARE	F VALUE	PR > F	R-SQUARE	C.V.
MODEL	5	33131.20355921	6626.24071184	336.21	0.0001	0.941739	2.2843
ERROR	104	2049.66916807	19.70835739		STD DEV		Y MEAN
CORRECTED TOTAL	109	35180.87272727			4.43940958		194.34545455

SOURCE	DF	TYPE I SS	F VALUE	PR > F	DF	TYPE IV SS	F VALUE	PR > F
X	1	13289.91954701	674.33	0.0001	1	5543.82589074	281.29	0.0001
X2	1	11376.63417568	577.25	0.0001	1	2015.55522415	102.27	0.0001
X3	1	6262.13894804	317.74	0.0001	1	1020.75911609	51.79	0.0001
X4	1	1764.25306313	89.52	0.0001	1	629.24597835	31.93	0.0001
X5	1	438.25782536	22.24	0.0001	1	438.25782536	22.24	0.0001

PARAMETER	ESTIMATE	T FOR H0: PARAMETER=0	PR > |T|	STD ERROR OF ESTIMATE
INTERCEPT	131.57510256	64.71	0.0001	2.03340524
X	0.52091125	16.77	0.0001	0.03105876
X2	-0.00141163	-10.11	0.0001	0.00013959
X3	0.00000180	7.20	0.0001	0.00000025
X4	-0.00000000	-5.65	0.0001	0.00000000
X5	0.00000000	4.72	0.0001	0.00000000

MICROHARDNESS DATA - 24 HOURS AT 1550 F. - 80 MIL DECARBURIZED DEPTH

OBS	Y	X	X2	X3	X4
1	136	25	625	15625	390625
2	146	55	3025	166375	9150625
3	151	85	7225	614125	52200625
4	159	115	13225	1520875	174900625
5	159	145	21025	3048625	442050625
6	156	175	30625	5359375	937890625
7	164	205	42025	8615125	1766100625
8	175	235	55225	12977875	3049800625
9	175	265	70225	18609625	4931550625
10	175	295	87025	25672375	7573350625
11	183	345	119025	41063625	14166950625
12	189	395	156025	61629875	24343800625
13	185	445	198025	88121125	39213900625
14	189	495	245025	121287375	60037250625
15	194	545	297025	161878625	88223850625
16	202	595	354025	210644875	125333700625
17	197	645	416025	268336125	173076800625
18	203	695	483025	335702375	233313150625
19	203	745	555025	413493625	308052750625
20	209	795	632025	502459875	399455600625
21	205	895	801025	716917375	641641050625
22	199	995	990025	985074875	980149500625
23	203	1095	1199025	1312932375	1.43766E+12
24	202	1195	1428025	1706489875	2.03926E+12
25	200	1295	1677025	2171747375	2.81241E+12
26	211	1395	1946025	2714704875	3.78701E+12
27	202	1495	2235025	3341362375	4.99534E+12
28	141	34	1156	39304	1336336
29	141	64	4096	262144	16777216
30	149	94	8836	830584	78074896
31	155	124	15376	1906624	236421376
32	159	154	23716	3652264	562448656
33	162	184	33856	6229504	1146228736
34	173	214	45796	9800344	2097273616
35	176	244	59536	14526784	3544535296
36	179	274	75076	20570824	5636405776
37	180	304	92416	28094464	8540717056
38	183	354	125316	44361864	15704099856
39	186	404	163216	65939264	26639462656
40	189	454	206116	93576664	42483805456
41	194	504	254016	128024064	64524128256
42	194	554	306916	170031464	94197431056
43	194	604	364816	220348864	133090713856
44	194	654	427716	279726264	182940976656
45	198	704	495616	348913664	245635219456
46	194	754	568516	428661064	323210442256

MICROHARDNESS DATA - 24 HOURS AT 1550 F. - 80 MIL DECARBURIZED DEPTH

OBS	Y	X	X2	X3	X4
47	194	854	729316	622835864	531901827856
48	194	954	910116	868250664	828311133456
49	196	1054	1110916	1170905464	1.23413E+12
50	201	1154	1331716	1536800264	1.77347E+12
51	200	1254	1572516	1971935064	2.47281E+12
52	196	1354	1833316	2482309864	3.36105E+12
53	198	1454	2114116	3073924664	4.46949E+12
54	134	26	676	17576	456976
55	146	56	3136	175616	9834496
56	151	86	7396	636056	54700816
57	159	116	13456	1560896	181063936
58	164	146	21316	3112136	454371856
59	168	176	30976	5451776	959512576
60	167	206	42436	8741816	1800814096
61	183	236	55696	13144256	3102044416
62	180	266	70756	18821096	5006411536
63	189	296	87616	25934336	7676563456
64	189	326	106276	34645976	11294588176
65	191	376	141376	53157376	19987173376
66	195	426	181476	77308776	32933538576
67	203	476	226576	107850176	51336683776
68	204	526	276676	145531576	76549608976
69	203	576	331776	191102976	110075314176
70	202	626	391876	245314376	153566799376
71	205	676	456976	308915776	208827064576
72	204	726	527076	382657176	277809109776
73	208	776	602176	467288576	362615934976
74	206	826	682276	563559976	465500540176
75	209	926	857476	794022776	735265090576
76	210	1026	1052676	1080045576	1.10813E+12
77	212	1126	1267876	1427628376	1.60751E+12
78	209	1226	1503076	1842771176	2.25924E+12
79	212	1326	1758276	2331473976	3.09153E+12
80	210	1426	2033476	2899736776	4.13502E+12
81	137	32	1024	32768	1048576
82	143	62	3844	238328	14776336
83	145	92	8464	778688	71639296
84	149	122	14884	1815848	221533456
85	160	152	23104	3511808	533794816
86	169	182	33124	6028568	1097199376
87	167	212	44944	9528128	2019963136
88	166	242	58564	14172488	3429742096
89	180	272	73984	20123648	5473632256
90	185	322	103684	33386248	10750371856
91	192	372	138384	51478848	19150131456
92	193	422	178084	75151448	31713911056

MICROHARDNESS DATA - 24 HOURS AT 1550 F. - 80 MIL DECARBURIZED DEPTH

OBS	Y	X	X2	X3	X4
93	184	472	222784	105154048	49632710656
94	191	522	272484	142236648	74247530256
95	194	572	327184	187149248	107049369856
96	190	622	386884	240641848	149679229456
97	192	672	451584	303464448	203928109056
98	201	722	521284	376367048	271737008656
99	200	772	595984	460099648	355196928256
100	207	822	675684	555412248	456548867856
101	200	872	760384	663054848	578183827456
102	205	922	850084	783777448	722642807056
103	203	972	944784	918330048	892616806656
104	212	1072	1149184	1231925248	1.32062E+12
105	210	1172	1373584	1609840448	1.88673E+12
106	211	1272	1617984	2058075648	2.61787E+12
107	209	1372	1882384	2582630848	3.54337E+12
108	211	1472	2166784	3189506048	4.69495E+12

MICROHARDNESS DATA - 24 HOURS AT 1550 F. - 80 MIL DECARBURIZED DEPTH

GENERAL LINEAR MODELS PROCEDURE

DEPENDENT VARIABLE: Y

SOURCE	DF	SUM OF SQUARES	MEAN SQUARE	F VALUE	PR > F	R-SQUARE	C.V.
MODEL	3	46787.87390590	15595.95796863	590.62	0.0001	0.944559	2.7734
ERROR	104	2746.22794595	26.40603794		STD DEV		Y MEAN
CORRECTED TOTAL	107	49534.10185185			5.13868056		185.28703704

SOURCE	DF	TYPE I SS	F VALUE	PR > F	DF	TYPE IV SS	F VALUE	PR > F
X	1	34185.54254021	1294.61	0.0001	1	9668.55114041	366.15	0.0001
X2	1	10862.71319799	411.37	0.0001	1	3422.47391021	129.61	0.0001
X3	1	1739.61816770	65.88	0.0001	1	1739.61816770	65.88	0.0001

PARAMETER	ESTIMATE	T FOR H0: PARAMETER=0	PR > |T|	STD ERROR OF ESTIMATE
INTERCEPT	133.11710742	78.86	0.0001	1.68803005
X	0.20949276	19.14	0.0001	0.01094813
X2	-0.00020621	-11.38	0.0001	0.00001811
X3	0.00000007	8.12	0.0001	0.00000001

APPENDIX B

```
      ***********************************************************************
      * THIS PROGRAM PLOTS FOUR GRAPHS USING DATA COLLECTED DURING THE *
      * STUDY OF THE EFFECTS OF DECARBURIZATION ON THE FATIGUE LIFE    *
      * OF SAE 1042 STEEL.  GRAPHS 1 & 2 CONTAIN S-N DATA AND GRAPHS   *
      * 3 & 4 CONTAIN MICROHARDNESS DATA.  GRAPHS 2 & 4 HAVE 'DEGREE   *
      * OF BEST FIT' CURVES DRAWN AND THE EQUATION OF THE CURVE        *
      * DETERMINED BY A LEAST SQUARES REGRESSION ANALYSIS LISTED.      *
      ***********************************************************************
0001        DIMENSION X5(47),   Y5(47),
     $                X10(47),  Y10(47),
     $                X15(43),  Y15(43),
     $                X20(43),  Y20(43),
     $                X30(110), Y30(110),
     $                X35(102), Y35(102),
     $                X40(112), Y40(112),
     $                X45(110), Y45(110), IAREA(664)
0002        REAL LG5X(47), LG10X(47), LG15X(43), LG20X(43)
0003        INTEGER INT(2)/5,0/
0004        INTEGER INTE(2)/3,0/
0005        INTEGER INTEG(2)/1,0/
0006        CALL PLOTS (IAREA,664,120.0)
0007        CALL ZIPOFF
0008        CALL PLOT (3.0,2.5,-3)

            S-N DATA - AS RECEIVED - SAE 1042 C.F.
0009        READ (5,580) X
0010        READ (5,590) (Y5(I),  X5(I),  I=1,45)

            S-N DATA - NO DECARBURIZATION
0011        READ (5,580) X
0012        READ (5,590) (Y10(I), X10(I), I=1,45)

            S-N DATA - 38 MIL DECARBURIZED DEPTH
0013        READ (5,580) X
0014        READ (5,590) (Y15(I), X15(I), I=1,41)

            S-N DATA - 80 MIL DECARBURIZED DEPTH
0015        READ (5,580) X
0016        READ (5,590) (Y20(I), X20(I), I=1,41)

            MICROHARDNESS DATA - AS RECEIVED - SAE 1042 C.F.
0017        READ (5,580) X
0018        READ (5,560) (Y30(I), X30(I), I=1,103)

            MICROHARDNESS DATA - 1 HOUR AT 1550 F. - NO DECARBURIZATION
0019        READ (5,580) X
0020        READ (5,560) (Y35(I), X35(I), I=1,100)

            MICROHARDNESS DATA - 8 HRS. AT 1550 F. - 38 MIL DECARBURIZED DEPTH
0021        READ (5,580) X
0022        READ (5,560) (Y40(I), X40(I), I=1,110)

            MICROHARDNESS DATA - 24 HRS. AT 1550 F. - 80 MIL DECARBURIZED DEPTH
0023        READ (5,580) X
0024        READ (5,560) (Y45(I), X45(I), I=1,108)
```

```
      ***********************************************************************
      * GRAPH #1 *                         SAE 1042 S-N CURVES              *
      ***********************************************************************
0025  DATA X5(46)/500.0/, X5(47)/0.92/, Y5(46)/15000.0/, Y5(47)/20000.0/
0026  X10(46)=X5(46)
0027  X10(47)=X5(47)
0028  X15(42)=X5(46)
0029  X15(43)=X5(47)
0030  X20(42)=X5(46)
0031  X20(43)=X5(47)
0032  Y10(46)=Y5(46)
0033  Y10(47)=Y5(47)
0034  Y15(42)=Y5(46)
0035  Y15(43)=Y5(47)
0036  Y20(42)=Y5(46)
0037  Y20(43)=Y5(47)

0038  CALL LGAXS (0.0,0.0,41HNUMBER OF REVERSED STRESS CYCLES, N        
     $41,6.48,0.0,X5(46),X5(47))
0039  CALL SYMBOL (5.66,-0.53,0.08,1HF,0.0,1)

0040  CALL AXIS (0.0,0.0,30H  REVERSED BENDING STRESS, PSI,30,4.8,90.0,Y
     $5(46),Y5(47))

0041  CALL PLOT (0.0,4.80,3)
0042  CALL PLOT (6.48,4.8,2)
0043  CALL PLOT (6.48,0.0,2)

0044  CALL PLOT (6.48,0.00,3)
0045  CALL PLOT (6.55,0.00,2)
0046  CALL PLOT (6.48,1.00,3)
0047  CALL PLOT (6.55,1.00,2)
0048  CALL PLOT (6.48,2.00,3)
0049  CALL PLOT (6.55,2.00,2)
0050  CALL PLOT (6.48,3.00,3)
0051  CALL PLOT (6.55,3.00,2)
0052  CALL PLOT (6.48,4.00,3)
0053  CALL PLOT (6.55,4.00,2)
0054  CALL SYMBOL (6.69,-0.10,0.105,6H103.42,90.0,6)
0055  CALL SYMBOL (6.69,0.90,0.105,6H241.30,90.0,6)
0056  CALL SYMBOL (6.69,1.90,0.105,6H379.19,90.0,6)
0057  CALL SYMBOL (6.69,2.90,0.105,6H517.08,90.0,6)
0058  CALL SYMBOL (6.69,3.90,0.105,6H654.97,90.0,6)
0059  CALL SYMBOL (6.88,0.38,0.14,28HREVERSED BENDING STRESS, MN/,90.0,2
     $8)
0060  CALL SYMBOL (6.88,4.28,0.105,1HM,90.0,1)
0061  CALL SYMBOL (6.81,4.38,0.08,1H2,90.0,1)

0062  CALL LGLIN (X5,Y5,45,1,-1,1,-1)
0063  CALL LGLIN (X10,Y10,45,1,-1,5,-1)
0064  CALL LGLIN (X15,Y15,41,1,-1,0,-1)
0065  CALL LGLIN (X20,Y20,41,1,-1,2,-1)
```

```
      CALL SYMBOL (2.20,4.19,0.08,1,0.0,-1)
      CALL SYMBOL (2.45,4.15,0.08,39HAS RECEIVED - 1042 C.F. - 100  -IN.
     $, AA,0.0,39)
      CALL SYMBOL (4.81,4.13,0.13,34,0.0,-1)
      CALL SYMBOL (2.20,3.99,0.08,5,0.0,-1)
      CALL SYMBOL (2.45,3.95,0.08,33HNO DECARBURIZATION - 20  -IN., AA,0
     $.0,33)
      CALL SYMBOL (4.33,3.93,0.13,34,0.0,-1)
      CALL SYMBOL (2.20,3.79,0.08,0,0.0,-1)
      CALL SYMBOL (2.45,3.75,0.08,44H0.038 INCH DECARBURIZED DEPTH - 20
     $ -IN., AA,0.0,44)
      CALL SYMBOL (5.21,3.73,0.13,34,0.0,-1)
      CALL SYMBOL (2.20,3.58,0.08,2,0.0,-1)
      CALL SYMBOL (2.45,3.55,0.08,44H0.080 INCH DECARBURIZED DEPTH - 20
     $ -IN., AA,0.0,44)
      CALL SYMBOL (5.21,3.53,0.13,34,0.0,-1)
      CALL PLOT (13.5,0.0,-3)


      ******************************************************************
      * GRAPH #2 *                  SAE 1042 S-N CURVES                 *
      ******************************************************************
      DO 100 J=1,45
  100 LG5X(J) = ALOG10(X5(J))
      DO 110 J=1,45

  110 LG10X(J) = ALOG10(X10(J))
      DO 120 J=1,41
  120 LG15X(J) = ALOG10(X15(J))
      DO 130 J=1,41
  130 LG20X(J) = ALOG10(X20(J))

      CALL LGAXS (0.0,-0.5,41HNUMBER OF REVERSED STRESS CYCLES, N       ,
     $-41,08.3,0.0,251.2,0.8)
      CALL SYMBOL (6.58,-1.02,0.08,1HF,0.0,1)

      CALL PLOT (0.0,5.0,3)
      CALL PLOT (0.0,6.0,2)
      CALL PLOT (8.3,6.0,2)
      CALL PLOT (8.3,0.0,2)

      CALL CRVPT (LG15X,Y15,-3,41,-1,6.0,08.3,' ',1,'LOG10',5,'
     $REVERSED BENDING STRESS, PSI',37,INTE)

      CALL CRVPT (LG5X,Y5,-1,-45,-1,6.0,08.3,' ',1,' ',1,' ',1,INTE)

      CALL CRVPT (LG10X,Y10,-5,-45,-1,6.0,08.3,' ',1,' ',1,' ',1,INTE)

      CALL CRVPT (LG20X,Y20,-2,-41,1,6.0,08.3,' ',1,' ',1,' ',1,INTE)
      CALL PLOT (3.0,0.0,-3)
```

```
        ************************************************************************
        * GRAPH #3 *            SAE 1042 DECARBURIZATION DEPTHS                *
        ************************************************************************
0098     DATA X30(109)/0.0/, X30(110)/0.025/, Y30(109)/120.0/, Y30(110)/30.
        $0/
0099     X35(101)=X30(109)
0100     X35(102)=X30(110)
0101     X40(111)=X30(109)
0102     X40(112)=X30(110)
0103     X45(109)=X30(109)
0104     X45(110)=X30(110)
0105     Y35(101)=Y30(109)
0106     Y35(102)=Y30(110)
0107     Y40(111)=Y30(109)
0108     Y40(112)=Y30(110)
0109     Y45(109)=Y30(109)
0110     Y45(110)=Y30(110)

0111     CALL AXIS (0.0,0.0,26HDEPTH FROM SURFACE, INCHES,-26,6.48,0.0,X30(
        $109),X30(110))

0112     CALL AXIS (0.0,0.0,32H MICROHARDNESS, DPH, (200 GRAMS),32,4.67,90.
        $0,Y30(109),Y30(110))

0113     CALL PLOT (0.0,4.60,3)
0114     CALL PLOT (6.48,4.6,2)
0115     CALL PLOT (6.48,0.0,2)

0116     CALL PLOT (6.48,0.33,3)
0117     CALL PLOT (6.55,0.33,2)
0118     CALL PLOT (6.48,2.82,3)
0119     CALL PLOT (6.55,2.82,2)
0120     CALL PLOT (6.48,3.72,3)
0121     CALL PLOT (6.55,3.72,2)
0122     CALL SYMBOL (6.69,0.23,0.105,5H71.00,90.0,5)
0123     CALL SYMBOL (6.69,2.72,0.105,5H92.33,90.0,5)
0124     CALL SYMBOL (6.69,3.62,0.105,5H97.00,90.0,5)
0125     CALL SYMBOL (6.88,1.52,0.14,11HHARDNESS, R,90.0,11)
0126     CALL SYMBOL (6.93,3.04,0.08,1HB,90.0,1)

0127     CALL PLOT (0.79,4.60,3)
0128     CALL PLOT (0.79,4.67,2)
0129     CALL PLOT (1.57,4.60,3)
0130     CALL PLOT (1.57,4.67,2)
0131     CALL PLOT (2.36,4.60,3)
0132     CALL PLOT (2.36,4.67,2)
0133     CALL PLOT (3.15,4.60,3)
0134     CALL PLOT (3.15,4.67,2)
0135     CALL PLOT (3.94,4.60,3)
0136     CALL PLOT (3.94,4.67,2)
0137     CALL PLOT (4.72,4.60,3)
0138     CALL PLOT (4.72,4.67,2)
0139     CALL PLOT (5.51,4.60,3)
0140     CALL PLOT (5.51,4.67,2)
0141     CALL PLOT (6.30,4.60,3)
0142     CALL PLOT (6.30,4.67,2)
```

```
0143          CALL SYMBOL (-0.09,4.70,0.105,4H0.00,0.0,4)
0144          CALL SYMBOL (0.69,4.70,0.105,4H0.50,0.0,4)
0145          CALL SYMBOL (1.47,4.70,0.105,4H1.00,0.0,4)
0146          CALL SYMBOL (2.26,4.70,0.105,4H1.50,0.0,4)
0147          CALL SYMBOL (3.05,4.70,0.105,4H2.00,0.0,4)
0148          CALL SYMBOL (3.84,4.70,0.105,4H2.50,0.0,4)
0149          CALL SYMBOL (4.62,4.70,0.105,4H3.00,0.0,4)
0150          CALL SYMBOL (5.41,4.70,0.105,4H3.50,0.0,4)
0151          CALL SYMBOL (6.20,4.70,0.105,4H4.00,0.0,4)
0152          CALL SYMBOL (1.73,4.85,0.14,22HDEPTH FROM SURFACE, IN,0.0,22)

0153          CALL LINE (X30,Y30,108,1,-1,1)
0154          CALL LINE (X35,Y35,100,1,-1,5)
0155          CALL LINE (X40,Y40,110,1,-1,0)
0156          CALL LINE (X45,Y45,108,1,-1,2)

0157          CALL SYMBOL (1.90,1.10,0.08,1,0.0,-1)
0158          CALL SYMBOL (2.15,1.06,0.08,32HAS RECEIVED - 1042 C.F. - ASTM 8,0.
             $0,32)
0159          CALL SYMBOL (1.90,0.90,0.08,5,0.0,-1)
0160          CALL SYMBOL (2.15,0.86,0.08,48HNO DECARBURIZATION - 1 HOUR AT 1550
             $ F. - ASTM 10,0.0,48)
0161          CALL SYMBOL (1.90,0.70,0.08,0,0.0,-1)
0162          CALL SYMBOL (2.15,0.66,0.08,41HDECARBURIZED 8 HOURS AT 1550 F. - A
             $STM 10,0.0,41)
0163          CALL SYMBOL (1.90,0.49,0.08,2,0.0,-1)
0164          CALL SYMBOL (2.15,0.46,0.08,42HDECARBURIZED 24 HOURS AT 1550 F. -
             $ASTM 10,0.0,42)
0165          CALL PLOT (13.5,-1.0,-3)


              *******************************************************************
              * GRAPH #4 *           SAE 1042 DECARBURIZATION DEPTHS            *
              *******************************************************************
0166          CALL PLOT (0.0,6.0,3)
0167          CALL PLOT (0.0,7.0,2)
0168          CALL PLOT (8.3,7.0,2)
0169          CALL PLOT (8.3,0.0,2)

0170          CALL CRVPT (X40,Y40,-3,110,-1,7.0,08.3,' ',1,'DEPTH FROM SURFACE,
             $INCHES',26,'        MICROHARDNESS, DPH, (200 GRAMS)',38,INT)

0171          CALL CRVPT (X30,Y30,-1,-108,-1,7.0,08.3,' ',1,' ',1,' ',1,INTE3)

0172          CALL CRVPT (X35,Y35,-5,-100,-1,7.0,08.3,' ',1,' ',1,' ',1,INTE3)

0173          CALL CRVPT (X45,Y45,-2,-108,1,7.0,08.3,' ',1,' ',1,' ',1,INTE)
0174          CALL PLOT (0.0,0.0,999)
```

```
      WRITE (6,500)
      WRITE (6,600)  (Y5(I), X5(I), LG5X(I), Y10(I), X10(I), LG10X(I), I=
     $1,45)
      WRITE (6,510)
      WRITE (6,600)  (Y15(I), X15(I), LG15X(I), Y20(I), X20(I), LG20X(I),
     $I=1,41)
      WRITE (6,520)
      WRITE (6,570)  (Y30(I), X30(I), Y30(I+54), X30(I+54), I=1,54)
      WRITE (6,530)
      WRITE (6,570)  (Y35(I), X35(I), Y35(I+50), X35(I+50), I=1,50)
      WRITE (6,540)
      WRITE (6,570)  (Y40(I), X40(I), Y40(I+55), X40(I+55), I=1,55)
      WRITE (6,550)
      WRITE (6,570)  (Y45(I), X45(I), Y45(I+54), X45(I+54), I=1,54)

  500 FORMAT (1H1//////T11,'S-N DATA - AS RECEIVED - SAE 1042 C.F.',T90,
     $'S-N DATA - NO DECARBURIZATION'//T6,'STRESS, PSI',T24,'NO. OF CYCL
     $ES',T41,'LOG10(CYCLES)',T81,'STRESS, PSI',T99,'NO. OF CYCLES',T116
     $,'LOG10(CYCLES)'/)

  510 FORMAT (1H1//////T10,'S-N DATA - 0.038 INCH DECARBURIZED DEPTH',T8
     $5,'S-N DATA - 0.080 INCH DECARBURIZED DEPTH'//T5,'STRESS, PSI',T24
     $,'NO. OF CYCLES',T41,'LOG10(CYCLES)',T81,'STRESS, PSI',T99,'NO. OF
     $CYCLES',T116,'LOG10(CYCLES)'/)

  520 FORMAT (1H1,T11,'MICROHARDNESS DATA - AS RECEIVED - SAE 1042 C.F.'
     $,T94,'(CONTINUED)'//T14,'HARDNESS, DPH',T35,'DEPTH FROM SURFACE, I
     $NCHES',T79,'HARDNESS, DPH',T100,'DEPTH FROM SURFACE, INCHES'/)

  530 FORMAT (1H1,T16,'MICROHARDNESS DATA - 1 HOUR AT 1550 F.',T94,'(CON
     $TINUED)'//T14,'HARDNESS, DPH',T35,'DEPTH FROM SURFACE, INCHES',T79
     $,'HARDNESS, DPH',T100,'DEPTH FROM SURFACE, INCHES'/)

  540 FORMAT (1H1,T16,'MICROHARDNESS DATA - 3 HOURS AT 1550 F.',T94,'(CO
     $NTINUED)'//T14,'HARDNESS, DPH',T35,'DEPTH FROM SURFACE, INCHES',T7
     $9,'HARDNESS, DPH',T100,'DEPTH FROM SURFACE, INCHES'/)

  550 FORMAT (1H1,T15,'MICROHARDNESS DATA - 24 HOURS AT 1550 F.',T94,'(C
     $ONTINUED)'//T14,'HARDNESS, DPH',T35,'DEPTH FROM SURFACE, INCHES',T
     $79,'HARDNESS, DPH',T100,'DEPTH FROM SURFACE, INCHES'/)

  560 FORMAT (F3.0,17X,F10.4)
  570 FORMAT (1H ,T13,F10.0,T41,F10.4,T78,F10.0,T106,F10.4)
  580 FORMAT (2F10.0)
  590 FORMAT (F10.0,F20.0)
  600 FORMAT (1H ,T5,F10.0,T18,F15.0,T41,F10.4,T80,F10.0,T93,F15.0,T116,
     $F10.4)
      STOP
      END
```

APPENDIX C

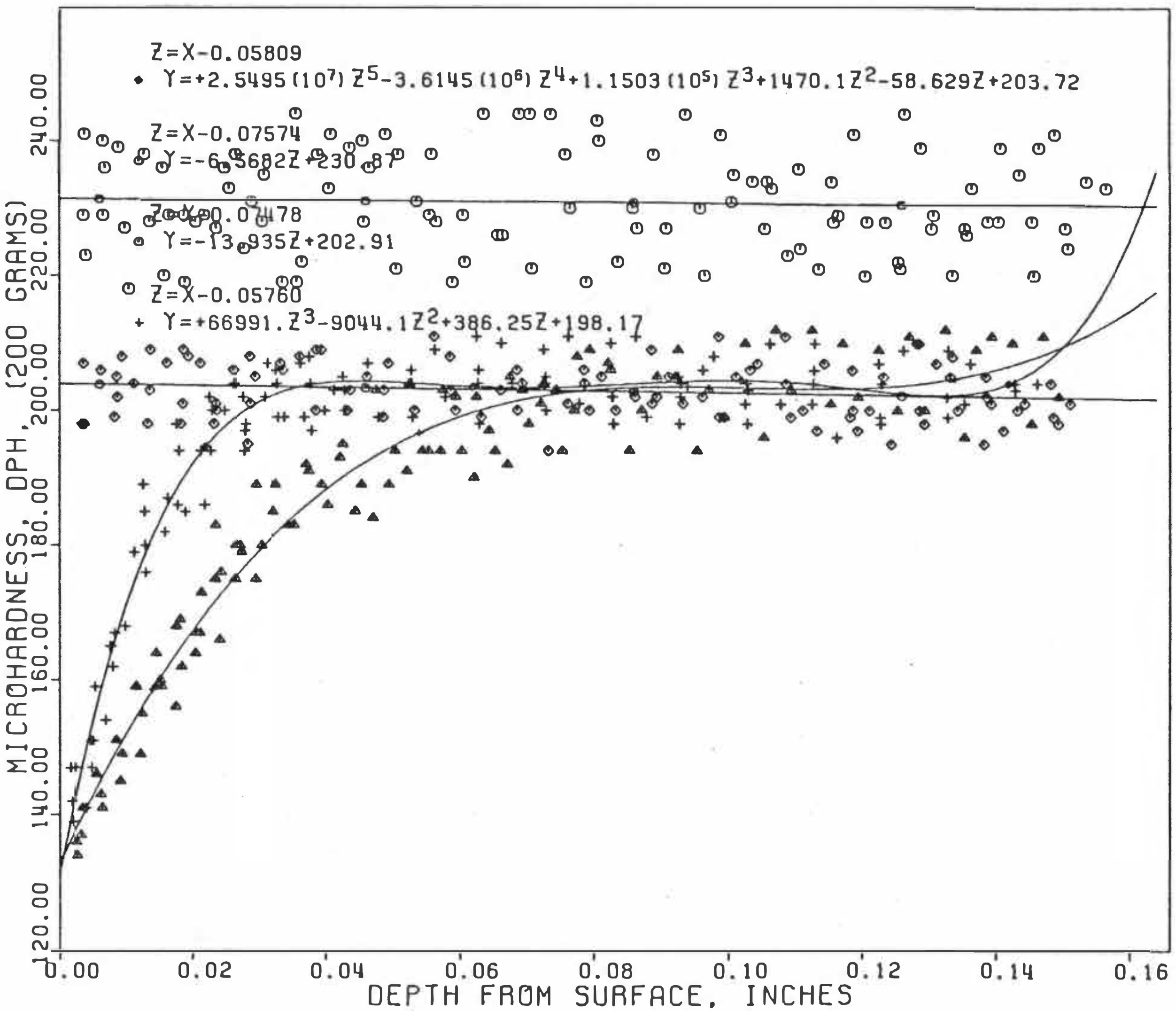

Figure 49. Hardness Curves as Drawn by the Calcomp Plotting Program.

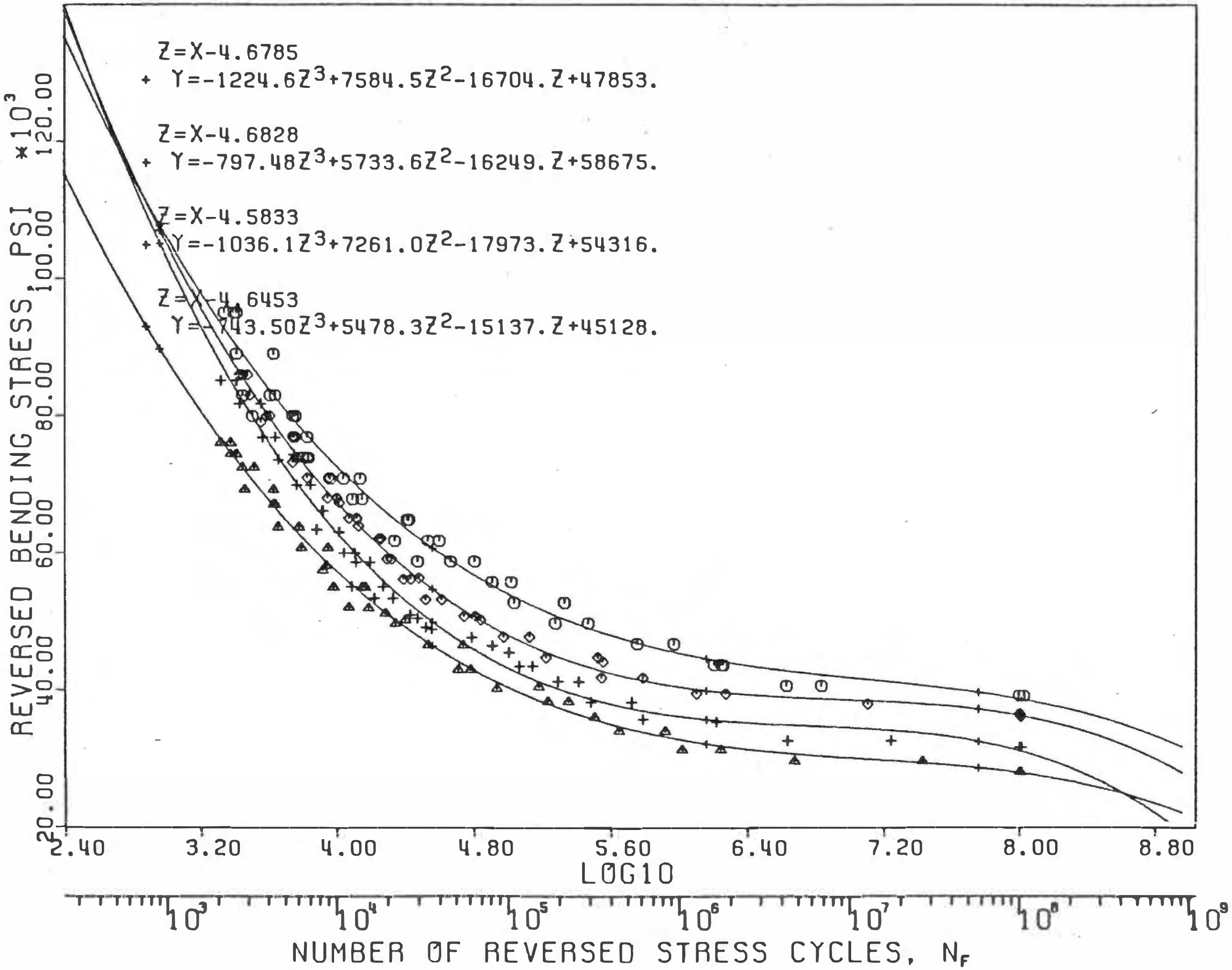

Figure 50. S-N Curves as Drawn by the Calcomp Plotting Program.

APPENDIX D

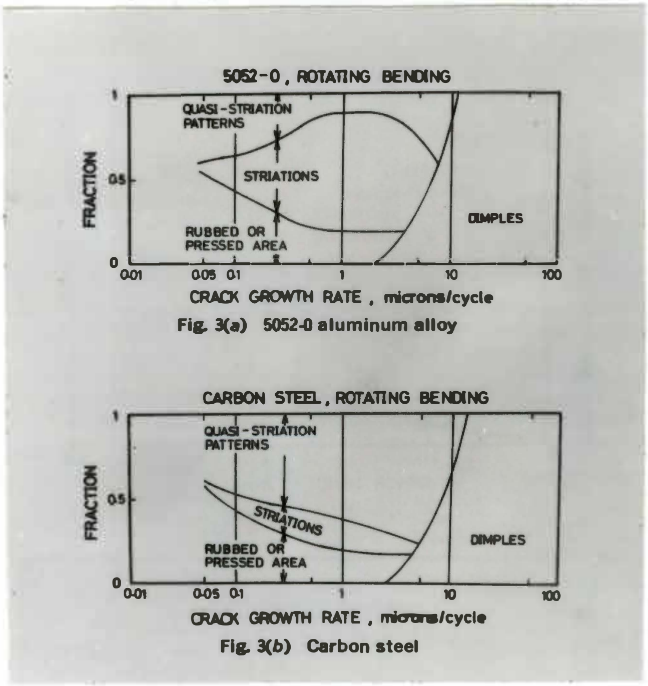

Figure 51. Schematic Representation of the Fraction of Fracture Surfaces Covered by Striations and Quasi-Striation Patterns.

Source: Koterazawa, R., Mori, M., Matsui, T., and Shimo, D., Fractographic Study of Fatigue Crack Propagation," Trans. ASME, and J. Engineering Materials and Technology, vol. 95, No. 4, Series H, October, 1973, pp. 202-211.

VITA

Daniel Alexander Bales was born in Jefferson City, Tennessee on March 11, 1951. He attended elementary schools and high school in that city. In September 1969 he entered The University of Tennessee, Knoxville; and was accepted to the Co-operative Engineering Program in January 1970. His Bachelor of Science degree in Mechanical Engineering was awarded in June 1974. From June 1974 until September 1974, he was employed as a design engineer with Cincinnati Milacron in Cincinnati, Ohio, his Co-operative Engineering Employer.

In September 1974 Mr. Bales accepted a teaching assistantship in the Department of Chemical and Metallurgical Engineering at The University of Tennessee, Knoxville. He received the Master of Science degree with a major in Metallurgical Engineering in August 1977.

He is a member of the American Society of Mechanical Engineers, the American Society for Metals, and Alpha Chi Sigma Honorary Fraternity.